**POLITECNICO DI MILANO**

School of Industrial and Information Engineering

Department of Energy

Master's Degree in Energy Engineering

# CFD simulation of sprays for IC engine applications: effects of sub-models and mesh structure

*Thesis Supervisor:*
Prof. Tommaso LUCCHINI

*Co-supervisor:*
Ing. Davide PAREDI

Master's thesis author:
Alberto Isacchi, Matr. 872121

Academic Year: 2018 – 2019

Vuoi davvero lasciare ai tuoi occhi
solo i sogni che non fanno svegliare
*F. De André*

# AKNOWLEDGMENTS

*In primo luogo, vorrei ringraziare i miei genitori che mi hanno sempre sostenuto e seguito in questo percorso non facendomi mai mancare nulla. Mi avete permesso di giungere fino a questo punto eliminando tutte le preoccupazioni che avrebbero potuto rallentarmi o fermarmi. So che avete vissuto questi anni tanto intensamente quanto ho fatto io.*

*Vorrei ringraziare il professor Tommaso Lucchini e l'ing. Davide Paredi per avermi seguito e aiutato durante la tesi, proponendomi un lavoro stimolante e mai banale. Ringrazio inoltre il professor Augusto Della Torre che mi ha aiutato mettendo a mia disposizione la sua esperienza.*

*Un grazie va anche a tutto il resto della mia famiglia che mi ha sempre sostenuto.*

*Infine, un grazie è dovuto a tutti gli amici che sono stati con me in questi cinque anni. Mi avete fatto divertire e mi avete ricordato che nella vita non c'è solo lo studio o il lavoro.*
*Ringrazio gli amici di Barzago e dintorni, assieme ai quali ho passato molto tempo e molte serate (siete troppi per menzionarvi tutti).*
*Ringrazio i vecchi amici delle superiori (Tommaso, Gioele, Dario, Andrea) sempre disponibili a fare due chiacchere e svagarsi.*
*Ringrazio anche tutti i ragazzi conosciuti qui al Politecnico che sono stati miei compagni di percorso, ma anche amici (non vi nomino tutti altrimenti ne dimenticherei sicuramente qualcuno, facendovi un torto imperdonabile). Grazie a voi non è stato così pesante alla fine.*
*Grazie ai ragazzi del 2V Villa Vergano, miei compagni di squadra con cui ho condiviso gioie e dolori.*
*Non mi sono scordato nemmeno dei vecchi compagni di treno ai tempi del Besanino, è sempre bello incontrarsi a ricordare i vecchi tempi*
*Infine, vorrei menzionare in modo particolare Daniele e Danilo, siete stati amici, compagni di percorso e molto altro ancora.*

*Alberto*

# INDEX

# ABSTRACT

During this thesis work, the effects of sub-models and mesh structure are evaluated for Computational Fluid Dynamics (CFD) simulation of sprays for Internal Combustion (IC) engine applications.
Nowadays, the objectives of the research activity in the internal combustion engine field include the increase of efficiency and the reduction of emissions. They can be reached through an improvement of the combustion process. To do this, the knowledge of the air-fuel mixing process and the study of sprays are fundamental.
CFD is a useful research tool for the study of internal combustion engines. It allows to test different configurations and to achieve accurate results saving time and costs.
In CFD simulations of sprays, the liquid dispersed phase is described through a Lagrangian approach coupled with a Eulerian approach for the gas phase. Several sub-models are necessary to describe the spray and its behaviour as well as the turbulent motion that it generates.
In the first part of this work, the spray G configuration has been adopted to evaluate the effects of different sub-models on the simulations, with focus on the breakup models. The objective is to find a numerical setup able to predict the experimental results provided by the Engine Combustion Network for spray G configuration. While the models are calibrated, the effects produced by changing their parameters are investigated.
In the last part of the work, a numerical analysis on spray simulations has been performed. According to the literature, the numerical results obtained from these simulations strongly depend on the grid adopted. Considering the main mesh structures commonly used for sprays in IC engine applications (spray-oriented grids and cartesian grids), the numerical results are compared analysing the effects related to the grid quality, accounting also for the issues related to the interaction between Lagrangian parcels and grid elements. The final task is to verify the performances provided by different grid structures and to evaluate how the numerical effects influence the results.

**KEYWORDS:** spray G, CFD, OpenFOAM, internal combustion engines, breakup models, mesh structure.

# SOMMARIO

In questo lavoro di tesi, sono stati valutati gli effetti dei sotto-modelli e della struttura della mesh sulle simulazioni di Fluido Dinamica Computazionale (CFD) di spray per applicazioni nel campo dei motori a combustione interna.
Al giorno d'oggi, gli obiettivi dell'attività di ricerca nel campo motoristico comprendono l'aumento dell'efficienza e la riduzione delle emissioni. Essi possono essere raggiunti attraverso il miglioramento del processo di combustione. Per fare ciò, la conoscenza del processo di formazione della miscela aria-carburante e lo studio degli spray sono fondamentali.
La CFD è uno strumento di ricerca molto utile per lo studio dei motori a combustione interna. Essa permette di testare differenti configurazioni e di ottenere risultati affidabili risparmiando tempo e riducendo costi.
Nelle simulazioni CFD degli spray, la fase liquida dispersa è descritta tramite un approccio Lagrangiano accoppiato con un approccio Euleriano per la fase gassosa. Diversi sotto-modelli sono necessari per descrivere lo spray e il suo comportamento, oltre che al campo di moto turbolento che esso genera.
Nella prima parte di questo lavoro, gli effetti dei diversi sotto-modelli sono valutati utilizzando la configurazione dello spray G, focalizzandosi in modo particolare sui modelli di breakup. L'obiettivo è quello di trovare un setup numerico capace di predire i dati sperimentali forniti dall' Engine Combustion Network (ECN) per questa configurazione. Mentre i modelli vengono calibrati, sono investigati gli effetti prodotti cambiando i loro parametri.
Nell'ultima parte del lavoro, è stata realizzata un'analisi numerica riguardante le simulazioni degli spray. In accordo con quanto affermato dalla teoria, i risultati di questo tipo di simulazioni dipendono fortemente dalla griglia adottata. Prendendo in considerazione le principali strutture di mesh comunemente utilizzate per gli spray in applicazioni motoristiche (griglie spray-oriented e griglie cartesiane), i risultai numerici sono confrontati analizzando gli effetti relativi alla qualità della mesh tenendo conto anche dell'interazione tra le particelle Lagrangiane e gli elementi della mesh stessa. Gli obiettivi sono quelli di verificare le performances fornite dalle diverse strutture e di valutare come gli effetti numerici influenzino i risultati.

**PAROLE CHIAVE:** spray G, CFD, OpenFOAM, motori a combustione interna, modelli di breakup, struttura della mesh.

# EXTENDED ABSTRACT

## Introduction

Nowadays, environmental awareness has become of primary importance in the automotive industry, as consequence of government regulations and market dynamics. Indeed, an important part of the research activity is focused on the reduction of emissions and on the increase of engine efficiency. To achieve these objectives, a proper design of the combustion process is fundamental. The air-fuel mixing strongly influences combustion and, hence, it is a matter of intense research. In diesel engines and Gasoline Direct Injection (GDI) engines, the fuel is injected directly into the cylinder at high pressures. What results is a spray whose characterises are the key to understand the air-fuel mixing.
Computational Fluid Dynamics is a useful research tool in the field of internal combustion engines. It allows to test different configurations and to achieve accurate results in much less time than what would be required by the corresponding experimental applications. For the case of spray simulations, CFD, combined with experimental measurements, allows to understand the physical phenomena that governs atomization, breakup, evaporation and mixture formation
The numerical modelling of sprays is very complex since it implies the description of a two-phase system with highly turbulent fields and very strong gradients. The liquid dispersed phase is described through a Lagrangian approach coupled with a Eulerian approach for the gas phase. Moreover, several sub-models are required to describe turbulence and spray behaviour. The results of CFD simulations of sprays for IC engines applications strongly depend on the sub-models adopted and on the structure of the mesh used to discretize the domain.
The Engine Combustion Network (ECN) [1] is an international collaboration among researchers that collects the contribution of different institutes with the purpose to join the efforts in IC engines analysis. GDI and diesel sprays represent a central topic in the research activity proposed by ECN. The spray G configuration has been proposed as a standard condition to study the spray in GDI engines. It corresponds to a non-reacting early injection case for spray-guided gasoline injection referred to a modern advanced injection system with high pressure capability.

## Thesis Purpose and Structure

During previous ECN workshops, several studies on CFD simulations of sprays have been performed to find a numerical setup able to provide accurate predictions of experimental data. These simulations have been proved to be strongly dependent on the setup used.
Therefore, the main scope of the thesis activity is the analysis of the effects produced by sub-models and mesh structure on spray simulations for IC engine applications. The

results obtained will allow to improve the numerical setup adopted and to investigate the issues related to numerical modelling of sprays.
The first part of the thesis work is devoted to a literature review. First, the GDI technology is introduced to give a context to spray G simulations. The Lagrangian-Eulerian approach adopted in spray simulations is presented together with a description of turbulence and breakup sub-models. After that, the finite volume method is introduced with the aim to provide the tools necessary to evaluate the quality of the numerical results.
In the second part, corresponding to chapters 5 and 6, CFD simulations adopting the spray G configuration are performed to validate a numerical setup by comparing its results with experimental data. This analysis adopts as starting point the numerical setup proposed by Politecnico di Milano during the previous ECN workshop. Particular attention is paid to assess the performances of secondary breakup models. Moreover, different mesh structures and turbulence models are tested observing the effects on the numerical results produced.
In the last part, corresponding to chapter 7, a numerical analysis is performed to investigate the main numerical effects related to the mesh structure. A spray configuration typical of diesel engines is adopted to simplify the numerical description of the problem. The conditions described by this configuration provide a faster evaporation of the fuel. As consequence of previous experiences, the numerical setup and the sub-models are well established for this kind of simulations.

**Spray Modelling and Main Assumptions**

In this thesis work, the analysis on sprays for IC engine applications are performed by studying the injection of liquid fuel into a constant-volume vessel filled by inert gas ($N_2$). The boundary conditions are set to reproduce the typical working conditions of IC engines.
Two different configurations are analysed in this work:

- The spray G configuration is adopted in the validation of the numerical setup. It corresponds to an early injection case for spray-guided gasoline injection. The fuel adopted is iso-octane and, initially, temperature and pressure are constant inside the vessel with a value of 573 K and 6.0 bar respectively. The inert gas is quiescent before the start of injection. In Fig. 1 is reported the injector geometry which refers to the Delphi solenoid-activated injector. The fuel is injected by eight identical holes disposed around a central axis of symmetry; the injection angle is 34° with respect to the z-axis.
- The configuration typical of diesel engine sprays is adopted for the numerical analysis. It is slightly different with respect to the conditions specified by ECN for spray G. The fuel is n-dodecane and it is injected always through an eight-holes injector. The injection angle is 77.5° with respect to the z-axis. Temperature and pressure are changed respectively to 1000 K and 160 bar. In these conditions the fuel evaporation is faster with respect to spray G.

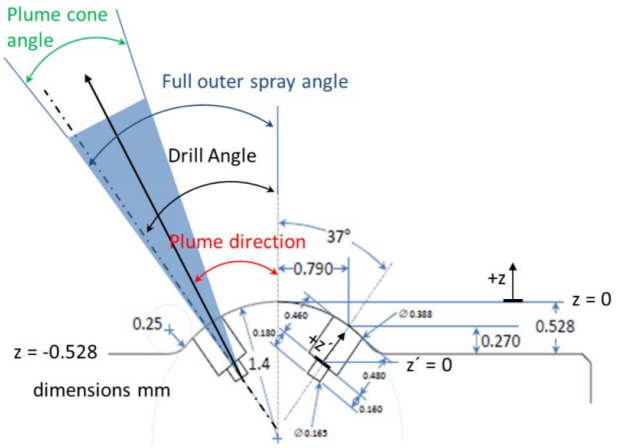


***Fig. 1 Injector geometry for spray G simulations***

The spray injection into an inert gas produces a two-phase non-reacting system governed by the conservation equations expressed in the Navier-Stokes formulation. The Lagrangian-Eulerian approach is adopted to describe the two phases saving memory and time requirements.

The gas phase is described through a Eulerian approach and it is treated as an ideal multicomponent mixture (composed by inert gas and fuel vapours) adopting the ideal gas law. The Newtonian fluid assumption and the isotropic fluid assumptions are also applied. The gas phase behaviour is completely described by the conservation equations (mass, momentum, energy and species) and the equation of state. The presence of the liquid phase is accounted in the conservation equations through suitable source terms.

The liquid phase is described through a Lagrangian approach adopting the discrete droplet model (DDM) [2]. This model features a Monte-Carlo based solution technique for the spray equation, that describes the spray droplets by stochastic particles which are called parcels. These parcels are considered representative of all the spray droplets. The liquid is assumed to be a Newtonian and isotropic fluid with temperature dependant properties. To describe its behaviour the droplet mass equation, the equation of motion and the droplet energy equation are solved. The liquid parcels account for the presence of the gas phase by imposing as boundary conditions the actual data of the owner cell, which is the cell that contains the parcel itself.

The URANS (Unsteady Reynolds Averaged Navier-Stokes) approach is used to describe turbulence with the $k$ - $\varepsilon$ models family.

The description of the spray breakup is done by means of breakup sub-models. The primary breakup (or atomization) models describe the breakup of the intact liquid phase into first ligaments and droplets, while the secondary breakup models describe the breakup of the already existing liquid droplets into smaller ones. To complete the numerical description of the spray other sub-models are required (such as evaporation and drag models), but they are not the focus for this thesis work. The collision among liquid droplets is neglected, since collision models provide convergence issues.

**Numerical Setup Validation for Spray G: Main Results**

The validation of the numerical setup is performed by comparing the results with experimental data provided by ECN. The numerical setup proposed by Politecnico di Milano during the previous ECN workshop is used as starting point [3]. This setup is currently the one that ensures the best results on spray G simulations if compared to experimental data. It adopts a cartesian grid with a cell size of 2 mm refined with the *adaptive local mesh refinement* (AMR). The geometric field used as refinement criterion is the total fuel mass fraction and the refinement level adopted is equal to 2 (creating refined cells with a side length of 0.5 mm). The spray is modelled with the Huh-Gosman model for primary breakup and the KHRT model for secondary breakup. The turbulence model used is the standard $k$ - $\varepsilon$ model with $C_{1\varepsilon}$ = 1.5 as suggested for jets and sprays.
The methodology adopted in this analysis consists in the comparison among the results from different simulations. The numerical setup adopted is the same in all the simulations except for a single input parameter that is changed to evaluate the effects that it produces on the results.
First, different secondary breakup models are compared according to this methodology in order to assess their performances. The main results obtained are summarized trying to understand the strengths and weaknesses of each model.
TAB and ETAB (presented in [4] and [5] respectively) models provide similar results with a very poor droplet breakup. The simulated spray is composed by large liquid drops (the droplets $SMD$ are strongly overestimated) which hardly evaporate. The penetration values are largely overestimated and the spray morphology is completely different from experimental observations. Given these results, TAB and ETAB are not suitable breakup models for sprays simulations.
The Pilch-Erdman (PE) [6] breakup model provides good penetration values after a suitable calibration of the constants. It contains only two adjustable parameters, but the most significant effects are shown while changing $B_2$. As its value is deceased, the spray penetration decreases too. The model accounts for the breakup only by reducing the diameter of the parent droplets without creating child drops. This results in a spray morphology where the tips of the spray plumes are composed by large droplets. They hardly evaporate and the penetration values obtained are mainly the consequence of their motion into the inert gas. To summarize, this model is very simple to calibrate and it provides good penetration values since it has been obtained from experimental-based correlations. The spray morphology that it provides is very different from experimental observations, so, it not suitable to obtain a complete and detailed characterization of the spray.
Similar conclusions can be drawn for the KHRTPE model. This hybrid model has been developed by the ICE group in Politecnico with the aim to combine PE and KHRT models. In this case, the model calibration is more complex, since there are more adjustable parameters to consider. Moreover, the penetration values are not so accurate such as the one provided by the Pilch-Erdman model. The morphology shows once again a spray where the plume tips are composed by big droplets, similarly to what is observed for the PE model. Also this model is not suitable to obtain accurate results in spray simulations.

The KHRT model [7] for secondary breakup coupled with the Huh-Gosman model [8] for primary breakup provides the most accurate description of the spray breakup mechanism. The numerical results well predict the experimental data, except for $SMD$ values that are slightly underestimated and liquid velocity values that are overestimated. The non-accurate prediction of these values has been proved to be a consequence of the numerical effects investigated in the second part of the analysis performed in this thesis. In fact, the area contraction coefficient $C_d$ adopted is equal to 0.72. This value is obtained from some experimental measurements and it is adjusted to fit experimental data.

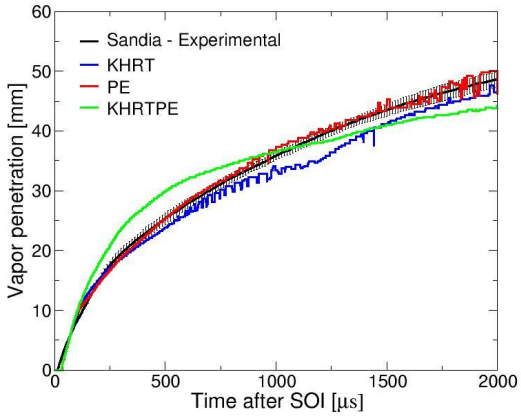


***Fig. 2 - Vapor penetration obtained with KHRT, PE and KHRTPE models***

Fig. 2 compares the vapor penetration values obtained with different secondary breakup models (KHRT, PE and KHRTPE). The setups, chosen to represent the model performances, are the ones that provides the most accurate prediction of the experimental data adopting the model considered.
Instead, in Fig. 3 the morphologies of the sprays obtained with different secondary breakup models are compared with experimental observations (Exp.UoM). In this picture the issues highlighted before are clearly shown.

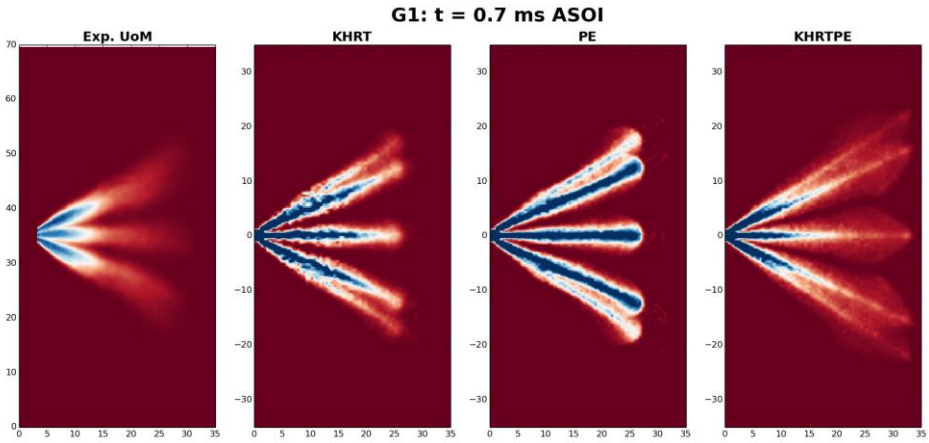


***Fig. 3 - Spray morphology obtained with different secondary breakup models***

The validation process has been carried on adopting the KHRT model for secondary breakup coupled with the Huh-Gosman model for atomization.
The effects of different turbulence model are studied testing the standard $k$-$\varepsilon$ model with $C_{1\varepsilon}$ = 1.5 and with $C_{1\varepsilon}$ = 1.44 and the RNG $k$-$\varepsilon$ model. The results are proved to be very sensitive to the choice of the model. In particular, in Fig. 4 very different results are provided while evaluating the axial velocity of the gas phase in the region in between the spray plumes. The gas motion in this location strongly affects the air entrainment and consequently the air-fuel mixing. From this point of view, the most accurate predictions of the experimental value are provided by the standard $k$-$\varepsilon$ model with $C_{1\varepsilon}$ = 1.5.

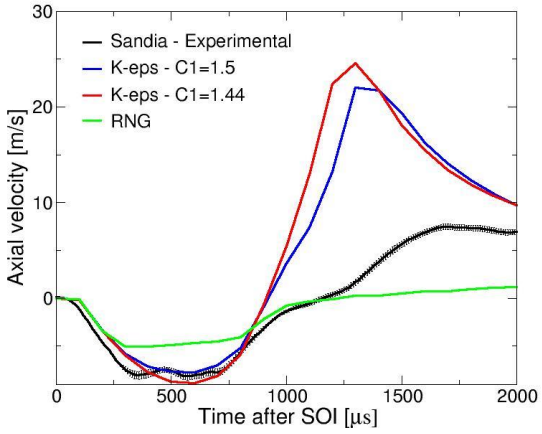


***Fig. 4 - Axial velocity of the gas phase as function of time sampled on the z-axis 15 mm above the injector location. Three different setups are adopted to describe turbulence***

In the final part of the validation process, different mesh structures are compared to evaluate the sensitivity of the results to the mesh structure. The mesh considered are three: a cartesian mesh with AMR, a fixed cartesian mesh with a side length of the cells equal to 0.5 mm and a spray-oriented grid which simulates only a single injector hole with proper symmetry boundary conditions. Again, the most significant difference in the results are shown in the axial velocity plot illustrated in Fig. 5.

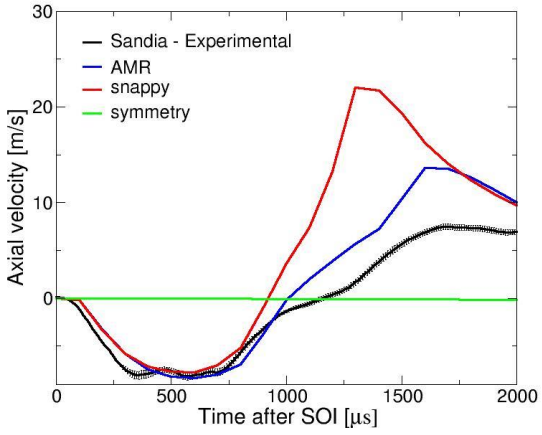


***Fig. 5 - Axial velocity of the gas phase as function of time evaluated on different grid structures***

The numerical analysis performed in the last part of this thesis work aims to deeper investigate these results and the grid dependency of the numerical results in spray simulations.

**Mesh Structure Effects: Main Results**

When a Lagrangian-Eulerian combined approach is adopted, many aspects regarding the grid must be considered to obtain reliable results. In addition to the mesh quality (expressed in terms of non-orthogonality, skewness and aspect ratio), also the presence of the Lagrangian parcels and their interaction with the grid must be accounted when the domain is discretized.
A spray configuration typical of diesel engines is adopted to simplify the numerical description of the problem. The conditions described by this configuration provide a faster evaporation of the fuel. The numerical setup and the sub-models are well established for this kind of simulations, since they have been studied for longer with respect to spray G conditions.
This part of the analysis adopts a numerical case as reference. This case is composed by a single plume of spray that is simulated by a grid which is simultaneously spray-oriented and cartesian. A study is performed to decide a cell size such to avoid void fraction issues. According to the literature, a void fraction lower than the threshold value of $10^{-2}$ does not compromise the results.
This reference case is compared to the main grid arrangements adopted in spray simulations: cartesian and spray-oriented grids. The results obtained are here summarized.
The adoption of a cartesian mesh allows to obtain the highest quality possible in terms of non-orthogonality, skewness and aspect ratio. The main issue highlighted for this grid arrangement is related to the interaction between liquid droplets and mesh elements. In almost all the practical cases, the grid lines do not follow the spray orientation. When this happens, the Lagrangian parcels result to be slowed down more than what happens for a spray-oriented grid. The most important consequences are noticed for penetration values that are underestimated. To overcome this issue, the tuning of the area contraction coefficient $C_d$ is a solution to adjust the numerical results. As this value is reduced, the penetration values increase. As side effect, the liquid velocity close to the injection position is strongly overpredicted, with consequences on spray breakup. This implies a further tuning of the parameters present inside all the sub-models adopted for the spray. Moreover, when the grid lines are not aligned with the spray direction, the liquid velocity close to the tip of the plume is not accurately predicted with possible consequences on the wall impingement.
In Fig. 6 the liquid velocity profile obtained for a cartesian mesh with different $C_d$ are compared showing the effects produced while changing this parameter. It is possible to notice also the different predictions of the liquid velocity close to the tip of the plume both in terms of gradients and magnitude compared to the reference case.

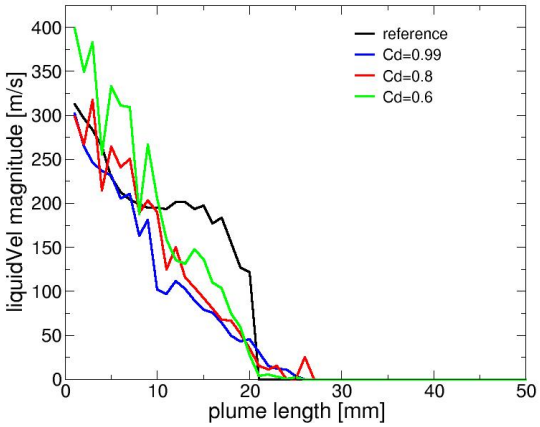


***Fig. 6 - Liquid velocity profile evaluated for a cartesian mesh with different $C_d$ compared to the reference case after 1.6 ms ASOI***

According to the literature, spray-oriented grids allows to obtain more accurate predictions of the spray characteristics without tuning the model parameters, but, in the practice, they are very complex to be designed. Many aspects must be considered to avoid numerical errors. The main issue highlighted from the results is related to the void fraction. When it assumes values close to unity, numerical errors are introduced in the momentum exchange between liquid and vapor phase. The liquid is not slowed down and the surrounding gas suddenly accelerates reaching the same velocity of the liquid drops. High void fraction values are commonly found in spray-oriented grids close to the injection location where the cells are very small. Other issues related to this grid structure are the presence of high aspect-ratio cells (always close to the injector position) and the low quality of the mesh in terms of non-orthogonality and skewness.
The most evident effects of the grid dependency of the results are shown when the air entrainment is evaluated. In Fig. 7 the fuel fraction field shows the effects of the different air entrainment predicted on the air-fuel mixing.

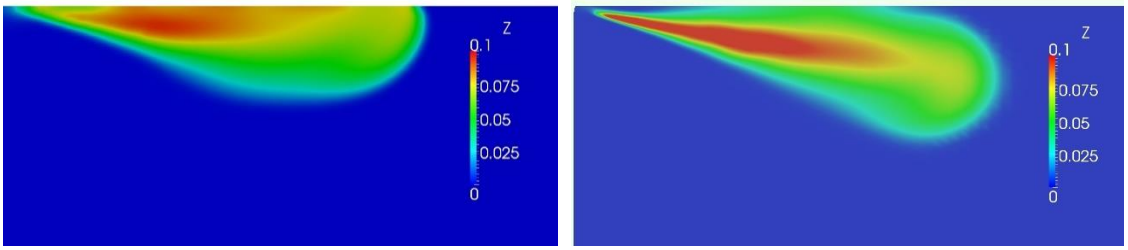


***(a)*** ***(b)***

***Fig. 7 – Profile of the fuel fraction Z evaluated on a cartesian mesh (a) and a spray-oriented grid (b) at the same time step: 1.6 ms after SOI***

**Future Work**

From the numerical perspective it could be interesting to deeply investigate why the spray-oriented grids provide issues in the evaluation of the pressure and velocity gradients.
From the modelling perspective, the development and implementation of new models, such as the KHRTPE, could be a solution to improve the results, since the breakup models adopted in the practice are outdated (the majority of them was developed approximately 30 years ago). This requires also an effort to improve the experimental setup in order to obtain more information about sprays. For example, to better understand the breakup mechanisms, experimental data for both vapor and liquid velocities evaluated in the same location of the spray could be very useful. Moreover, since all the sub-models adopted in the simulation (breakup, turbulence, drag, evaporation) are inherently linked, all of them must be accounted to improve the modelling of the system.
The spray description by Lagrangian-Eulerian approach is proved to be strongly dependent on the grid structure. For this reason, an improvement of the sub-models adopted in the simulation would not be useful if this issue is not overcome. The literature proposes different solutions to reduce the grid-dependency of spray simulations: the Eulerian-Eulerian approach and the so-called ICAS-model (Interactive Cross-sectional Averaged Spray) applied to the Lagrangian-Eulerian are the most interesting. It might be useful to investigate them in order to find a better approach to describe the spray.

# INTRODUCTION

Nowadays, environmental awareness has become of primary importance in the automotive industry, as consequence of government regulations and market dynamics. Indeed, an important part of the research activity is focused on the reduction of emissions and on the increase of engine efficiency. To achieve these objectives, a proper design of the combustion process is fundamental. The air-fuel mixing strongly influences combustion and, hence, it is a matter of intense research. In diesel engines (compressed ignition engines) and Gasoline Direct Injection (GDI) engines the liquid fuel is injected at high pressures directly inside the cylinder creating a spray, whose characteristics are key to understand the air-fuel mixing process. Given their importance, the researchers are investigating sprays both from experimental and numerical point of view.

Numerical techniques, such as CFD, together with experimental measurements are very important to develop and improve the technological solutions adopted in internal combustion (IC) engines. For example, in the specific case of sprays, they allow to understand the physical phenomena that governs atomization, breakup, evaporation and mixture formation.

The Computational Fluid Dynamics (CFD) is an important research tool which offers a wide range of possibilities for the study and the simulation of several applications related to industrial applications. In the field of internal combustion engines, it can be very useful to describe a wide variety of processes such as: the air-fuel mixing, the combustion process and post-treatment of exhausts. CFD allows the engineers to test different configurations, with the same operating conditions, and to achieve accurate results in much less time than what would be required by the corresponding experimental applications.

The numerical modelling of sprays is very complex since it implies the description of a two-phase system with highly turbulent fields and very strong gradients. The use of a Eulerian approach for both the two phases is not feasible since it would require a space discretization fine enough to well describe the injectors channels. Due to the large difference among the length scales that characterize the cylinder geometry and the injector holes, the resulting grid would have too many cells and the simulation would be too much expensive both in terms of time and memory. For this reason, a Lagrangian-Eulerian combined approach is usually adopted: the liquid phase of the system is described by a Lagrangian approach while the gas is described by a Eulerian approach.

Considering the importance and the complexity of the research activity in the internal combustion engine field, Sandia has decided to create the Engine Combustion Network (ECN). ECN is an international collaboration among researchers that collects the contribution of different institutes with the aim to join the efforts in IC engines analysis. GDI and diesel sprays represent a central topic in the research activity proposed by ECN.

Within this contest, this thesis work has been carried out with the main purpose of studying the effects of sub-models and mesh structure on CFD simulation of sprays for IC engines applications. In particular, simulations of the fuel injection inside a constant-

volume vessel have been performed according to the spray G conditions specified by ECN. The spray G configuration corresponds to an early injection case for spray-guided gasoline injection referred to a modern advanced injection system with high pressure capability. The analysis performed in this thesis is part of the research activities carried out by the ICE Group at the Energy Department of Politecnico di Milano in the CFD modelling field, which regard the development of the OpenFOAM numerical code for IC engines simulations.

In the first part of the analysis, a numerical setup for the spray G conditions has been validated comparing the results with experimental data provided by ECN. The setup presented by Politecnico di Milano during the last ECN workshop has been chosen as starting point for this analysis. During the validation, different secondary breakup models have been tested to assess their performances. To do this, their constants have been calibrated and the sensitivity of the numerical results on their variation has been analysed. Moreover, different mesh structures and turbulence models have been tested observing the effects on the numerical results produced.

During the validation process, a strong dependency of the results to the mesh structure has been noticed. For this reason, in the last chapter of this work, a numerical analysis has been performed to deeper investigate the effects produced by the grid structure on the results. A spray configuration typical of diesel engines has been adopted to simplify the numerical description of the problem. The conditions described by this configuration provide a faster evaporation of the fuel. The numerical setup and the sub-models are well established for this kind of simulations, since they have been studied for longer with respect to GDI conditions. The main grid structures adopted in spray simulations for IC engines applications have been analysed studying the numerical effects produced on the results. In simulations which adopt the Lagrangian-Eulerian approach, in addition to the mesh quality (expressed in terms of non-orthogonality, skewness and aspect ratio), also the presence of the Lagrangian parcels and their interaction with the grid must be accounted when the domain is discretized. Together with the choice of the models, a correct grid design is the key to obtain reliable results in spray simulations.

This thesis work is structured as follows:

- In Chapter 1, GDI engines are presented, with focus on their advantages in terms of efficiency and pollutant emissions. After that, the spray G configuration adopted as reference for the first part of the analysis performed in thesis work is described.
- Chapter 2 presents the governing equations of fluid dynamics and the Lagrangian-Eulerian approach commonly adopted to solve sprays problems.
- Chapter 3 briefly introduces turbulence together with the main approaches and models adopted to describe it. Moreover, the spray and its characteristics are described focusing on the breakup models analysed in this work.
- In Chapter 4, the finite volume method is presented to provide the tools necessary to understand the quality of the results in CFD simulations.
- In Chapter 5, the numerical state of art for spray G simulations described during previous ECN workshops is presented together with its results. After that, the performances of different breakup models are assessed trying to improve the spray description provided by the results of the reference setup.

- In Chapter 6, the sensitivity of the results with respect to sub-models and mesh structure is analysed, always referring to the numerical setup defined as state of art.
- In Chapter 7, a numerical analysis is performed with the aim to deeply understand how the mesh structure affects the results provided by CFD sprays simulations.
- Chapter 8 summarizes the results previously obtained and it suggests the guidelines for possible future work on this topic.

# 1. GDI ENGINES AND SPRAY G

In this chapter, the spray G configuration adopted for the CFD simulations is described. This experiment was defined in the context of ECN to analyse the evolution of sprays used in GDI engines.

Also GDI engines are presented according to the description provided by [9]. This is done to understand the importance of spray analysis. The correct description of the spray is the key to predict the air-fuel mixing inside the engine which influences the combustion process. A correct design of the combustion process allows to obtain improvements in terms of engine efficiency and reduction of emissions.

## 1.1. DIRECT INJECTION IN SPARK-IGNITION ENGINES

In GDI engines the fuel is injected directly inside the cylinder, like it is done in compressed-ignition engines; while the combustion process is started by the spark-plug. The main advantages of direct-injection with respect to indirect-injection are a better control of the air-fuel distribution in each cylinder, reduced knock risks and the possibility to run the engine with stratified charge combustion. As cons, emissions become more difficult to handle and the injectors used must be more robust and expensive since they are in direct contact with the high temperatures and pressures present in the cylinder. Moreover, higher injection pressure is required and the time available for the injection process results shorter.

In recent years, in the field of internal combustion engines, the researchers' attention has been focused on the reduction of emissions and on the increase of efficiency without losing performances. By reducing the risk of knock, GDI engines allow to operate with higher pressure inside the cylinder with a consequent increase of efficiency. For the same reason, they give wider possibilities to use turbocharging and to downsize the engine increasing the specific power per unit of weight.

### 1.1.1. Mixture Preparation and Stratified Charge

In GDI engines the mixture is prepared directly inside the cylinder where fuel is injected at high pressure and fresh air is sucked from the intake manifold. The injection system allows to produce a homogeneous mixture simply advancing the injection during the intake stroke. By doing so, air and fuel have a longer time for the mixture homogenization. With this kind of mixture preparation, the GDI engine during combustion behaves like a spark-ignition engine with port fuel indirect injection.

If the injection is done later, during the compression stroke, a stratified charge is obtained. The mixture results richer close to the spark-plug, while it is leaner far from it. The stratified charge allows to create a globally lean mixture and it is convenient in those points of the operating map where the engine works at part load. Figure 1.1 shows the difference between the homogeneous and stratified charge preparation.

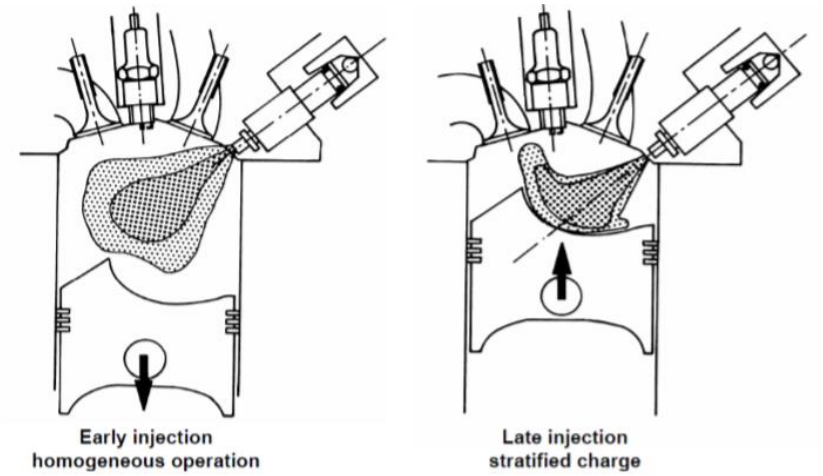


***Figure 1.1 - Preparation of an homogeneous mixture and a stratified charge in GDI engines***

The main techniques commonly adopted to obtain a stratified charge are classified as:

- Wall-guided, where the spray is directed in the wanted direction driven by the shape of piston and combustion chamber
- Air-guided, where the spray is driven by the air motion inside the cylinder created during the intake and power stroke
- Spray-guided, where the spray is injected at high pressure and the multi-hole injector is the main responsible of its characteristics.

Figure 1.2 shows the difference between the techniques mentioned above. Spray-guided techniques are the most commonly used in modern GDI engines because the quick atomization and evaporation of the spray, caused by high injection pressure, allows to reduce the wall-film. Another reason of its usage is the relatively small sensibility of the spray characteristics to the air motion inside the cylinder that can be very variable especially at part load.

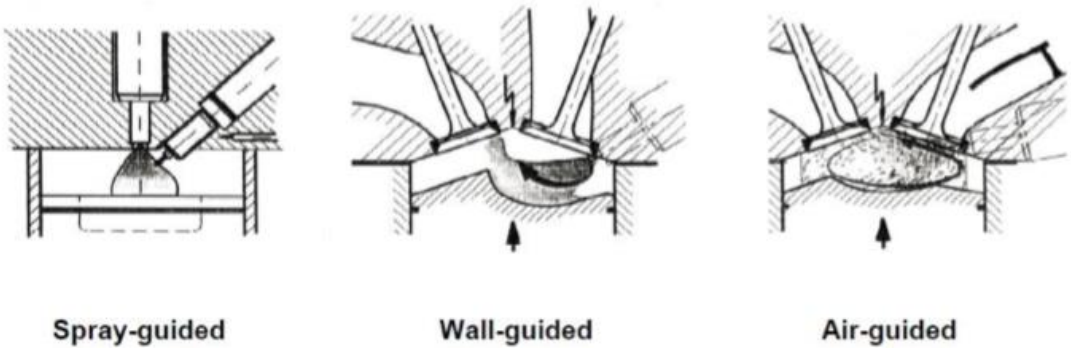


***Figure 1.2 - Representation of the different system for the creation of a stratified charge***

In indirect-injection SI engines, the load is controlled through the use of the throttle valve that regulates the air-fuel mixture introduced inside the cylinder keeping the air-fuel ratio $\lambda$ (defined as the ratio between the mass of air and the mass of fuel in

the mixture) always close to the stoichiometric value. When the load is low, the losses (especially the pumping losses) introduced by this control method become too high and the efficiency of the engine drops. Instead, for Diesel engines, the load is controlled by changing the amount of fuel injected in the cylinder without reducing the mass of air inspired. The mixture becomes globally lean and the efficiency of the engine at part load is still good.

GDI engines combines these two behaviours. When the maximum power is required, there is the possibility to work with homogeneous mixtures at full load, like in indirect-injection SI engines. While, when the engine works at part load, the stratified charge allows to keep a good value of efficiency like in diesel engines. The throttle valve is always present, but differently from indirect-injection engines, it is used only to reach very low loads together with stratified charge. The electronic control unit (ECU) is responsible for the load control; it decides the injection timing and activates the throttle valve as the load changes.

Gasoline is injected at high pressure inside the cylinder; the resulting spray penetrates into the fresh air while the fuel changes phase from liquid to gas. The main mechanisms of phase change are:

- Evaporation: fuel vapour, present on the interface between liquid fuel and surrounding gas, diffuses in the environment. The rate of evaporation is controlled by the diffusion rate.
- Flash boiling: the temperature of the system is higher than the bubble temperature of the fuel computed at the pressure of the system. The liquid is rapidly vaporized and on its surface it is possible to observe the formation of bubbles. The velocity of the phase change is governed by heat transfer.

When an engine is started from cold conditions, these mechanisms represent an advantage for the GDI engine, because the injection at high pressure creates a spray that is composed by very small droplets that can easily evaporate. While for PFI systems fuel is injected at low pressure and we have wall impingement in the intake manifold; if the engine is cold such as the fresh air sucked, there can be problem of fuel evaporation when the engine is started.

Another advantage of GDI engines with respect to PFI engines is the possibility to split the injection process in different events. Like in diesel engines, the multiple injection of fuel offers wider possibilities to optimize the combustion process reducing pollutants and increasing efficiency.

In GDI engines it is crucial to understand and study how the mixture is created and how the fuel vaporizes. By doing so, it is possible to predict the combustion process and consequently control emissions and efficiency of the system.

### 1.1.2. Combustion

Combustion is a complex sequence of elementary reactions that oxidize the fuel. It involves hundreds of species and thousands of reactions. A complete treating of this topic is not the purpose of this work, but, however, it is important to mention something about it, in order to understand the importance of predicting the air-fuel mixing and some of the advantages of GDI engines.

In gasoline engines there is the combustion of a pre-mixed charge of fuel and air both in gas phase. Normal combustion is characterized by two conditions: the ignition of the gasoline is controlled by the spark-plug and after the ignition the flame propagates regularly to the all mixture, without sudden increase of velocity. The combustion is characterized by three phases:

- Initial flame development: immediately after the electric discharge of the spark-plug the small volume of mixture around it is burned and it is gradually transformed into a turbulent flame front.
- Turbulent flame propagation: the turbulent flame propagates rapidly in the whole combustion chamber.
- Burnout: the mixture completes its oxidation behind the flame front during the expansion stroke.

In some conditions it is possible to have the auto-ignition of the fresh charge which has not been reached yet by the flame front. This condition is called knock and it is extremely unwanted because it can seriously damage the mechanical components of the engine and it reduces the performances. It happens where locally pressure and temperature are high enough to give the self-ignition of the fresh mixture. Usually it happens in those points of the combustion chamber that are the last to be reached by the flame front. The advancement of the flame increase temperature and pressure there, creating the condition for auto-ignition before the turbulent flame front arrives. To avoid it, it is necessary to keep the compression ratio low (usually around 10); they are also limited the use of turbocharging and the spark advance. This limits the engine efficiency.

Considering the combustion process, GDI engines, with the stratified charge, have the following advantages with respect to traditional SI engines with homogeneous charge:

- Combustion begins near the plug where the mixture is richer, with consequent high speed of the flame front in the initial part of the process.
- The burning process depends only by the local air/fuel ratio. Therefore, the load can be controlled changing the amount of injected fuel, removing the pumping losses due to throttling.
- Heat losses through the combustion chamber walls are reduced, because the excess air forms an insulating layer between the burned gases and the chamber walls.
- Higher compression ratio (even greater than 12) can be used, since the late injection reduces the time that the mixture spends at high temperature and pressure. So, there is not enough time to have some preliminary reactions necessary to have auto-ignition. In indirect-injection systems air and fuel come in contact before entering the combustion chamber and all these preliminary reactions occur, increasing the risk of knock.
- Higher tolerance to exhaust gas recirculation. This allows to dilute the fresh charge controlling the load and it also has benefits on emissions.

Globally, with higher compression ratio and less losses, especially at low loads, GDI engines are more efficient (up to 25% of potential improvement in fuel economy for some working conditions).

### 1.1.3. Emissions

The main pollutants produced by the combustion inside an engine are $CO_2$, CO, unburned hydrocarbons, nitrogen oxides ($NO_x$) and soot. They can be limited by improving the quality of the fuel, controlling the mixture preparation, monitoring the combustion process and by after-treatment of the exhaust gases. Comparing a GDI engine with a port fuel injection (PFI) engine, these observations can be done:

- $CO_2$ is a product always present in a combustion process that can be generally written as (neglecting the stoichiometric coefficients):

$$fuel + O_2 \rightarrow H_2O + CO_2 \tag{1.1}$$

  It is impossible to avoid the production of $CO_2$ during combustion, the only thing that can be done is to improve the engine efficiency in order to burn less fuel obtaining always the same useful work. By doing so also the $CO_2$ emitted is lower, being the same the power produced. GDI engines performs well from this point of view with respect to PFI engines.
- CO is an intermediate product present in the combustion reactions. Its emissions mainly depend on the air-fuel ratio; they are quite high when the mixture is rich while they rapidly decrease moving toward leaner mixtures. In GDI engines the mixture is almost stoichiometric at full load, while it is lean at part load. PFI engines, instead, work always at stoichiometric conditions; so, direct-injection systems produce less CO while they work at part load.
- Unburned hydrocarbons are produced where the fuel does not burn completely. Their formation depends on many parameters like spark-advance, geometrical parameters of the combustion chamber and, again, on the air-fuel ratio. In GDI engines, at part load, the fuel can be easily oxidized since the mixture is globally lean and the oxidant is largely available. Attention must be payed when the mixture becomes too lean, because the flame front can extinguish before reaching all the fuel. To limit their formation, it is important the correct design of the combustion chamber and of the combustion process.
- $NO_x$ formation is very complex to describe. The Zeldovich mechanism states that they are formed where there are high temperatures (2000 K) and $O_2$ availability. Their production is maximum for slightly lean mixtures, where the adiabatic flame temperature is high and $O_2$ is still available and not completely consumed for combustion. GDI engines typical working conditions are not good from this point of view. However, in direct-injection engines there is a higher tolerance to exhaust gas recirculation (EGR) compared to PFI. This is beneficial for $NO_x$ reduction.
- Soot are carbon particles resulting from incomplete combustion of hydrocarbons. In GDI engines they are formed because of the shorter contact time between air and fuel, that results not enough to complete all the preliminary reactions of combustion. Compared to PFI engines, where there are longer mixing times and where soot emission is not an issue, with GDI engines this is a problem that must managed.

Summing up all the observations, GDI engines performs better than PFI engines especially at part load, with the important exceptions of soot and $NO_x$. However, to meet the strict limits imposed by European regulations it is required the post-treatment of

exhaust. Like in PFI engines it is necessary the three-way catalyst (TWC) to remove CO, $NO_x$ and unburned hydrocarbons. Moreover, in compliance with Euro 6c emission regulation (which is effective from 1 September 2017) also the soot must be removed to avoid emissions above the limit of $6 \cdot 10^{11}$ particles/km. For this reason, in GDI systems, Gasoline Particulate Filters (GPF) similar to Diesel Particulate Filters (DPF) are now necessary.

## 1.2. STATE OF ART AND ACTUAL SITUATION OF THE MARKET

The very first examples of direct-injection systems are dated before the second world war where they were used in the aeronautics. After the war, some automotive applications were present, mainly proposed by Mercedes-Benz. In the following years, GDI engines were studied and developed by Japanese car manufacturers, but the technologies used were not enough advanced to create a product competitive on the market. During the first years of the new millennium, GDI engines have acquired interest exploiting the developments of injection system technologies, due to studies in diesel engines. Now they are widely adopted by car manufacturers since they present a lot of advantages with respect to traditional PFI engines.

Today the most advanced example of GDI engine is represented by the SkyActiv technology produced by Mazda [10] (available on the market starting from 2012) with an engine compression ratio of 14, the highest among gasoline engines. Such value has been reached through the use of direct injection, a peculiar design of the piston head and a proper tuning of the exhaust manifold. This allows to avoid knock even with such extreme conditions.

The passenger cars global market is increasing continuously after the economic crisis of 2007, mainly due to the contribution of developing countries. According to the data provided by [11], 2018 has been the first year since 2009 that has registered a decrease of sales; in fact, 78.7 million cars were sold compared to 79 million of 2017. However, this is only a small drop compared to values around 50 million of car sales registered before 2009. Analysing the European market, where more detailed data are provided by [12], it is possible to notice that the share of gasoline engines on the market is increasing at the expense of diesel cars. This trend has become more evident after the Dieselgate scandal of 2015 and after the driving restrictions imposed in recent years in some areas of the continent, especially to cars powered by diesel fuel. During 2011-2012 diesel car share of the market was equal to 55% while it dropped to 45% during 2017. Among gasoline cars, the share of GDI engines is increasing year by year and during 2017 they reached quite the 50% of the total gasoline vehicles registrations; before 2008 this percentage has always been less than 10%. This is a consequence of the choices made by car manufacturers that are producing GDI engines because of their advantages and efficiency.

## 1.3. SPRAY G AND ENGINE COMBUSTION NETWORK

The Engine Combustion Network (ECN) [1] is an international collaboration among researchers in engine combustion involving both experimental and computational

aspects. It is promoted by Sandia National Laboratories and receives the contribution of many partners from different countries, including also Politecnico di Milano. The objectives of ECN are to:

- Establish an internet library of experiments that are appropriate for model validation and the advancement of scientific understanding of combustions in engines.
- Provide a framework for collaborative comparison of measured and modelled results
- Identify priorities for further experimental and computational research.

Regarding GDI engines, the ECN working group has identified a few experimental conditions that will be the focus of modeller and experimentalists. It has been decided to fix these setups to standardise experiments and numerical simulations. The spray G condition corresponds to a non-reacting early injection case for spray-guided gasoline injection. The specifications given by ECN refer to a modern advanced injection system with high pressure capability. The objective is to study and model the spray development and the air-fuel mixing before the combustion; this has a great influence on the combustion process and consequently on the engine operations. The boundary conditions for ambient and injector quantities are fixed and listed in Table 1-1.

| **Spray G operating conditions of ECN** | |
|---|---|
| Ambient gas temperature | 573 K |
| Ambient gas pressure | 6.0 bar |
| Ambient gas density | 3.5 kg/m$^3$ |
| Ambient gas oxygen (by volume) | 0% of $O_2$ |
| Ambient gas velocity | Near-quiescent, less than 1m/s |
| Fuel injection pressure | 20 MPa, prior to start of the injection |
| Fuel | Iso-octane |
| Fuel temperature at nozzle | 363 K |
| Injection mass | 10 mg |
| Electronic injection duration | 680 µs |
| Actual injection duration | 780 µs |

***Table 1-1 - Boundary conditions of ambient and injector quantities for Spray G***

The combination of gas properties corresponds to a particular set of gases composed by 89.71% $N_2$, 6.52% $CO_2$ and 3.77% $H_2O$ by volume. Moreover, ECN provides the injection law for this specific set of operating conditions.

The specifications for the multi-hole injector correspond to the ones adopted in a modern high-pressure system, in particular, they refer to the Delphi solenoid-activated injector, that is the one adopted for experimental measurements. The fuel is injected by eight identical holes disposed around a central axis of symmetry. The injection hole location (corresponding to the level identified by z'=0 in Figure 1.3) is positioned at the bottom of a counterbore with a diameter of 0.388 mm. The injection orifice diameter is

equal to 0.165 mm. More detailed information about it are provided in Figure 1.3 and in Table 1-2.

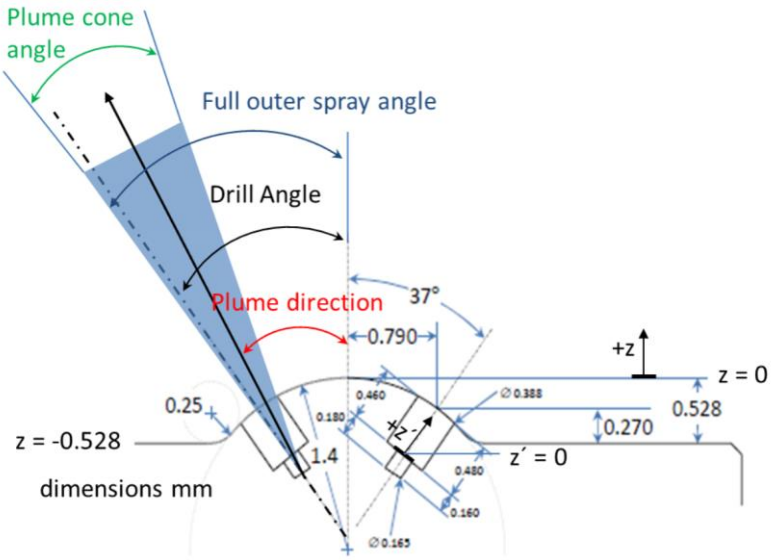


***Figure 1.3 - Detailed nozzle geometry for Spray G***

| | |
|---|---|
| Number of holes | 8 |
| Spray shape | circular |
| Bend angle | 0° |
| L/D ratio | 1.4 |
| Hole shape | Straight |
| Flow rate | 15cc/s @ 10 MPa |
| Nozzle type | Valve-covered orifice (VCO) |
| Nozzle shape | Step hole |
| Orifice diameter | 0.165 mm |
| Orifice length | 0.16-0.18 mm |
| Step diameter | 0.388 mm |
| Orifice drill angle | 37° relative to nozzle axis |
| Full outer spray angle | 80° |

***Table 1-2 - Specifications for the nozzle geometry of Spray G***

### 1.3.1. Experimental Apparatus

The numerical simulations presented in this work are compared to experimental results published on the ECN website. The experimental data available have been obtained by the ECN partners following the specification described in the previous

paragraph. The results are obtained through optical techniques such as DBI (diffused back-illumination) and schlieren imaging.

The vapor boundary of gasoline sprays is obtained through schlieren imaging. The experimental apparatus used to collect data (Figure 1.4) is composed by an optical accessible constant-volume vessel under the conditions specified by ECN. The chamber has a cubical shape and it is approximately one liter in volume. Each side of the geometry is equipped with a port. The injector is mounted in one of the side ports, while the other ports are fitted with sapphire windows to provide the optical access. A single high-speed LED is used as a schlieren light source and the light produced is focused onto a diffuser to produce a uniform light intensity. The system of mirrors allows to produce a beam approximately 150 mm in diameter. Schlieren images are obtained by a high-speed digital camera.

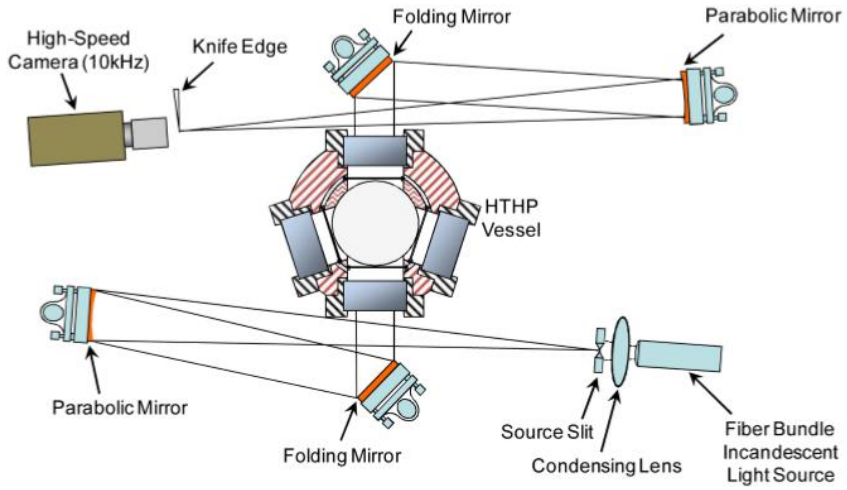


***Figure 1.4 - Experimental apparatus for schlieren imaging***

Schlieren imaging system has been used for long to image fluid phenomena. Both liquid and vapor phases of fuel contribute to the schlieren signature and it is impossible to distinguish one from the other. This technique is based on the fact that fuel (no matter if it is in liquid or vapor phase) adsorbs light differently from the surrounding inert gas, so, the image produced presents different level of lighting depending on how much fuel the light crossed in its path.

DBI imaging is recommended by ECN website and SAE J2715 standard for liquid-phase measurements. It uses the extinction produced by the spray droplets to provide a measure related to the liquid volume fraction along the path of the light. Since the environment has high temperature and pressure, care must be taken to ensure that the diagnostic is not sensitive to vapor phase beam steering from temperature/refractive index gradients. The diffuser and collector angles need to be calibrated for a given setup; while the camera needs to be configured to accurately measure background intensity, with no transmitted DBI light. The experimental apparatus is very similar to the one described for schlieren imaging and it is shown in Figure 1.5.

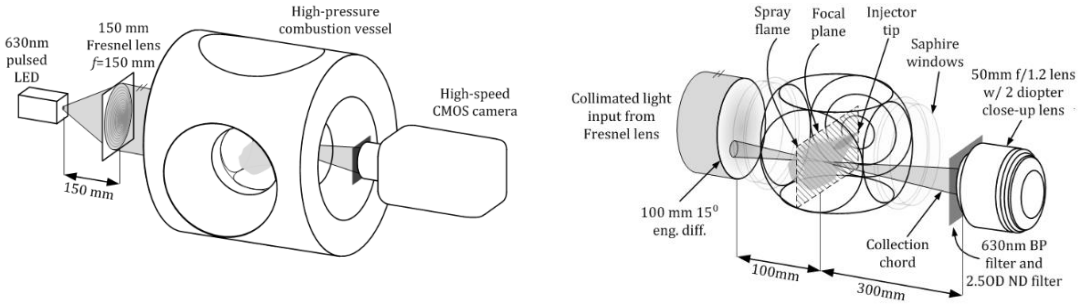


***(a)*** ***(b)***

***Figure 1.5 - Optical arrangement (a) and close up of the combustion chamber (b) for DBI imaging***

# 2. FLUID-DYNAMICS AND GOVERNING EQUATIONS

Fluid dynamics is a branch of continuum mechanics that studies the motion of fluids (liquids or gases).

The fluid behaviour is governed by the conservation equations which are expressed in the Navier-Stokes formulation. To solve fluid dynamics problems, it is necessary the resolution of sets of non-linear, partial differential equations in which the unknowns are scalars and vectors that can be both space and time dependent. Only for few cases, after several assumptions and simplifications, it is possible to solve them analytically. When this is not feasible, space and time can be discretized into numerous finite volumes and time steps. By doing so, the governing equations can be numerically integrated and the problem turns into a system of algebraic equations, which can be solved using iterative methods.

The presence of a spray injected into an inert gas creates a two-phase system with highly turbulent fields and very strong gradients. To completely describe it and to reduce the amount of memory and time necessary, this kind of problems are solved using a Lagrangian approach for the liquid dispersed phase coupled with an Eulerian approach for the gas phase.

A complete theoretical discussion about the governing equations of fluid dynamics is presented in [13] and [14]; this chapter reports only the main results.

## 2.1. THE GAS PHASE

The gas phase of the system is treated using an Eulerian approach: a finite control volume is fixed in space and then all the conservation equations are expressed as the balance between all the terms (accumulation, convection, diffusion and source terms) that increase or decrease the generic flow variable $\Phi$ inside the volume itself:

$$\begin{bmatrix} Rate\ of\ change \\ of\ \Phi\ in\ the \\ control\ volume \\ with\ respect\ to \\ time \end{bmatrix} = \begin{bmatrix} Net\ rate\ of \\ increase\ of \\ \Phi\ due\ to \\ convection \end{bmatrix} + \begin{bmatrix} Net\ rate\ of \\ increase\ of \\ \Phi\ due\ to \\ diffusion \end{bmatrix} + \begin{bmatrix} Net\ rate\ of \\ creation\ of \\ \Phi\ inside \\ the\ volume \end{bmatrix}$$

The conservation equations written following the Eulerian approach describe only the behaviour of the gas phase and the interactions with the Lagrangian dispersed phase are accounted in the source terms.

### 2.1.1. Mass Conservation Equation

Once it is given a fixed and finite control volume, the mass conservation equation can be written as:

$$\frac{\partial \rho}{\partial t} + \nabla \cdot (\rho \boldsymbol{u}) = S_m^l \tag{2.1}$$

On the left-hand side of the equation, the first term expresses the variation of mass during time while the second one represents the net mass flux through the boundaries of the control volume. On the right-hand side there is the source term that accounts for the variation of mass due to evaporation or condensation of the liquid phase droplets.

### 2.1.2. Species Conservation Equation

Since the system is made up by a multicomponent mixture (fuel and inert gas) it is possible to write the mass conservation for each species. The equation written below can be easily obtained starting from (2.1):

$$\frac{\partial (\rho Y_i)}{\partial t} + \nabla \cdot (\rho Y_i \boldsymbol{u}) = S_{Y_i}^l + S_{chem} \tag{2.2}$$

where $Y_i$ is the mass fraction of the i-th species defined as:

$$Y_i = \frac{\rho_i}{\rho} \tag{2.3}$$

Again, on the left-hand side of the equation (2.2), there are the time dependant term and the term that accounts for the flux through the boundaries. On the right-hand side there are two source terms: the first one accounts for evaporation and condensation of the liquid, the second one accounts for the production or consumption of the $i$-th species due to chemical reactions. If the system is non-reacting this last term is equal to zero. Moreover, to be consistent with the global mass balance, in a system composed by n species, it must be verified the following relation:

$$\sum_i^n S_{Y_i}^l = S_m^l \tag{2.4}$$

### 2.1.3. Momentum Conservation Equation

The momentum conservation is obtained directly from the Newton's II law, that sets:

$$\frac{d\boldsymbol{q}}{dt} = \frac{d(m\boldsymbol{u})}{dt} = \boldsymbol{F} \tag{2.5}$$

The variation of the momentum during time is equal to the sum of all the forces acting on the system. It is possible to distinguish between surface forces, acting on the boundaries of the system like pressure and viscous forces; and body forces like gravity, electromagnetic and other external forces acting on the whole volume.

By manipulating the Newton's II law and explaining all the terms it is obtained the momentum conservation equation:

$$\frac{\partial (\rho \boldsymbol{u})}{\partial t} + \nabla \cdot (\rho \boldsymbol{u}\boldsymbol{u}) = -\nabla p + \nabla \cdot \boldsymbol{\tau} + \rho \boldsymbol{g} + \boldsymbol{S_u^l} \tag{2.6}$$

On the left-hand side there are the time dependant term and the term that accounts for the flux of momentum through the boundary. On the right-hand side the following terms are present:

- $-\nabla p$ identify the gradient of pressure
- $\nabla \cdot \boldsymbol{\tau}$ is the divergence of the tensor of the viscous stresses
- $\rho \boldsymbol{g}$ represents the gravity force per unit volume
- $\boldsymbol{S_u^l}$ is the source term that accounts for the exchange of momentum between the liquid and gas phase.

### 2.1.4. Energy Conservation Equation

The energy conservation equation derives from the first principle of thermodynamics:

$$\frac{\partial(\rho e)}{\partial t} + \nabla \cdot (\rho e \boldsymbol{u}) = Q_{vol} + \nabla \cdot \boldsymbol{Q_s} \tag{2.7}$$

where e is the total energy per unit mass defined as the sum between the internal energy per unit mass $i$ and the kinetic energy per unit mass $u^2/2$. The source term $Q_{vol}$ accounts for production or dissipation of energy inside the control volume. The source term $\boldsymbol{Q_s}$, instead, accounts for the contribution of surface sources of energy like the diffusion of heat through the boundaries or the work done by the pressure and viscous stresses.
Making explicit all the source term, the energy conservation equation assumes this form:

$$\frac{\partial(\rho e)}{\partial t} + \nabla \cdot (\rho e \boldsymbol{u}) = -\nabla \cdot (p \boldsymbol{u}) + \nabla \cdot (\boldsymbol{\tau} \cdot \boldsymbol{u}) + \nabla \cdot (k \nabla T) + \rho \boldsymbol{g} \cdot \boldsymbol{u} + S_e^l + \dot{Q}_{chem} \tag{2.8}$$

### 2.1.5. Viscous stress modelling and Navier-Stokes equations

In the previous equations the tensor $\boldsymbol{\tau}$ of the viscous stresses appears. Adopting the hypothesis of Newtonian fluid, some expressions are introduced to relate the viscous stresses to the properties of the fluid and to the velocity vector $\boldsymbol{u}$. For a Newtonian fluid the viscous stresses are proportional to the rates of deformation $s_{i,j}$ according to:

$$\tau_{i,j} = \mu \, s_{i,j} = \mu \left( \frac{\partial u_j}{\partial x_i} + \frac{\partial u_i}{\partial x_j} \right) + \lambda (\nabla \cdot \boldsymbol{u}) \delta_{i,j} \tag{2.9}$$

$\mu$ is the dynamic viscosity and $\lambda$ is the so-called second viscosity. Not much is known about $\lambda$ and in practice its effect is small. A good approximation for gas is $\lambda = -\frac{2}{3}\mu$ (Schlichting, 1979). The term $\delta_{i,j}$ is the Kronecker delta by which $\delta_{i,j} = 1$ if $i = j$, otherwise $\delta_{i,j} = 0$.
Substitution of the expression (2.9) in the previous conservation equations (2.6) and (2.8) yields the Navier-Stokes equations. For the momentum conservation:

$$\frac{\partial(\rho \boldsymbol{u})}{\partial t} + \nabla \cdot (\rho \boldsymbol{u} \boldsymbol{u}) = -\nabla p + \nabla \cdot \mu (\nabla \boldsymbol{u}) + \rho \boldsymbol{g} + \boldsymbol{S_u^l} \tag{2.10}$$

and for energy conservation:

$$\frac{\partial(\rho e)}{\partial t} + \nabla \cdot (\rho e \boldsymbol{u}) = -\nabla \cdot (p\boldsymbol{u}) + \Phi + \nabla \cdot (k\nabla T) + \rho \boldsymbol{g} \cdot \boldsymbol{u} + S_e^l + \dot{Q}_{chem} \quad (2.11)$$

$\Phi$ is the dissipation function and describes all the effects due to viscous stresses. It is defined as:

$$\Phi = \mu\left\{2\left[\left(\frac{\partial u}{\partial x}\right)^2 + \left(\frac{\partial v}{\partial y}\right)^2 + \left(\frac{\partial w}{\partial z}\right)^2\right] + \left(\frac{\partial u}{\partial y} + \frac{\partial v}{\partial x}\right)^2 + \left(\frac{\partial u}{\partial z} + \frac{\partial w}{\partial x}\right)^2 + \left(\frac{\partial w}{\partial y} + \frac{\partial v}{\partial z}\right)^2\right\} + \lambda(\nabla \cdot u)^2 \quad (2.12)$$

### 2.1.6. Equations of State

Considering all the equations obtained up to now and a single component system, the fluid dynamic problem has 7 unknowns ($p$, $T$, $\rho$, $i$ and the three components of $\boldsymbol{u}$) and 5 equations (mass conservation; energy conservation; x, y and z momentum equation). To close the system and to obtain a set of equations that can be solved, they are needed other 2 relation between the unknowns.

The equations of state allow to relate the physical properties of the fluid through the assumption of thermodynamic equilibrium. This hypothesis is considered valid over a large amount of different cases, the only exceptions are flows with strong shock waves, but this is not the case of gasoline or diesel sprays. It is possible to describe completely the state of a substance using only two state variables and then the equations of state relate the other variables to the previous two. For example, if $T$ and $\rho$ are used as state variables there will be two equations for $p$ and $i$:

$$p = p(\rho, T) \quad and \quad i = i(\rho, T) \quad (2.13)$$

For an ideal gas the equations of state can be expressed as follows:

$$p = \rho RT \quad and \quad i = C_v T \quad (2.14)$$

The equations of state allow to have a set of 7 equations in 7 unknows for a single component system. By doing so, it is possible to find a solution for the fluid dynamic problem. If the system has more than one component, there are other n unknowns (being $n$ the number of components) corresponding to the mass fractions $Y_i$. In this case to close the problem it must be used $n$ - 1 species conservation equations and the relation:

$$\sum_i^n Y_i = 1 \quad (2.15)$$

## 2.2. THE LIQUID PHASE

The liquid phase of the system is treated using a Lagrangian approach. In this case the attention is focused on an individual fluid parcel and its motion is tracked through space and time. The only independent variable becomes the time, while all the other quantities depend on it.

The use of a Lagrangian approach for the liquid phase is necessary to save memory and computational time. Indeed, the use of an Eulerian approach also for the liquid dispersed phase in this kind of problems should have required a space discretization of

the computational mesh fine enough to well describe the injector. Only if it was done, it would be possible to capture all the phenomena related to the liquid injection. Since the injector diameter is in the order of $10^{-4}$ m and the characteristic dimension of the system is in the order of $10^{-1} – 10^{-2}$ m, the resulting mesh with such characteristics would have too many cells and the simulations would be too much expensive both in terms of time and memory.

The Lagrangian approach allows to describe the spray using a statistical method called Discrete Droplet Model (DDM) [2]. It features a Monte-Carlo based solution technique for the spray equation, that describe the spray droplets by stochastic particles which are usually called parcels [15]. These parcels are individual mass points that can be viewed as representative classes of identical, non-interacting droplets. This means that a parcel represents a certain number of real existing droplets with the same characteristics (same shape, dimension, velocity, temperature …) and the same fluid-dynamic behaviour. Instead of solving the conservation equations for each single droplet (approximately their number is in the order of $10^6$-$10^8$), it allows to simulate the spray by computing the behaviour of a user-defined number of parcels, reducing the memory and time requirements. As the number of parcels in the spray is increased, the spray statistics are improved, but this imply an increase of computational costs. A number of parcels in the order of $10^4 – 10^5$ is commonly used.

The liquid phase needs the solution of the conservation equations, likely the gas phase, supported by models to describe injection, breakup, evaporation, heat exchange, aerodynamic force and wall-film interaction. Some of these models will be discussed in chapter 3.

It is important to remember that gas and liquid interact one with the other exchanging mass, energy and momentum. While for the gas phase suitable source terms are included in the conservation equations, for the liquid phase this interaction is considered by imposing as boundary conditions for the parcel the actual data of the cell that is crossed by the parcel itself in a specific time step.

### 2.2.1. The Droplet Mass Equation

To write the equation of mass conservation it is assumed that the liquid droplets are spheres with diameter $D$. The mass balance has the following expression that is experimentally validated:

$$\frac{dD^2}{dt} = C_{eva} \tag{2.16}$$

Anyway, it is a common practise to refer to mass variation during time once evaporation is studied:

$$\dot{m}_d = \frac{dm_d}{dt} = -\pi D \Gamma \rho_v ln\left(1 + \frac{Y_{v,s} - Y_{v,\infty}}{1 - Y_{v,s}}\right) Sh \tag{2.17}$$

in this equation $\rho_v$ is the density of the vapor close to the drop computed using the ideal gas law, $\Gamma$ is the mass diffusion coefficient, $Sh$ is the Sherwood number, $Y_{v,\infty}$ and $Y_{v,s}$ are the mass fractions of fuel vapours respectively evaluated in a point sufficiently far from the drop and close to the interface between the two phases at saturation condition. The

Sherwood number accounts for the relative motion between the gas and liquid droplet that influences the evaporation rate. A correlation is used to compute $Sh$ as function of Reynolds and Schmidt numbers:

$$Sh = 2.0 + 0.6\sqrt{Re}\,\sqrt[3]{Sc} \tag{2.18}$$

where the others dimensionless numbers are defined as:

$$Sc = \frac{\mu}{\rho D} \quad and \quad Re = \frac{\rho|\boldsymbol{u}_d - \boldsymbol{u}|D}{\mu} \tag{2.19}$$

In the $Re$ number is used the relative velocity between the fluid and the surrounding gas. Usually the equation (2.17) is managed and written in the following manner:

$$\dot{m}_d = \frac{dm_d}{dt} = -\frac{m_d}{\tau_e} \tag{2.20}$$

where $\tau_e$ is the evaporation relaxation time and it is defined as:

$$\tau_e = \frac{m_d}{\pi D \Gamma \rho_v ln(1+B) Sh} \tag{2.21}$$

$B$ is called Spalding number and it has the following expression:

$$B = \left(1 + \frac{Y_{v,s} - Y_{v,\infty}}{1 - Y_{v,s}}\right) \tag{2.22}$$

The equations obtained up to now, in particular (2.17) and (2.20), are valid in situations where only the evaporation phenomenon is present without boiling. If there is also the presence of boiling, the evaporation pressure approaches the pressure of the system. This would lead to have $B \rightarrow 0$ and $\tau_e \rightarrow \infty$, so that the evaporation rate would increase up to infinite. Obviously, this situation is not physical and the droplet mass equation must be corrected to account the fact that, during boiling, the phase change is controlled by heat exchange, rather than diffusive phenomena typical of evaporating sprays.

### 2.2.2. The Equation of Motion

The momentum equation, from the Newton's II law, for a discrete particle is:

$$\frac{d\boldsymbol{q}_d}{dt} = \frac{d(m_d \boldsymbol{u}_d)}{dt} = \boldsymbol{F} \tag{2.23}$$

where $m_d$ is the droplet mass, $\boldsymbol{u}_d$ is the droplet velocity and $\boldsymbol{F}$ is the resulting of all the forces acting on the parcel. The most general form of $\boldsymbol{F}$ is represented by the BBO equation, from the work of Basset (1888), Boussinesq (1903) and Oseen (1927). In systems like gasoline and diesel sprays, where the density ratio between the liquid and vapor phase is of the order of $10^2$ or higher, it is possible to neglect the added mass, Basset, Magnus, Saffman, pressure and buoyancy forces. So, at the end, the BBO equation is reduced to (2.24), and it contains just drag and gravitational force.

$$\boldsymbol{F} = -\frac{\pi D^2}{8}\rho C_d |\boldsymbol{u}_d - \boldsymbol{u}|(\boldsymbol{u}_d - \boldsymbol{u}) + m_d \boldsymbol{g} \tag{2.24}$$

$D$ is the parcel diameter, $\rho$ is the liquid density, $C_d$ is the drag coefficient, $\boldsymbol{u}$ is the velocity of the gas and $\boldsymbol{g}$ the gravitational acceleration.

By substituting the expression found for $\boldsymbol{F}$ (2.24) in the momentum equation (2.23), the following equation can be written:

$$\frac{d\boldsymbol{u}_d}{dt} = -\frac{\boldsymbol{u}_d - \boldsymbol{u}}{\tau_u} + \boldsymbol{g} \tag{2.25}$$

Where $\tau_u$ is the momentum relaxation time and it is defined as:

$$\tau_u = \frac{8\, m_d}{\pi D^2 \rho C_d |\boldsymbol{u}_d - \boldsymbol{u}|} = \frac{4\, D}{3 C_d |\boldsymbol{u}_d - \boldsymbol{u}|} \tag{2.26}$$

### 2.2.3. The Droplet Energy Equation

The liquid parcel exchanges energy with the surrounding gas. The heat transferred from the gas to the droplet is used to increase the temperature of the fuel and to evaporate it. Evaporation is always present unless the gas is saturated with fuel vapor; therefore, if the energy provided by the gas is not enough the droplet temperature will decrease. The energy equation for the liquid droplet is:

$$m_d \frac{dh_d}{dt} = \dot{m}_d h_v(T_d) + \pi D k_g Nu (T - T_d) f \tag{2.27}$$

Where $\dot{m}_d$ has been already defined in (2.17), $h_v(T_d)$ is the latent heat of evaporation at the temperature $T_d$, $k_g$ is the thermal conductivity of the gas phase, $Nu$ is the Nusselt number and it can be expressed as function of $Re$ and $Pr$ using the Ranz-Marshall correlation:

$$Nu = 2.0 + 0.6\sqrt{Re}\,\sqrt[3]{Pr} \tag{2.28}$$

This equation is very similar to (2.18) because there is an analogy between heat and mass transfer. The last term of equation (2.27) is $f$ that is a correcting factor which adjusts the rate of heat exchange accounting for the presence of mass transfer. It can be expressed as

$$f = \frac{z}{e^z - 1}, \qquad z = -\frac{c_{p,v}\dot{m}_d}{\pi D k_g Nu} \tag{2.29}$$

Similarly to droplet mass and momentum equations, it is possible to define the heat transfer relaxation time $\tau_h$, defined as:

$$\tau_h = \frac{m_d c_l}{\pi D k_g Nu} \tag{2.30}$$

So, finally, the equation (2.27) can be rewritten as:

$$\frac{dT_d}{dt} = \frac{T - T_d}{\tau_h} f - \frac{h_v(T_d)}{c_l\, \tau_e} \tag{2.31}$$

Where $\tau_e$ has already been defined in (2.21).

## 2.3. EULERIAN-LAGRANGIAN COUPLING

As discussed in this chapter, the gas phase and the dispersed liquid are treated using two different approaches. Now it is important to understand how the two phases interact one with the other, since they exchange mass, momentum and energy. The liquid parcels, treated as points with mass and physical properties, account for the presence of the gas with proper boundary conditions, while the gas phase includes source terms that are representative of the liquid effects on the gas.

Once the problem is discretized, both in time and space, to set the boundary conditions and to solve the source terms it is fundamental to determine the position of each parcel and to identify to which cell it belongs. This must be done for each time step.

### 2.3.1. Parcel Tracking Methods

Tracking a parcel means not only to determine its location in space, but also identify the owner cell. Only by doing so, it is possible to impose as boundary condition of a parcel the actual values assumed by each flow property inside the owner cell. There are two main approaches for the parcel tracking: the Lose-Find (LF) algorithm and the Face-to-Face (F2F) algorithm.

The LF algorithm does not account for the mesh when moves the particle. Starting from the initial position the liquid drop is moved along its path by $\boldsymbol{u_d}\Delta t$ to find the final position. Once this is done, the algorithm performs a research to find out the owner cell corresponding to the parcel location.

F2F algorithm searches the parcel position only when it is introduced in the system. To track all the subsequent movements, it determines if the particles leaves the owner cell in the time step $\Delta t$ or not. To do so, the following quantity is defined:

$$\lambda_i = \frac{(\boldsymbol{c_i} - \boldsymbol{x})\hat{\boldsymbol{n}}_{\boldsymbol{i}}}{(\boldsymbol{u_d}\Delta t\,)\hat{\boldsymbol{n}}_{\boldsymbol{i}}} \tag{2.32}$$

where $\boldsymbol{x}$ is the position of the parcel, $\boldsymbol{c_i}$ the position of the face centre and $\hat{\boldsymbol{n}}_{\boldsymbol{i}}$ the normal that points outward of the cell face. If $\lambda_i$ is greater than 1 the parcel does not leave the cell through the $i$-th face. Otherwise it leaves the cell crossing the face considered.

# 3. TURBULENCE AND SPRAY MODELLING

As previously mentioned, the spray injection creates a highly turbulent field in the inert gas. To correctly describe the fluid behaviour, it is important to understand what turbulence is and how it affects the fluid properties. Since in most of the applications, the characteristic length and time scales involved have a very wide range, it is difficult to completely describe a turbulent flow without excessive costs and computational time. That is why some models able to replicate the effects of turbulence on the mean flow saving time and costs are adopted. To do this, some simplifications must be introduced. The study of these models is fundamental to understand their strengths and weaknesses and consequently to make a critical analysis of the results obtained.

At the same time, while studying the spray injection process, it is needed to precisely define the main spray characteristics to avoid inconsistencies while comparing results from different institutes. Also for the sprays, some models are introduced to describe their formation and evolution saving time and costs.

## 3.1. INTRODUCTION TO TURBULENCE

The following brief description of turbulence is inspired by the analogous work done by Versteeg and Malalasekera in [14].

Turbulence is a three-dimensional and intrinsically unsteady phenomenon. It involves random and chaotic fluctuations of the flow properties, like velocity and pressure. Turbulence can be present even when there are steady boundary conditions and very simple geometries.

Experimental evidences show how every fluid system passes from a laminar and ordered regime, called laminar flow, to a turbulent regime once it is reached and overcome a critical value of the Reynolds number $Re_{cr}$, that is typical of the system itself. The Reynolds number is the ratio between the order of magnitude of the inertia forces and the order of magnitude of the viscous forces. The first ones tend to create and maintain the turbulence while the last ones oppose the instabilities.

$$Re = \frac{inertia\ forces}{viscous\ forces} = \frac{uL}{\nu} \tag{3.1}$$

The random nature of a turbulent flow makes difficult the description of the fluid motion. To simplify the problem, it is used the so-called Reynolds decomposition: a generic quantity $\varphi$ can be decomposed into a steady mean value $\Phi$ plus a fluctuating component $\varphi'$:

$$\varphi(\mathbf{x},t) = \Phi(\mathbf{x}) + \varphi'(\mathbf{x},t) \tag{3.2}$$

A graphical example of a fluctuating quantity in turbulent flow and its Reynolds decomposition is shown in Figure 3.1. For mean steady state turbulent flows $\Phi$ is the

average value of $\varphi$; while if it is considered a time dependant flow, $\Phi$ becomes the ensemble average of $\varphi'$ over a large number of repeated identical experiments.

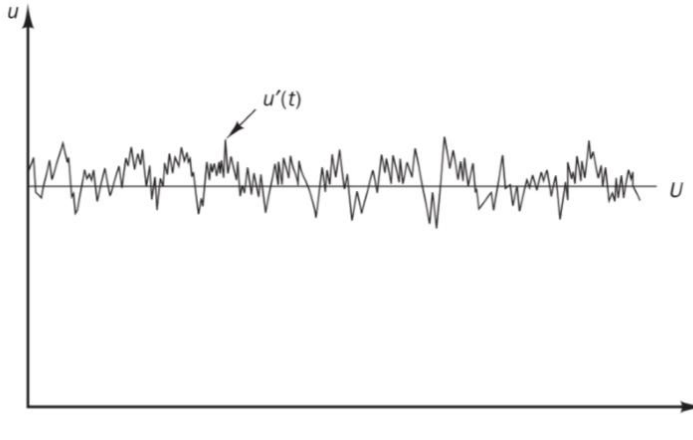


***Figure 3.1 - Typical point velocity measurement in turbulent flow***

In turbulent flows the presence of rotational flow structures is observed, called turbulent eddies, with a wide range of length scales. The large eddies have characteristic length scale $l$ and characteristic velocity $\theta$ of the same order of length scale $L$ and velocity scale $u$ of the mean flow. Hence, their Reynolds number $Re_l = \theta l / \nu$ is not very different from the Reynolds number of the mean flow $Re$, defined in (3.1). Large eddies have an inviscid behaviour and the inertia forces prevail on the viscous dissipation. They interact with the mean flow extracting energy from it by a process called vortex stretching. This energy exchange is done by means of the shear stresses that distort the rotational eddies. Large eddies are highly anisotropic and strongly affected by boundary conditions.

Smaller eddies are similarly stretched by larger eddies; in this way the kinetic energy is transferred from the mean flow to progressively smaller eddies, in a process called energy cascade. As the radius of the vortexes decreases, the rotational velocity increases because of the momentum conservation; also the gradients of velocity increase and with them the viscous stresses rise, dissipating the kinetic energy into thermal energy. So, the energy is transferred from the mean flow to large eddies and then to small eddies, where it is dissipated by viscous effects.

All the fluctuating properties of a fluid contain energy across a wide range of frequencies. It is possible to notice that in Figure 3.2 where the spectral energy $E(k)$ (kinetic energy per unit mas and wavenumber) is shown as a function of the wavenumber defined as:

$$k = \frac{2\pi f}{u} \tag{3.3}$$

where $f$ is the frequency of the vortex. At high wavenumbers it is possible to find small eddies with higher frequencies.

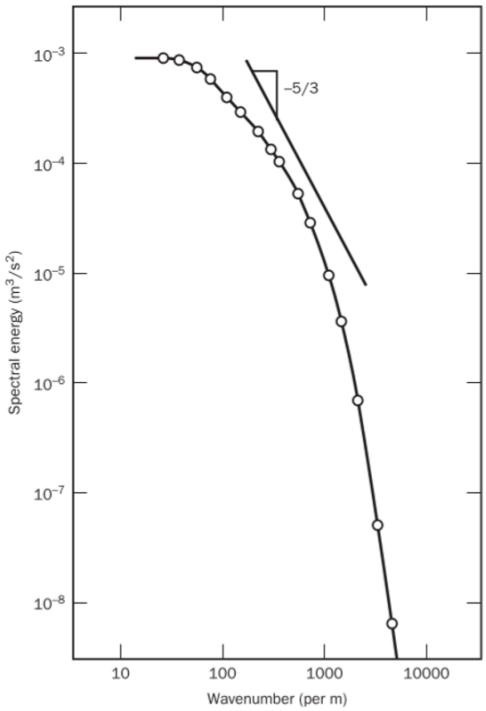


***Figure 3.2 - Energy spectrum of turbulence***

The smallest scale motion in a turbulent flow is called Kolmogorov scale. The vortexes that belong to it are isotropic, dominated by viscous effects and their Reynolds number is approximately equal to 1. It is possible to find estimates of their characteristic lengths, velocities and times (respectively η, $v$ and $\tau$):

$$\frac{\eta}{L} \approx Re_L^{-\frac{3}{4}} \qquad \frac{v}{u} \approx Re_L^{-\frac{1}{4}} \qquad \frac{\tau}{T} \approx Re_L^{-\frac{1}{2}} \tag{3.4}$$

$L$, $T$, $u$ and $Re_L$ are the corresponding properties evaluated on the mean flow. From equations (3.4) it is possible to obtain the smallest times and lengths that need to be captured during a simulation to completely describe the fluid flow. As $Re_L$ increases, the difference between micro scales and mean flow scales, called scale separation, becomes greater and consequently more computational time will be required to solve the problem.

## 3.2. TURBULENCE MODELLING

Turbulence creates eddies with a wide range of time and length scales interacting in a complex way. Different numerical methods to simulate turbulent flows have been developed and they can be grouped into the following three categories:

- **RANS (Reynolds averaged Navier-Stokes) equations**: the attention is focused on the mean flow and on the effects that turbulence has on it. The Navier-Stokes equations are time averaged (or ensemble averaged if the boundary conditions are time dependant) and then some models are used

to describe the interactions between turbulent eddies and mean flow. Practically only the mean flow is simulated while all the turbulent fluctuations are modelled. This approach allows to obtain reliable results saving costs and time for the simulation; for this reason, it is widely used in engineering calculations.

- **Large Eddy Simulation (LES):** this is an intermediate approach for turbulent calculations. The mean flow and the larger eddies are tracked in their motion while the smaller eddies are modelled. It is used a space filtering for the unsteady Navier-Stokes equations: the larger eddies are solved directly while the smaller ones, which are more isotropic, are solved through an averaged model, losing only little information. This approach is more costly and time demanding with respect to RANS simulations, but it is gaining importance in simulations where better turbulence predictions are needed.

- **Direct Numerical Simulations (DNS):** the unsteady Navier-Stokes are computed entirely from the mean flow to the Kolmogorov scale. This requires a mesh with cells smaller than the length scale η of the smallest eddies and a time step shorter than τ, their characteristic time scale. The time requirements and the costs of simulations are very high, that is why this approach is not used for industrial applications.

## 3.3. RANS EQUATIONS AND MODELS

RANS equations are the result of the time averaging of the Navier-Stokes equations. To obtain them it is important to remember the Reynolds decomposition of a generic variable $\varphi$ described by equation (3.2). The mean value $\Phi$ is defined as:

$$\Phi(\boldsymbol{x}) = \frac{1}{\Delta t}\int_0^{\Delta t} \varphi\,(\boldsymbol{x}, t)\,dt \tag{3.5}$$

where $\Delta t$ is a time interval larger than the time scale of the large eddies in mean steady state flows. The large eddies are the ones with the lowest fluctuations (corresponding to longer characteristics times). For non-steady flows $\Phi$ is the ensemble average over a large number of identical repeated experiments.

From the Reynolds decomposition described by (3.2) and from the definition of the mean value $\Phi$ given by (3.5), it follows that:

$$\bar{\varphi}'\,(\boldsymbol{x}, t) = \frac{1}{\Delta t}\int_0^{\Delta t} \varphi'(\boldsymbol{x}, t)\,dt = 0 \tag{3.6}$$

Now, given another generic variable $\psi$, the following relationships can be written:

$$\bar{\varphi}' = \bar{\psi}' = 0 \tag{3.7}$$

$$\overline{\varphi + \psi} = \Phi + \Psi \tag{3.8}$$

Considering the product between $\varphi$ and $\psi$ instead it is obtained:

$$\overline{\varphi \cdot \psi} = \Phi \cdot \Psi + \overline{\varphi' \psi'} \tag{3.9}$$

where:

$$\overline{\varphi' \psi'} = \frac{1}{\Delta t} \int_0^{\Delta t} \varphi' \psi' dt \tag{3.10}$$

this last term defined in the equation (3.10) would be equal to 0 if the fluctuations of $\varphi$ and $\psi$ were independent and random, but in a turbulent system it is not the case and this term assumes a value that needs to be considered.

To obtain the RANS equations the Reynolds decomposition of the scalar and vector fields in the Navier-Stokes equations is done, neglecting the fluctuations of the density $\rho$:

$$\boldsymbol{u} = \boldsymbol{U} + \boldsymbol{u}' \quad and \quad p = P + p' \tag{3.11}$$

at the end of this so-called Reynold averaging, a set of equations is obtained:

Continuity $$\nabla \cdot \boldsymbol{U} = 0 \tag{3.12}$$

x-Momentum $$\frac{\partial U}{\partial t} + \nabla \cdot (U\boldsymbol{U}) + \nabla \cdot (\overline{u'\boldsymbol{u}'}) = -\frac{1}{\rho}\frac{\partial p}{\partial x} + \upsilon \nabla \cdot (\nabla U) + S_u \tag{3.13}$$

y-Momentum $$\frac{\partial V}{\partial t} + \nabla \cdot (V\boldsymbol{U}) + \nabla \cdot (\overline{v'\boldsymbol{u}'}) = -\frac{1}{\rho}\frac{\partial p}{\partial y} + \upsilon \nabla \cdot (\nabla V) + S_v \tag{3.14}$$

z-Momentum $$\frac{\partial W}{\partial t} + \nabla \cdot (W\boldsymbol{U}) + \nabla \cdot (\overline{w'\boldsymbol{u}'}) = -\frac{1}{\rho}\frac{\partial p}{\partial z} + \upsilon \nabla \cdot (\nabla W) + S_w \tag{3.15}$$

Generic scalar $$\frac{\partial \varphi}{\partial t} + \nabla \cdot (\varphi \boldsymbol{U}) + \nabla \cdot (\overline{\varphi'\boldsymbol{u}'}) = \frac{1}{\rho} \nabla \cdot \left(\Gamma_\varphi \nabla \varphi\right) + S_\varphi \tag{3.16}$$

Inside the scalar and momentum equations some new terms appear. They represent the contribution that turbulent eddies have on the mean flow in terms of momentum and energy diffusion. Considering for example one of the momentum equations, these terms can be generally written as:

$$-\nabla \cdot (\overline{u_i' u'}) = \frac{1}{\rho} \sum_{j=1}^{3} \left[ \frac{\partial \left(-\rho \overline{u_i' u_j'}\right)}{\partial x_j} \right] \qquad for\ i = 1, 2, 3 \tag{3.17}$$

Now it is possible to introduce the Reynolds stresses defined as:

$$\tau'_{i,j} = -\rho \overline{u_i' u_j'} \tag{3.18}$$

Boussinesq in 1877 proposed that Reynolds stresses might be expressed using an expression similar to (2.9) for the viscous stresses under the Newtonian fluid assumption:

$$\tau'_{i,j} = \mu_t \left( \frac{\partial U_j}{\partial x_i} + \frac{\partial U_i}{\partial x_j} \right) - \frac{2}{3} \rho k \delta_{i,j} \tag{3.19}$$

where $\mu_t$ is the turbulent viscosity and $k$ is the turbulent kinetic energy per unit mass:

$$k = \frac{1}{2} \left( \overline{u'^2} + \overline{v'^2} + \overline{w'^2} \right) \tag{3.20}$$

Equation (3.19) introduces the so-called Boussinesq approximation that implies the isotropy hypothesis by which there is an equal distribution of turbulent kinetic energy to the three components of the normal Reynolds stresses.
The transport of a generic scalar $\varphi$ due to turbulence can be expressed following a similar assumption:

$$-\rho\overline{u_i'\varphi'} = \Gamma_{t,\varphi}\,\frac{\partial \Phi}{\partial x_i} \tag{3.21}$$

where $\Gamma_{t,\varphi}$ is the turbulent or eddy diffusivity of $\varphi$. According to Reynolds analogy, considering that the transport of momentum and $\varphi$ are due to the same mechanism, it is reasonable to assume that $\Gamma_{t,\varphi}$ is close to $\mu_t$. So, a dimensionless number can be defined as:

$$\sigma_t = \frac{\mu_t}{\Gamma_{t,\varphi}} = constant \tag{3.22}$$

For example, for mass transport $\sigma_t$ corresponds to Schmidt number, while for energy transport it corresponds to Prandtl number. Most of CFD procedures assumes that its value is close to unity.

### 3.3.1. Standard k-ε model

Once the Navier-Stokes equations have been handled to obtain the RANS equations and the Boussinesq approximation has been adopted, it is introduced a new unknown quantity in the set of equations used to describe the fluid system: the turbulent viscosity $\mu_t$. That is why there are introduced models to find a way to express it as function of the other variables of the system.

The $k$ - $\varepsilon$ models family expresses $\mu_t$ as a function of $k$ and $\varepsilon$: $\mu_t = f(k, \varepsilon)$. The turbulent kinetic energy per unit mass $k$ has been already defined in (3.20), while $\varepsilon$ is the rate of dissipation of turbulent kinetic energy per unit mass and it is expressed as:

$$\varepsilon = 2\,\frac{\mu}{\rho}\,\overline{s'_{ij}s'_{ij}} \tag{3.23}$$

The dissipation of turbulent kinetic energy is due to the work done by the smallest eddies against the viscous stresses.

These models are based on the hypothesis that the turbulent viscosity is isotropic, and so that the ratio between the Reynolds stresses and the mean rate of deformation is the same in all directions. This assumption fails in many complex flows. All the $k$ - $\varepsilon$ models require the solution of two additional transport equations (partial differential equations) for $k$ and $\varepsilon$. For this reason, they are called two-equations models.

The standard $k$ - $\varepsilon$ model proposes the following expression to find $\mu_t$:

$$\mu_t = \rho\, C_\mu\,\frac{k^2}{\varepsilon} \tag{3.24}$$

While the transport equations for $k$ and $\varepsilon$ are respectively:

$$\frac{\partial(\rho k)}{\partial t} + div(\rho k \boldsymbol{U}) = div\left[\frac{\mu_t}{\sigma_k}\,grad\,k\right] + 2\mu_t S_{ij}\cdot S_{ij} - \rho\varepsilon \tag{3.25}$$

$$\frac{\partial(\rho\varepsilon)}{\partial t} + div(\rho\varepsilon \boldsymbol{U}) = div\left[\frac{\mu_t}{\sigma_\varepsilon}\, grad\ \varepsilon\right] + C_{1\varepsilon}\frac{\varepsilon}{k}2\mu_t S_{ij}\cdot S_{ij} - C_{2\varepsilon}\rho\frac{\varepsilon^2}{k} \qquad (3.26)$$

These equations are very similar and each term inside them has a specific meaning:

- first term: rate of change of $k$ or $\varepsilon$
- second term: transport of $k$ or $\varepsilon$ by convection
- third term: transport of $k$ or $\varepsilon$ by diffusion
- fourth term: rate of production of $k$ or $\varepsilon$
- fifth term: rate of destruction of $k$ or $\varepsilon$

In equations (3.24), (3.25) and (3.26) five constants are introduced that have been defined by data fitting from experiments:

$$C_\mu = 0.09 \quad \sigma_k = 1.00 \quad \sigma_\varepsilon = 1.30 \quad C_{1\varepsilon} = 1.44 \quad C_{2\varepsilon} = 1.92 \qquad (3.27)$$

but it is also common to use $C_{1\varepsilon} = 1.5$ in jets and sprays simulations.
The standard $k$ - $\varepsilon$ model is well established and it is the most widely validated turbulence model. It provides excellent performances for many industrial cases and up to now it is the best compromise between accuracy and simplicity. However, it fails for some unconfined flows, boundary layers in presence of adverse pressure gradients, rotating and swirling flows.

## 3.4. THE SPRAY STRUCTURE

A detailed description of spray for IC engines applications is presented in [9], [16] and [17]. In this paragraph the most useful information are summarized.

During injection, the liquid fuel is forced through the small injector holes (order of $10^{-1}$ mm) by a large pressure difference (order of $10^2$ MPa) with high speed (order of $10^2$ m/s). The result is that the fuel jet breaks up in small droplets, because of its relatively high velocity, forming a cone-shaped spray. This is the primary breakup and it is illustrated in Figure 3.3.

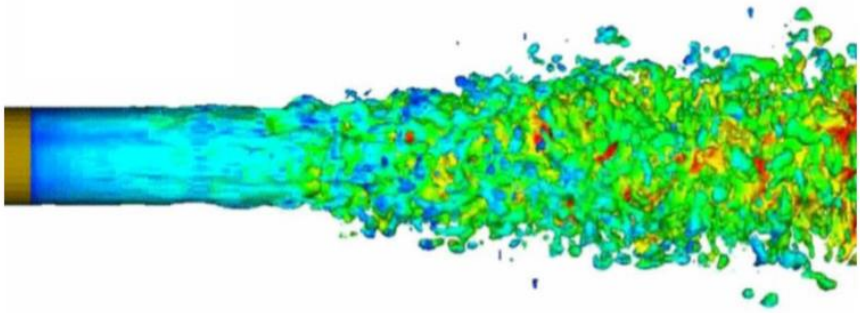

***Figure 3.3 - Primary breakup of the liquid jet***

Primary breakup is followed by a secondary breakup where the already existing droplets are broken and divided into smaller particles by the aerodynamic interactions between the surrounding gas and the droplets themselves. Meanwhile the two different phases of the system (liquid and gas) are exchanging mass and energy.

All this leads to the formation of a spray composed by droplets of different size. Its characteristics are very important to be studied because they determine how the air-fuel mixture is formed and consequently they influence the combustion process. The typical shape of a spray is shown in Figure 3.4 and the main physical characteristics studied are:

- Droplet size (atomization)
- Jet tip advancing (penetration)
- Spray dispersal angle (diffusion)

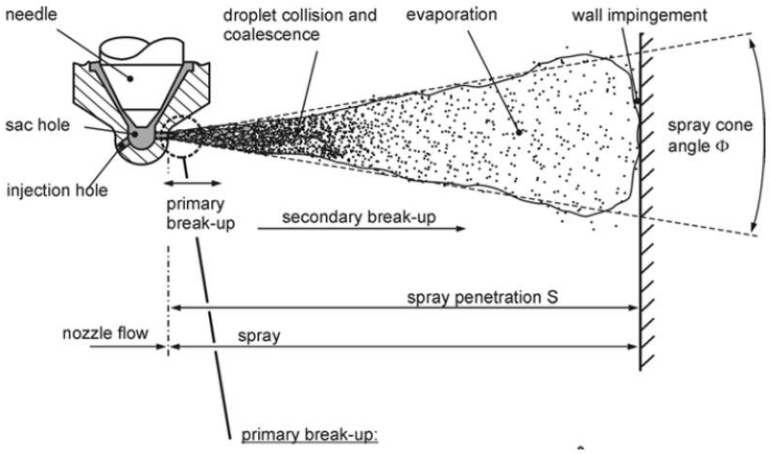


***Figure 3.4 - Representation of a spray formed by the fuel***

### 3.4.1. Atomization

The spray obtained during the injection process contains droplets of different sizes. Since the motion conditions of the liquid and the gas change in space and during time; the breakup mechanisms, that are mainly due to aerodynamic interactions between the two phases, are different. This results in a non-homogeneous atomization process.

To describe synthetically the droplet size and the atomization of the spray, statistical values are used. Usually the droplet diameter is expressed in terms of Sauter mean diameter ($SMD$) that is a proper average value representative of the particle size. Its value can be computed starting from a set of measurements done for the droplet diameter using the following expression:

$$SMD = \frac{\int_{x_m}^{x_M} x^3 \, f(x) \, dx}{\int_{x_m}^{x_M} x^2 \, f(x) \, dx} \tag{3.28}$$

where $x$ represents the general drop diameter, $x_m$ is the minimum diameter measured and $x_M$ is the maximum one. Inside the integrals $f(x)$ is the distribution function and expresses how the droplet diameter is distributed in the set of the measurements done. The $SMD$ is the diameter of a sphere that has the same volume to surface area ratio as the particle considered. The conservation of this ratio has a very important meaning because during evaporation the mass of fuel that changes phase is related to volumes while the heat exchanged is related to surfaces.

The spray atomization is influenced by the injection conditions, for example the $SMD$ will decrease if the injection pressure increases, if the nozzle diameter is reduced or if the density of the gas phase is greater.

### 3.4.2. Penetration

The spray penetration gives information about the distance covered by the fuel from the injection point in the direction of the injector axis. Considering the spray G conditions, the effects of the air motion inside the cylinder (such as swirl, tumble or squish) on the penetration are neglected.

The spray penetration changes during time as the injection process proceeds. The liquid droplets, as they are injected into the system, exchange momentum, energy and mass with the gas phase. What results is the fuel evaporation, the droplet breakup and the change of their velocity. The value of the penetration is influenced by all these processes. The first droplets injected into the system encounter gas that is not moving, so the aerodynamic forces are strong and the liquid drops are broken up and slowed down quickly. While, the fuel that is injected some tenth of millisecond later than the SOI (start of injection) encounters air with a velocity in the same direction of the spray. In this case the aerodynamic forces are lower and the breakup is less intense such as the reduction of the droplet velocity.

The spray penetration depends on numerous parameters. For example, it increases as the injection pressure grows or the droplet diameter is bigger, while it decreases as the gas phase density becomes higher.

During ECN workshops some modelling and computational standards have been defined and regarding the spray penetration it has been made a distinction between liquid and vapor penetration. The penetration length is always measured along the injection axis and the zero is set corresponding to the injection tip, as shown in Figure 3.5.

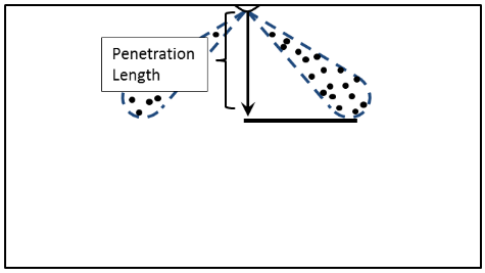


***Figure 3.5 - Measurements of the penetration length***

The liquid penetration is measured using the projected liquid volume methodology suggested by ECN [3]. In the following definitions and explanations, it is used as reference the experimental setup of DBI imaging described in chapter 1. First, it is useful to define the projected liquid volume ($PLV$) as the integral of liquid volume fraction ($LVF$) along a straight path in the y direction:

$$PLV = \int_{-\infty}^{+\infty} LVF\ dy = \int_{-\infty}^{+\infty} \frac{volume\ of\ liquid}{total\ volume}\ dy \tag{3.29}$$

It is possible to state that there is liquid where the local value of *PLV* exceeds a proper threshold value previously defined. Once it is defined where the liquid is present and where it is not, the liquid penetration can be easily measured. ECN suggests to use the following two threshold values for spray G simulations:

$$\int_{-\infty}^{+\infty} LVF\ dy = 0.2 \cdot 10^{-3} \frac{mm^3}{mm^2} \quad and \quad \int_{-\infty}^{+\infty} LVF\ dy = 2.0 \cdot 10^{-3} \frac{mm^3}{mm^2} \tag{3.30}$$

Now it is needed a relation that links the *PLV* to the values obtained with experiments based on light extinction techniques. These techniques measure the attenuation of incident light through an optically thick medium. Considering an experimental setup like the one schematized in Figure 3.6, it is possible to define the optical thickness of a medium as:

$$\tau = -ln\left(\frac{I}{I_0}\right) \tag{3.31}$$

where $I_0$ is the intensity of the incident radiation and I is the intensity of the outgoing radiation.


***Figure 3.6 - Light extinction across an optically thick medium***

Exploiting the so-called Mie-scattering relations, it is possible to relate this value of $\tau$ to the projected liquid volume fraction:

$$\tau \frac{\pi\ D^3}{6\ C_{ext}^*} = \int_{-\infty}^{+\infty} \text{LVF dy} \tag{3.32}$$

where $D$ is the droplet diameter and $C_{ext}^*$ is a constant that accounts for a finite collection angle. They are two constants and their value depend on the experimental setup. Always referring to ECN recommendations a droplet size of 7 μm is a reasonable value for spray G.

The vapor penetration, instead, is defined on the base of the mixture fractions. Again, it is imposed a threshold value of 0.1% for the fuel fraction and it is possible to state that there is fuel where the mixture fraction is greater than the threshold value.

### 3.4.3. Diffusion

The liquid droplet created by the breakup process tends to move away one from each other once they leave the injector. The resulting spray has a cone shape and its opening angle $\beta_{sp}$ mainly depends on:

- The ratio between the density of the gas phase $\rho_g$ and the density of the liquid $\rho_l$. As this ratio increases, they increase also the aerodynamic forces among the two phases and the cone angle becomes greater.
- The geometric ratio between the length of the injection channel $L_f$ and the injection hole diameter $d_f$. As this ratio increases, the dispersal angle decreases because the fuel flow is more forced to follow a certain path inside the injection nozzle and when the fuel leaves it has less tendency to create a widely opened spray.

Moreover, during the opening of the injection nozzle, the cross-section area, where the flow passes, results smaller since the needle opening is not instantaneous. In that moment the mass of fuel injected is lower and it is strongly influenced by the aerodynamic interaction with the gas. In this phase the cone angle results bigger. Later, when the needle is fully opened, and the gas starts to move following the spray direction and $\beta_{sp}$ diminishes. This trend is shown in Figure 3.7:

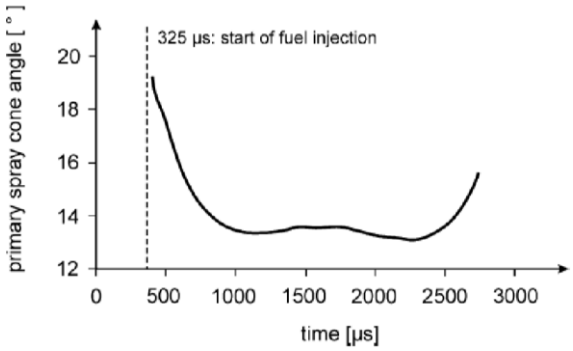


***Figure 3.7 - Spray cone angle as function of time***

There exist several correlations to compute the value of $\beta_{sp}$ as function of the main parameters that influence it. The most widely used is the Reitz-Bracco:

$$tan\left(\frac{\beta_{sp}}{2}\right) = \frac{4\pi}{A}\sqrt{\frac{\rho_g}{\rho_l}}\frac{\sqrt{3}}{6} \tag{3.33}$$

where:

$$A = 3 + \frac{1}{3.6}\left(\frac{L_f}{d_f}\right) \tag{3.34}$$

## 3.5. PRIMARY BREAKUP

Considering the motion condition of the liquid inside the injector under typical working condition, the fuel immediately breaks up into droplets once it leaves the nozzle hole, producing the so-called primary breakup. This is caused by some instabilities already present in the fluid flow inside the injector where the motion is turbulent, due to the high velocities reached. The turbulent flow creates some small vortexes that can be strong enough to win the surface tension producing droplets and branches that detach from the mean flow. Another effect must be accounted: inside the nozzle channels the fluid high velocities allow to create cavitation bubbles where the pressure locally becomes smaller than the bubble point pressure. At the nozzle outlet, where the pressure increase, these bubbles implode increasing the instabilities in the flow.

Once the fuel leaves the nozzle, the instabilities created by cavitation bubbles and turbulent vortexes are increased by the aerodynamic interaction between liquid and gas. According to Reitz and Bracco [18] the primary breakup can follow different mechanisms depending on the physical properties of the two phases and the relative velocities. To understand and distinguish the different breakup modes, it is useful to introduce some dimensionless numbers: the Reynolds number, the Weber number for the liquid phase and the Ohnesorge number. They are respectively defined as:

$$Re = \frac{\rho_l \, u \, D}{\mu_l} \tag{3.35}$$

$$We_l = \frac{\rho_l \, u^2 \, D}{\sigma_l} \tag{3.36}$$

$$Z = \frac{\sqrt{We_l}}{Re} \tag{3.37}$$

Four different breakup mechanisms can be identified depending on these dimensionless quantities: Rayleigh, first wind induced, second wind induced and atomization. They are represented in the Ohnesorge 2D diagram as function of $Z$ and $Re$; while Reitz proposed an extension accounting also the dependence on the ratio $\rho_g/\rho_l$ creating a 3D diagram (Figure 3.8).

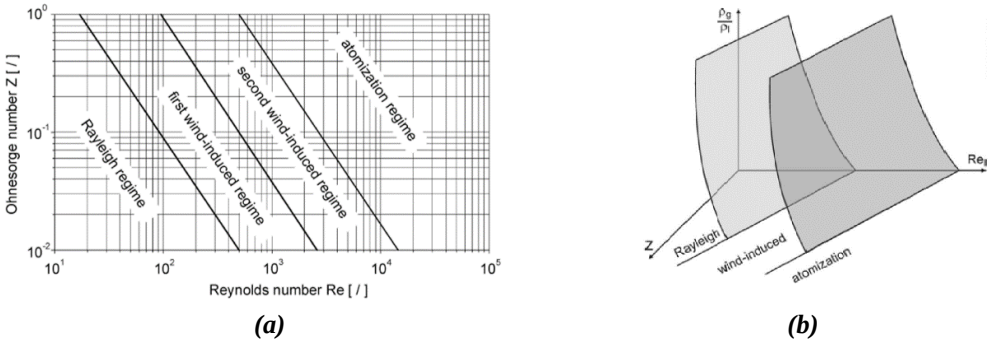


*(a)* *(b)*

***Figure 3.8 – Ohnesorge diagram (a) and the Reitz extension (b)***

Considering the typical working conditions present in spray G, where there are high velocities and great $Re$, the most important mechanism is the atomization. The separation of droplets from the liquid jet starts immediately after the injector outlet and the so-called intact surface length tends to zero. While the central part of the jet remains untouched for a certain length, called liquid core length, after which the spray becomes composed only by liquid droplets and the central fluid vein completely disappear.

The complete description of primary breakup is very complex since it is influenced by the fluid motion inside the nozzle channels. The small characteristic dimensions and the high velocities make the experimental measurements very complex, therefore, it is preferred to implement models able to describe the conditions of the liquid drops at the injector outlet without solving the fluid flow inside the nozzle. These models provide the initial condition of the droplets, such as diameter, velocity and spray cone angle, once they leave the nozzle by means of adjustable constants that allows to include the effects of the in-nozzle phenomena.

### 3.5.1. Blob Injection Model

Reitz and Diwakar [19] proposed a very simple model to describe the initial conditions of the liquid drops at the nozzle outlet. Instead of simulating the whole atomization process it collects the real existing liquid droplets in packages, called parcels, and it provides their initial conditions.

The diameter of all the parcels injected is assumed to be equal to the nozzle diameter $d_f$, while the number of the droplets created in a time interval is computed using the injection law, that express the injection rate (mass flow rate) as function of time:

$$n = \frac{\dot{m}_{inj}(t)}{\Delta t \, m_{parcel}} \tag{3.38}$$

where $\dot{m}_{inj}(t)$ is the injection rate that can be measured experimentally, $\Delta t$ is the time interval and $m_{parcel}$ is the mass of a single parcel that can be computed using the liquid density $\rho_l$ and considering the parcel as a sphere with a diameter $d_f$. Also the initial velocity of the parcel can be computed from the injection law:

$$U_{inj}(t) = \frac{\dot{m}_{inj}(t)}{\rho_l \, A_{eff}} \tag{3.39}$$

where $A_{eff}$ is the effective cross-section area that is computed as:

$$A_{eff} = \frac{\pi \, d_f^2}{4} \, C_d \tag{3.40}$$

$C_d$ is the area contraction coefficient and accounts for the fact that not all the actual geometrical area of the hole is exploited by the fuel flow, but only a fraction of it, the so-called effective area.

The velocity direction is computed exploiting the knowledge of the cone angle $\beta_{sp}$ using correlations like (3.33). The components of the velocity vector are usually expressed in terms of polar angle $\psi$ and azimuthal angle $\varphi$ defined with respect to the injector axis as shown in Figure 3.9 . They are computed with:

$$\psi = \frac{\beta_{sp}}{2}\,\xi_1 \tag{3.41}$$

$$\varphi = 2\pi\,\xi_2 \tag{3.42}$$

where $\xi_1$ and $\xi_2$ are random numbers that belong to the interval [0;1]. They are created using statistical tools that allows to obtain the correct distribution of particles inside the cone angle.
This model is very simple to implement but all the information regarding the turbulent motion at the injector outlet and the cavitation are lost. If they need to be considered, more complex and accurate models must be used.

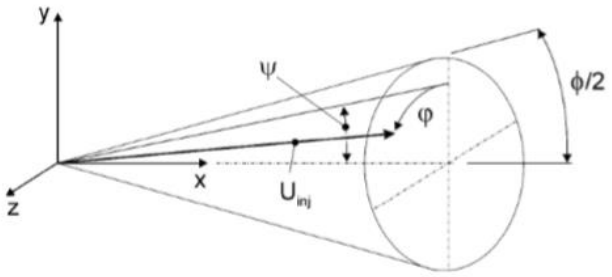


***Figure 3.9 - Representation of polar and azimuthal angles***

### 3.5.2. Huh-Gosman model

Huh and Gosman [8] proposed a model of turbulence-induced atomization for full-cone diesel sprays. This model is able also to predict the primary spray cone angle. It is assumed that the turbulent motion within the liquid at the nozzle outlet produces an initial surface perturbation. This perturbation grows exponentially due to aerodynamic forces, until there is the formation of new droplets. The wavelengths of the most unstable surface disturbances are determined by the turbulent length scale, while the turbulent kinetic energy is estimated from material, energy and momentum balances.

According to this model, the fuel is injected into the system as spherical blobs with the same diameter of the nozzle hole $d_f$, like it is done in the Blob injection model. On the surface of these blobs, perturbations grow due to the action done by aerodynamic forces, with a mechanism similar to the one described in Kelvin-Helmoltz model for secondary breakup. Their characteristic atomization length scale $L_A$ and time scale $\tau_A$ can be obtained by some equations. The atomization length scale is assumed to be dependant to the turbulence length scale $L_t$ according to this relation:

$$L_A = C_1 L_t = C_2 L_w \tag{3.43}$$

where the constants are set equal to $C_1$ = 2.0; $C_2$ = 0.5 and $L_w$ is the wavelength of surface perturbations caused by turbulence.
The characteristic atomization time scale is expressed as a linear combination of turbulent time scale $\tau_t$ and the spontaneous wave growth time scale $\tau_w$:

$$\tau_A = C_3 \tau_t + C_4 \tau_w \tag{3.44}$$

where $C_3$= 1.2 and $C_4$ = 0.5. The wave grow-rate time-scale $\tau_w$ is given by:

$$\tau_w = \left[ \frac{\rho_l \rho_g}{(\rho_l + \rho_g)^2} \left( \frac{U_{inj}}{L_w} \right)^2 - \frac{\sigma}{(\rho_l + \rho_g) {L_w}^3} \right]^{-1} \tag{3.45}$$

This formula is provided by KH instability theory and it is valid for an inviscid liquid. The turbulent length scale $L_t$ and time scale $\tau_t$ are evaluated using the turbulent kinetic energy $k$ and its rate of dissipation $\varepsilon$:

$$L_t = C_\mu \frac{k^{1.5}}{\varepsilon} \tag{3.46}$$

$$\tau_t = C_\mu \frac{k}{\varepsilon} \tag{3.47}$$

where $C_\mu$ is the same constant that appears in the $k$ - $\varepsilon$ model for turbulence.
The Huh-Gosman model predicts also the primary spray cone angle $\varphi$. To do this, the values of atomization length scale and time scale are evaluated for the blobs that are injected into the system to obtain respectively $L_{A,0}$ and $\tau_{A,0}$. It is also assumed that the spray diverges with a radial velocity equal to $L_{A,0}/\tau_{A,0}$.

$$tan\left(\frac{\varphi}{2}\right) = \frac{L_{A,0}/\tau_{A,0}}{U_{inj}} \tag{3.48}$$

Finally it is possible to compute the breakup rate and the size of the new secondary droplets starting from equations (3.43) and (3.44). The breakup rate of the primary blob is proportional to the ratio between atomization length and time scales:

$$\frac{d(D_p(t))}{dt} = C_5 \frac{L_A(t)}{\tau_A(t)} \tag{3.49}$$

$C_5$ is an adjustable constant. $L_A$ and $\tau_A$ are time dependent since the turbulence inside the blob is reduced during time when it leaves the nozzle hole. There are some correlations to evaluate $L_t$ and $\tau_t$ starting from the initial values computed for the blob $L_{t,0}$ and $\tau_{t,0}$:

$$L_t(t) = L_{t,0} \left( 1.0 + \frac{0.0828\, t}{\tau_{t,0}} \right)^{0.457} \tag{3.50}$$

$$\tau_t(t) = \tau_{t,0} + 0828\, t \tag{3.51}$$

$L_A$ and $\tau_A$ are evaluated using again equations (3.43) and (3.44) with the new updated values obtained for $L_t$ and $\tau_t$.
The parcels are classified in two categories: the primary parcels (parents) are the ones injected from the nozzle, the secondary parcels (child) are the ones generated from the primary parcels. Child droplets continuously detach from the parents, decreasing their dimensions, through a process called stripping.
Similarly to the primary parcels also the secondary ones can be broken with a breakup rate given by:

$$\frac{d(D_S)}{dt} = k_2 \frac{L_w}{\tau_w} \tag{3.52}$$

$k_2$ is another adjustable constant. In this case the surface perturbations are the main phenomena that influence the breakup, while the turbulence inside the nozzle has not a

direct influence on it. For this reason, equation (3.52) is similar to (3.49), but the atomization quantities (that accounts for both perturbations and turbulence in the nozzle) are substituted with perturbations quantities.
The diameter of the secondary droplets is computed through probability functions defined as:

$$p(x) = C\frac{\Phi(x)}{\tau_A(x)} \tag{3.53}$$

where $x$ represents the droplet diameter, $\Phi(x)$ is the turbulent energy spectrum and $C$ is a constant determined by imposing:

$$\int_0^\infty p(x) = 1 \tag{3.54}$$

The velocity of the secondary particle is given as the vector sum of the velocity of the parent drop plus a normal velocity component computed using characteristic length and time scales relative to the child drop:

$$V_{normal} = \frac{L_s}{\tau_s} \tag{3.55}$$

$L_s$ is the $SMD$ of the secondary parcel determined using $p(x)$ and $\tau_s$ is evaluated using:

$$\tau_S = C_3\tau_t\left(\frac{L_s}{C_1}\right) + C_4\tau_w\left(\frac{L_s}{C_2}\right) \tag{3.56}$$

Huh-Gosman model is more advanced than Blob injection model because it accounts the influence of turbulence at nozzle exit on the primary breakup. Its performances are reasonably good, especially in steady state single hole cases. However, it neglects the effects of cavitation; so, its use must be limited to non-cavitating turbulent nozzle hole flows.

## 3.6. SECONDARY BREAKUP

The secondary breakup happens when the liquid droplets are divided into smaller particles by the action of the aerodynamic interaction with the surrounding gas. These forces are present because the two phases in contact are moving with different velocities. As consequence of this, some instabilities are created on the interface surface that continuously change, modifying also the drops shape. The distorting effect of the aerodynamic forces is opposed by the surface tension of the liquid that acts to maintain the initial spherical shape.

The dimensionless Weber number is used to describe the relative weight of these forces with opposite effects:

$$We = \frac{\rho_g\, u_{rel}^2\, D}{\sigma_l} = \frac{aerodynamic\ force}{surface\ tension} \tag{3.57}$$

At different values of $We$ correspond different regimes of breakup, as shown in Figure 3.10:

- For $We$ around 6 the vibrational breakup occurs when the oscillatory motion prevails.

- For $We$ < 10 the bag breakup occurs. In this case the droplet is deformed and assumes the shape of an empty bag before it is broken up.
- For $We$ < 25 the bag / streamer breakup happens. This situation is very similar to the previous one with an additional formation of a streamer shaped interior inside the bag.
- For 25 < $We$ < 50 it is possible to find the stripping breakup. The aerodynamic forces are intense and small droplets are stripped or sheared off the surface of the bigger parent drop.
- For $We$ > 50 occurs the catastrophic breakup and a lot of small particles are created from the parent.

The values that identify the ranges of each breakup mode are only indicative and they are obtained experimentally.

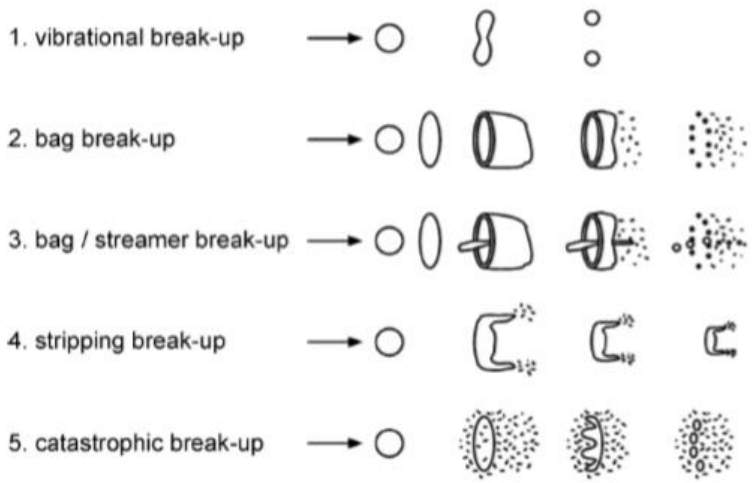


***Figure 3.10 - Different drops breakup regimes***

In engine spray simulations all the breakup regimes presented above are present. For example, near the nozzle outlet the catastrophic breakup occurs due to high velocities and big diameters, while where the droplet dimensions are lower, due to evaporation and previous breakup, it is possible to find all the other regimes.

### 3.6.1. Kelvin-Helmoltz Model

The Kelvin-Helmoltz model, described by Reitz in [20], assumes that each liquid droplet has a series of waves and instabilities on its surface once it leaves the nozzle hole. Their presence is the consequence of the turbulent vortexes and cavitation bubbles that are present inside the nozzle channels. These waves and instabilities grow up because of the aerodynamic interaction between the gas and liquid phases that have different velocities. Their growth goes on until some new smaller drops are created and they detach from the surface.

From the Navier-Stokes equation written for both the two phases it is possible to obtain a relation that express the rate of growth of a certain wave $\omega$ with its proper

characteristic length $\lambda$. To do this it is necessary to assume that fluids are incompressible and that the viscosity of the gas phase is equal to 0 (inviscid fluid). The expression obtained can be solved numerically and the results show that there is only one maximum value for $\omega$, named $\Omega$, that is obtained when $\lambda = \Lambda$. Kelvin-Helmoltz models assumes also that only this wave which has the maximum grow rate will detach creating news drops. The radius of the newly born droplets is provided by:

$$r_c = B_0 \, \Lambda \tag{3.58}$$

Where $B_0$ is a constant usually equal to 0.61. The child drop detaches from the parent drop that continuously loses mass as the breakup occurs. This results in a shrinking radius and it rate of reduction can be expressed as

$$\frac{dr}{dt} = -\frac{r - r_c}{\tau_{BU}}, \quad with \;\; \tau_{BU} = 3.778 \, B_1 \frac{r}{\Omega \Lambda} \tag{3.59}$$

$B_1$ is an adjustable constant that usually assumes values from 1.73 to 60. It accounts the influence of turbulence level and nozzle design on spray breakup.

The KH breakup model results in a bimodal droplet size distribution with small droplets that are sheared off the surface of the parent droplets and larger droplets remaining from the original parent drop.

### 3.6.2. Rayleigh-Taylor Model

The Rayleigh-Taylor model [21] is based on the analysis about the instability of the interface between two fluid with different density once it undergoes an acceleration. As it is assumed in the KH model, the interface surface of the liquid droplets presents a series of waves and instabilities caused by the motion conditions inside the nozzle. When there is an acceleration directed from the less dense fluid to the denser one, it results a stabilization of the surface; while, when the acceleration is directed in the opposite direction, the instabilities grow. For a fuel droplet that is moving inside a gas, the front surface results stabilized while the back-side surface present instabilities that are growing. This is clearly shown in Figure 3.11.

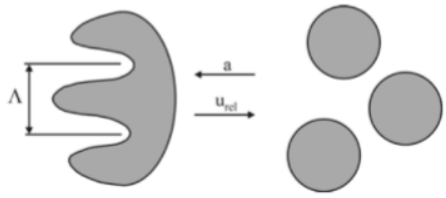


***Figure 3.11 - Deformation of liquid drop according to RT model***

The aerodynamic force that is applied on the surface of the drop, due to different velocities between liquid and gas, can be expressed as:

$$F_{aero} = \pi\, D^2 C_d \frac{\rho_g\, u_{rel}^2}{8} \tag{3.60}$$

while the consequent acceleration is:

$$a = \frac{F_{aero}}{m_d} = \frac{3}{8} C_d \frac{\rho_g\, u_{rel}^2}{\rho_l\, r} \tag{3.61}$$

Similarly to KH model, the waves grow up and only one of them, the one which has the highest grow rate, detaches from the surface determining the breakup of the original droplet. The RT model provides also the equation to compute the characteristic length and the grow rate, $\Lambda$ and $\Omega$, for the waves that will generate the breakup:

$$\Lambda = C_{RT}\, 2\pi \sqrt{\frac{3\sigma}{a\,(\rho_l - \rho_g)}} \tag{3.62}$$

$$\Omega = \sqrt{\frac{2}{3\sqrt{3\sigma}} \frac{\left[a(\rho_l - \rho_g)\right]^{1.5}}{(\rho_l + \rho_g)}} \tag{3.63}$$

$C_{RT}$ is a constant that accounts for all the effects, which are unpredictable a priori, that can create instabilities over the surface, like turbulent eddies inside the nozzle or the implosion of cavitation bubbles. Since this strongly affects the properties of the drops generated, it must be accurately calibrated.

It is possible to show that the characteristic breakup time $\tau_{RT}$ is simply $1/\Omega$. So, the droplet breaks up once it has passed a period of time equal to $\tau_{RT}$ and the parcels created have a diameter $d_c = \Lambda$. Obviously, to avoid unphysical situations, $\Lambda$ must be smaller than the diameter of the original parent droplet.

The RT breakup model predicts the disintegration of a parent droplet into a number of equally sized droplets. The resulting spray droplets are too small, especially near the nozzle outlet where the great values reached by the relative velocity determines a very strong acceleration $a$. For this reason, it is not commonly used in CFD simulations as it is, but it is frequently combined with the KH model.

### 3.6.3. KHRT model

Generally, a single model implemented alone is not able to completely describe all the breakup mechanisms; that is why they are combined to create new and more complete models. The KHRT model derives from the combination of the KH and the RT models and it is widely used in CFD simulations since it provides good predictions of the secondary breakup and, in particular, of the catastrophic breakup.

Hwang et al. in their work [7] observed that the aerodynamic forces act on the droplets crushing them and creating disk shaped particles. After that, they are broken following the mechanism proposed by the RT model. At the same time, the small waves, present on the surface, lead to the formation of micro droplets that detach from the surface following the stripping mechanism proposed by the KH model.

To avoid the excessive breakup given by the RT model near the nozzle outlet, it is imposed that within a certain distance from the injector, called core length, only the KH breakup can occur. Farther, both breakup mechanisms are present. The core length is computed using the following expression:

$$L_c = C_{BU}\, d_f \sqrt{\frac{\rho_l}{\rho_g}} \tag{3.64}$$

where $C_{BU}$ is a constant that accounts for the motion condition inside the injector.

The combination of KH and RT models counteracts the formation of sprays with a distinct bimodal droplet size distribution.

### 3.6.4. Pilch Erdman model

Pilch and Erdman [6] proposed a model by which breakup takes place only if the droplet diameter $D_d$ is greater than a limit value $D_S$, that represents the maximum stable diameter. The value assumed by $D_S$ is affected by:

- the decrease of the droplet Weber number because of the new smaller droplet diameter.
- the decrease of the relative velocity $u_{rel}$ between the liquid droplets and the surrounding gas as result of the forces acting on the droplet and the exchange of momentum.

The breakup occurs if the decrease in Weber number is greater than a critical value computed using the following correlation:

$$We_c = 6\,(1 + 1.077\, Z^{1.6}) \tag{3.65}$$

where $Z$ is the Ohnesorge number that accounts for the viscous effect.

Pilch and Erdman distinguished among five different breakup mechanisms that can occur at different Weber numbers; similar to what was described in Figure 3.10. At each regime is associated an expression to compute the dimensionless total breakup time $\bar{\tau}_b$ as it is possible to see in Table 3-1.

| Breakup Regime | $\bar{\tau}_b$ | Weber number |
|---|---|---|
| Vibrational BU | $6\,(2\,We - 12)^{-0.25}$ | $0 < We \leq 9$ |
| Bag BU | $2.45\,(2\,We - 12)^{0.25}$ | $9 < We \leq 22$ |
| Bag-and-stamen BU | $14.1\,(2\,We - 12)^{-0.25}$ | $22 < We \leq 175$ |
| Sheet stripping | $0.766\,(2\,We - 12)^{0.25}$ | $175 < We \leq 1335$ |
| Wave crest stripping | $5.5$ | $We > 1335$ |

***Table 3-1 - Breakup regimes and their corresponding dimensionless breakup times and We ranges according to Pilch-Erman model***

The dimensionless total breakup time $\bar{\tau}_b$ is defined starting from the total breakup time $\tau_b$ and applying the following definition:

$$\bar{\tau}_b = \tau_b \frac{u_{rel}}{D_d} \left(\frac{\rho_g}{\rho_l}\right)^{1/2} \tag{3.66}$$

Once these values are known, it is possible to evaluate the maximum stable diameter:

$$D_s = 2\, We_c \frac{\sigma_l}{\rho_g\, {u_{rel}}^2 \left(1 - \frac{V_d}{u_{rel}}\right)^{-2}} \tag{3.67}$$

where $V_d$ is the droplet volume defined by:

$$V_d = u_{rel} \left(\frac{\rho_g}{\rho_l}\right)^{1/2} (B_1 \bar{\tau}_b + B_2 {\bar{\tau}_b}^2) \tag{3.68}$$

$B_1$ and $B_2$ are constants that need to be calibrated to fit experimental data. Finally, the change in diameter of the liquid droplets can be computed as:

$$\frac{dD_d}{dt} = \frac{D_d - D_s}{\tau_b} \tag{3.69}$$

The breakup mechanism described by this model is very similar to the one described by the KH model where the child drops were stripped of the parent drop. In PE model only the reduction in diameter of the parent drop is accounted and no child drops are created. The correlations adopted to describe the maximum stable diameter and the breakup time are based on experimental measurements. That is why this model provides good results when the constants are properly calibrated.

PE model is not so common in CFD simulations of Lagrangian sprays since the KHRT model performs better in a wide range of practical cases and it is largely used in most of the situations.

### 3.6.5. KHRTPE model

KHRTPE model is another hybrid model obtained by combining the KHRT model and the Pilch-Erdman model. The advantages of the combination of different models have been already described while treating the KHRT model. In this case, at the KHRT model, it is added the possibility to have the Pilch-Erdman breakup inside the core length described by (3.64).

The KH breakup mechanism can be applied only once for each injected parcel which has not undergone any breakup. The PE breakup is applied only inside the core length, while the RT mechanism can be applied only after the core length to avoid excessive breakup.

This hybrid model has been developed only recently by the Internal Combustion Engines (ICE) group of Politecnico di Milano and it has not been validated yet.

# 4. FINITE VOLUME METHOD

As discussed in chapter 2 the fluid dynamic problem requires the solution of a system of non-linear partial differential equation coupled together. This system cannot be solved analytically obtaining an exact solution, except for few simple cases. However, by applying the finite volume method it is possible to obtain an approximate solution that can be useful in practical applications. The approximation is related to the fact that the domain is discretized into elements which have finite dimensions and that are not infinitesimal. The theoretical description of the finite volume method gives the tools necessary to understand the quality of the approximation and of the results obtained.

The finite volume method can be schematized in three steps. As first there is the grid generation step, where the domain is divided into discrete control volumes. After that, the governing equations are integrated over a control volume to obtain algebraic equations in the so-called discretization step. Finally, during the last step, the equations are solved with an approximated method.

## 4.1. DISCRETIZATION OF SPACE AND TIME

### 4.1.1. Space Discretization: Mesh ad Quality

The mesh is the result of the geometrical discretization of the control volume. It is composed by cells that are the fixed control volumes where the conservation equations are integrated. For 3D domains, the elements of the mesh can have the shape of a tetrahedron, a pyramid, a prism, a hexahedron or a polyhedron. The accuracy of the solution depends a lot on the quality of the grid used; a poor-quality grid causes inaccurate solutions and slows down the convergence. That is why it is important to define the quality and then check if the mesh used satisfies certain criteria. The following definitions are given according to the user guide of OpenFOAM [22] that was used during this work:

- Aspect Ratio: it is the ratio between the longest and the shortest length in a cell. Considering a 3D element, it is possible to identify its bounding box, that is the minimal box that can contain the cell. Being $a_x$, $a_y$ and $a_z$ the areas of the bounding box faces, the aspect ratio is equal to the largest value among $Eq1$ and $Eq2$:

$$Eq1 = \frac{max(a_x, a_y, a_z)}{min(a_x, a_y, a_z)} \tag{4.1}$$

$$Eq2 = \frac{1}{6}\,\frac{|a_x| + |a_y| + |a_z|}{V^{2/3}} \tag{4.2}$$

$V$ represents the volume of the cell considered. The best aspect ratio obtainable is 1, corresponding to a cell that has the same lengths in all the directions. The aspect ratio gives information about how much an element of the mesh is stretched in a

direction rather than the others. Cells that are strongly stretched in a certain direction are unwanted because the fluxes that are perpendicular to it are underestimated compared to those fluxes that are parallel. This is not such a big issue in those cases where the flow direction is aligned with the cell stretching direction and where those fluxes that are perpendicular can be neglected. However, when the aspect ratio becomes strongly greater than 1, attention must be paid.

- Mesh non-orthogonality: it is the measure of the angle between the line connecting two cell centres and the normal of their common face. Referring to Figure 4.1 it is the angle between the red arrows and the corresponding blue ones. A value of 0 is the best obtainable for mesh non-orthogonality, while values greater than 70 degrees are considered unwanted (this threshold is suggested by the OpenFOAM user guide).
- Skewness: it is the measure of the distance between the intersection of the line connecting two cell centres with their common face and the centre of that face. The smaller is the skewness, the better is the quality of the mesh. The minim value obtainable is 0.

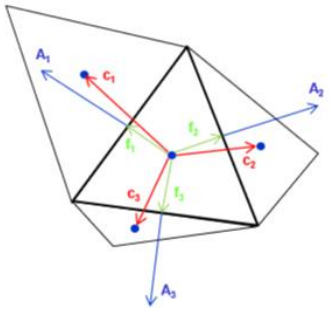


***Figure 4.1 - Representation of the angle between the line connecting two cell centres and their common face normal***

### 4.1.2. Time Discretization: Courant Number

When a time dependant problem is considered not only the space is discretized, but also the time. Usually a proper time step $\Delta t$ is chosen, then the simulation is performed starting from the initial time and advancing step by step until the end time. The choice of the time step size is done considering the dimensionless Courant number defined as:

$$Co = \frac{u\,\Delta t}{\Delta x} \approx \frac{|\boldsymbol{u}|\,\Delta t}{V^{1/3}} \tag{4.3}$$

where u is a characteristic velocity and $\Delta x$ is a characteristic length both related to the mesh element where the Courant number is computed. To simplify the calculations as characteristic velocity it can be considered the magnitude of the velocity inside the cell and as characteristic length it can be used the cube root of the cell volume.
By keeping the maximum Courant number close to 0.1, a high temporal accuracy and a very good convergence rate are ensured. For Courant maximum values close to 1, good temporal accuracy and convergence are still ensured; while, if it is greater than 10 there can be convergence issues. It is important to notice that the choice of the time step is

closely connected to the cells size inside the mesh. Only once the mesh is created the time step can be decided. Obviously finer is the mesh and smaller must be $\Delta t$, implying an increase of the computational time necessary for the simulation.

## 4.2. INTEGRATION OF THE CONSERVATION EQUATIONS

For the Eulerian phase of the system the conservation equations are integrated over each cell of the mesh. The following description uses [14] as main source. Considering the generic quantity $\varphi$ (scalar or vector), its conservation equation in unsteady conditions can be written as:

$$\frac{\partial(\rho\varphi)}{\partial t} + \nabla \cdot (\rho\varphi \boldsymbol{u}) = \nabla \cdot (\Gamma_\varphi \nabla\varphi) + S_\varphi \tag{4.4}$$

written in words it becomes:

$$\begin{bmatrix} Rate\ of\ change \\ of\ \varphi\ in\ the \\ control\ volume \\ with\ respect\ to \\ time \end{bmatrix} + \begin{bmatrix} Transport \\ of\ \varphi \\ by\ convection \end{bmatrix} = \begin{bmatrix} Transport \\ of\ \varphi \\ by\ diffusion \end{bmatrix} + \begin{bmatrix} source \\ term \end{bmatrix}$$

Integrating (4.4) on a fixed control volume $V$ and a finite time step $\Delta t$ it is obtained:

$$\int_V \int_t^{t+\Delta t} \frac{\partial(\rho\varphi)}{\partial t} + \int_V \int_t^{t+\Delta t} \nabla \cdot (\rho\varphi \boldsymbol{u}) = \int_V \int_t^{t+\Delta t} \nabla \cdot (\Gamma_\varphi \nabla\varphi) + \int_V \int_t^{t+\Delta t} S_\varphi \tag{4.5}$$

applying the Gauss-Green theorem and being $\partial V$ the boundary of the control volume:

$$\begin{aligned} \int_t^{t+\Delta t} \int_V \frac{\partial(\rho\varphi)}{\partial t} dV\, dt + \int_t^{t+\Delta t} \int_{\partial V} (\rho\varphi \boldsymbol{u}) \cdot n\, dA\, dt \\ = \int_t^{t+\Delta t} \int_{\partial V} (\Gamma_\varphi \nabla\varphi) \cdot n\, dA\, dt + \int_t^{t+\Delta t} \int_{\partial V} S_\varphi\, dV dt \end{aligned} \tag{4.6}$$

The computational domain is decomposed using a mesh with a certain number of finite volumes. Each one of them is characterized by a central node and one face node for each face. Usually it is used a convention by which central nodes are define with capital letters and face nodes are defined with small letters (Figure 4.2).

At the end of the discretization process, a system of algebraic equations is obtained. These equations can be managed and expressed in the following general form:

$$a_P \varphi_P = \sum a_{nb} \varphi_{nb} + S_u \tag{4.7}$$

where the left-hand side contains the quantity $\varphi$ evaluated in the centre cell $P$ with the corresponding coefficient $a_P$. On the right-hand side $S_u$ collects all the source terms and the summation sign contains the contribution given by all the neighbour cells, again expressed as the product between a coefficient and the quantity $\varphi$ evaluated on the node of the neighbour cell.

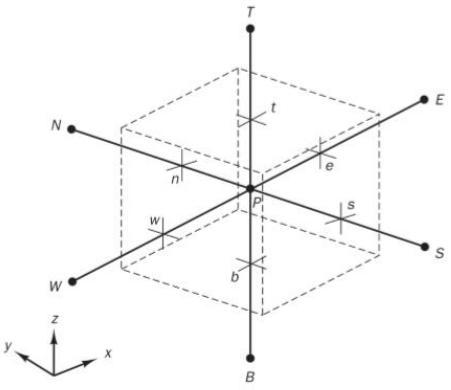


***Figure 4.2 - Representation of the convention used for the point's nomenclature***

When a discretization scheme is used, it is important to satisfy certain fundamental properties to be consistent with the initial physical problem. These properties are:

- Conservativeness: this is the property that ensures the consistency of the schemes. It is verified when the flux of $\varphi$ that leaves a cell across a certain face is the same that enters the adjacent control volume through the same face.
- Boundedness: it is linked to the convergence of the scheme. Since the finite volume method expects to find a solution starting from a guessed value of $\varphi$ and performing a series of iterations, it is needed a criterion that ensures the convergence. Scarborough (1958) showed that a sufficient condition for a convergent iterative method ca be expressed as:

$$\frac{\sum|a_{nb}|}{|a'_P|} \begin{cases} \leq 1 \; at \; all \; nodes \\ < 1 \; at \; one \; node \; at \; least \end{cases} \tag{4.8}$$

  where $a'_P$ is the net coefficient of the central node P obtained as $a_P - S_u$. If this condition is satisfied the matrix correspondent to the algebraic system is diagonally dominant and convergence can be reached.
- Transportiveness: when a quantity $\varphi$ is evaluated on a face of the grid, its value is influenced in different ways by the values that $\varphi$ assumes in the nodes of those cells that share the face considered. This property accounts for the effects of the flow, in terms of both magnitude and direction, to assign different weights to the node values of the quantity while this evaluation is done. The dimensionless Peclet number is used to measure the relative strengths of convection and diffusion:

$$Pe = \frac{F}{D} = \frac{\rho \, u}{\Gamma_\varphi / \delta x} \tag{4.9}$$

  where $\delta x$ is the cell characteristic length that is representative of the width of the cell. $F$ and $D$ are presented and defined after during the detailed discussion of the diffusion and convective terms. As $Pe$ of a cell increases, the nodes downstream are more influenced by it. Transportiveness relates the directionality of the influence on a quantity at the flow direction and magnitude.

To obtain the form described by (4.7) starting from the equation (4.6), it is required to evaluate each term present in (4.6) as follows. For sake of simplicity the expressions presented here are obtained using a uniform grid, where the node of a face is exactly the midpoint of the line that connects the two central nodes. However, this discussion can be easily extended to non-uniform grids:

- **Diffusion term**: it contains a gradient that needs to be approximated by a differencing scheme. The order used for this simplification must be chosen as a compromise between the desired accuracy and the computational cost. For example, the central differencing scheme is second-order accurate and it estimates the first derivative of the face node as:

$$\left(\frac{\partial \varphi}{\partial x}\right)_i = \frac{\varphi_I - \varphi_P}{\Delta x_{PI}} + O(\Delta {x_{PI}}^2) \tag{4.10}$$

The last term is the truncation error which explicates the second-order accuracy of the method. The error introduced by using the central differencing scheme can be reduced by decreasing the distance between the nodes of the neighbouring cells $\Delta x_{PI}$. This implies a refinement of the grid. By using expression (4.10) and neglecting the truncation error, the diffusion term can be written as:

$$\int_{\partial V} (\Gamma_\varphi \nabla \varphi) \cdot n \, dA \approx \sum_i \left(\Gamma_{\varphi,i} \frac{\varphi_I - \varphi_P}{\Delta x_{PI}}\right)_i = \sum_i D_i (\varphi_I - \varphi_P) \tag{4.11}$$

where $D_i$ is the diffusion coefficient defined as:

$$D_i = \frac{\Gamma_{\varphi,i}}{\Delta x_{PI}} \tag{4.12}$$

The diffusivity can be evaluated as a mean value by using:

$$\Gamma_{\varphi,i} = \frac{2\,\Gamma_{\varphi,I}\,\Gamma_{\varphi,P}}{\Gamma_{\varphi,I} + \Gamma_{\varphi,P}} \tag{4.13}$$

- **Convective term**: it is a surface integral similar to the diffusion term, but in this case there is no derivative to estimate:

$$\int_{\partial V} (\rho \varphi \boldsymbol{u}) \cdot n \, dA \approx \sum_i (F \varphi A)_i \tag{4.14}$$

where

$$F_i = \rho \boldsymbol{u_i} \tag{4.15}$$

Considering the value that φ assumes on the common face between the cell with centre P and its generic neighbour with centre *I*, it can be estimated again with a central differencing scheme:

$$\varphi_i = \frac{\varphi_P + \varphi_I}{2} \tag{4.16}$$

The central differencing scheme is still second-order accurate, but it does not account for the effects of the flow direction. This does not satisfy the

transportiveness property especially when $Pe > 2$, inducing high instability while running the simulation.
To solve this problem, most of CFD codes use the upwind differencing scheme (UDS), by which:

$$\varphi_i = \begin{cases} \varphi_I; & (\boldsymbol{u} \cdot \boldsymbol{n})_i < 0 \\ \varphi_P; & (\boldsymbol{u} \cdot \boldsymbol{n})_i > 0 \end{cases} \tag{4.17}$$

In this case $\varphi$ evaluated in the face node assumes the same value of the upstream centre node depending on the flow direction. The UDS satisfy the transportiveness but it is only first-order accurate. To evaluate the error committed by using it, it is useful to analyse the Taylor expansion of $\varphi_i$:

$$\varphi_i \approx \varphi_P + (x_i - x_P)\left(\frac{\partial \varphi}{\partial x}\right)_i + \frac{(x_i - x_P)^2}{2}\left(\frac{\partial^2 \varphi}{\partial x^2}\right)_i \tag{4.18}$$

The last term is similar to the diffusion term described before, with the Laplacian operator. This term, when it is neglected during the simulations, introduces the so-called numerical diffusion. When this happens, the fluid diffusivity is overestimated and the system behaves like as it had a higher viscosity than what it is observed in real experiments. This problem becomes more evident when coarse grids with high skewness and not aligned with the flow direction are used. To limit this issue and maintaining the transportiveness, it is possible to use higher order upwind differencing schemes, like the SOUDS (second order upwind differencing scheme). The accuracy results improved in exchange of an increase of computational time and costs.

- **Source term**: it is a volume integral that can be estimated as:

$$\int_{\partial V} S_\varphi \, dV \approx S_{\varphi,P} \, V \tag{4.19}$$

Where usually $S_{\varphi,P}$ is expressed as a function of $\varphi_P$:

$$S_{\varphi,P} = {S_{\varphi,P}}^{rhs} + {S_{\varphi,P}}^{lhs} \, \varphi_P \qquad \begin{cases} {S_{\varphi,P}}^{rhs} > 0 \\ {S_{\varphi,P}}^{lhs} < 0 \end{cases} \tag{4.20}$$

The signs of the different terms are such to satisfy the boundedness property. ${S_{\varphi,P}}^{rhs}$ becomes $S_u$ on the right-hand side of the equation (4.7), while ${S_{\varphi,P}}^{lhs}$ contributes to $a_P$ on the left-hand side of the same equation.

- **Temporal integrals**: assuming the central node value of $\varphi$ to be representative of the whole control volume, the rate of change of $\varphi$ in equation (4.6) can be approximated as:

$$\int_t^{t+\Delta t} \int_V \frac{\partial(\rho\varphi)}{\partial t} dV \, dt \approx \rho \, (\varphi_P^{t+\Delta t} - \varphi_P^t) \, \Delta V \tag{4.21}$$

Where the term with apex t is computed at the previous time step while the term with apex $t + \Delta t$ is evaluated at the following time step. The term corresponding to the new time step can be written using:

$$\int_t^{t+\Delta t} \varphi_P \, dt \approx [\theta \, \varphi_P^{t+\Delta t} + (1-\theta) \, \varphi_P^t] \, \Delta t \tag{4.22}$$

$\theta$ is a weighting parameter. If $\theta$ = 0 the value of $\varphi$, relative to the new time step, is computed using only values from the old time step; this is the so-called forward Euler method and it is fully explicit. Instead, if $\theta$ = 1, a fully implicit method called backward Euler method is obtained; in this case only values coming from the new time step are used. Finally, if $\theta$ = 0.5 it is obtained the Crank-Nicolson method. This is a second-order accurate method differently from the first two that belong to first-order category.
Explicit methods require less computational time, but they are not stable when a time step $\Delta t$ too large is used. Instead implicit methods are more time demanding, but they are very robust since they are unconditionally stable and boundedness is always guaranteed.

It must be underlined that the properties and convergence criteria described in this paragraph are referred to the Eulerian phase. While, if it is considered the Lagrangian phase and the coupling between the two phases, the situation becomes more complex. The literature tells that there is a lack of statistical convergence in the Lagrangian treatment of the liquid phase (for a more detailed description of this topic refer to [16] and [23]). Further on, in this work, some numerical aspects, related to the Lagrangian phase and its coupling with the Eulerian one, are studied and analysed.

## 4.3. SOLUTION ALGORITHMS AND PRESSURE-VELOCITY COUPLING

In expression (4.7) pressure was not explicit and it was accounted in the source term for simplicity. However, the correct resolution of the pressure field is necessary to solve correctly the momentum equations and to obtain the velocity field. Pressure and velocity are intrinsically coupled, since considering continuity equation and the momentum equations there is no an explicit expression for pressure. Usually the iterative methods used to solve the algebraic equations, obtained during the discretization phase, predict pressure and the three components of velocity from the three momentum equations, while the continuity equation is used for the pressure correction.

To understand how these iterative methods work, it is useful to make the pressure explicit in the algebraic equations. The general pressure term can be approximated as:

$$\int_V \frac{\partial p}{\partial x} \, dV = \int_{\partial V} p \, dA \approx \sum_i (p_P - p_I) A_i \tag{4.23}$$

If it is substituted in the momentum equations expressed as (4.7),(4.6) it is obtained:

$$a_P \boldsymbol{u}_P = \sum a_{nb} \boldsymbol{u}_{nb} + b_i + (p_P - p_I) A_i \tag{4.24}$$

where $b_i$ accounts for the source terms without including pressure. In general, the iterative methods express pressure and velocity as a sum of a predicted value (*) plus a correction value (‘):

$$\boldsymbol{u} = \boldsymbol{u}^* + \boldsymbol{u}' \tag{4.25}$$

$$p = p^* + p' \tag{4.26}$$

### 4.3.1. SIMPLE Method

The SIMPLE (Semi-Implicit Method for Pressure-Linked Equations) method is used as default for the pressure-velocity coupling for steady state flow since it is very robust. As first, it is used a trial value for pressure, $p^*$, to solve the momentum equations and to obtain the predicted values of the velocity component ($u^*$, $v^*$ and $w^*$). In the following description of the method only the component u is showed for simplicity, but the same speech can be done also for v and w:

$$a_P u_P^* = \sum a_{nb} u_{nb}^* + b_i + \left(p_P^* - p_I^*\right) A_i \tag{4.27}$$

By subtracting this expression to equation (4.24) and exploiting the definitions given by (4.25) and (4.26), it is obtained:

$$a_P u_P' = \sum \cancel{a_{nb} u_{nb}'} + \left(p_P' - p_I'\right) A_i \tag{4.28}$$

This method introduces the fundamental approximation by which the term containing the influence of the neighbour nodes is neglected; this can be done because it tends to 0 at convergence. This equation is used to find the velocity correction $u'$.
Given the continuity equation expressed as:

$$\sum F_i u_i = 0 \tag{4.29}$$

and combining it with (4.25) and (4.28) it is possible to find an expression in which the pressure correction is the only unknown:

$$a_P p_P' = \sum a_{nb} p_{nb}' + B \tag{4.30}$$

Where $B$ is a term that is function only of the predicted values of velocity $u^*$.
To check if the convergence is reached, they are monitored residuals as reference quantities. Considering the general conservation equation written in the algebraic form, they are defined as the modulus of the difference between the left-hand side and right-hand side of the equation. For example, from equation (4.7) :

$$res = \left| a_P \varphi_P - \left( \sum a_{nb} \varphi_{nb} + S_u \right) \right| \tag{4.31}$$

The SIMPLE method can be represented by the following cycle of steps:

1. Guess a trial value for pressure $p^*$
2. Solve the momentum predictor given by (4.27) to get $u^*$
3. Solve the first pressure correction (4.30) to get $p'$
4. Perform the velocity correction (4.28) to get $u'$.
5. Find the values of $u$ and $p$ from the definitions (4.25) and (4.26)

6. Check convergence by comparing the initial residuals of the momentum predictors and pressure correction with the desired tolerance. If the method is not converged repeat the cycle starting from the point 2.

To improve the stability of the method the new values of $p$ and $u$ are obtained using under relaxation factor that allows to reduce the possible divergence issues:

$$u^{new} = \alpha_u u + (1 - \alpha_p)\, u^{old} \tag{4.32}$$

$$p^{new} = p^* + \alpha_p p' \tag{4.33}$$

With relaxation factors close to 1 the method results faster but less stable, while if they are close to 0 the opposite happens.

The SIMPLE method is widely used in steady state simulations due to its robustness, but when unsteady situations are present, they are preferred other methods that apparently require more memory and time per each iteration, but it is demonstrated that they are faster and more efficient.

### 4.3.2. The PISO Method

The PISO (Pressure Implicit with Splitting of Operators) method is widely used for pressure-velocity coupling in unsteady simulations since it performs better than the SIMPLE algorithm. It involves a predictor step and two subsequent correctors steps. The predictor and the first corrector step are performed following the same procedure used for in the SIMPLE method, but in this case, before starting the iterative loop, it is done a second corrector step.

Each generic variable can be written as:

$$\varphi^{***} = \varphi^{**} + \varphi'' = \varphi^* + \varphi' + \varphi'' \tag{4.34}$$

where $\varphi'$ and $\varphi''$ are respectively the first and second $\varphi$ corrections; while $\varphi^*$ is the predicted value (the same present in the SIMPLE algorithm) and $\varphi^{**}$ is a second prediction obtained after the first correction step. During the predictor and the first corrector step the values of $\varphi'$ and $\varphi^{**}$ are obtained starting from a guessed value of pressure $p^*$. The second corrector step is performed similarly to the first one, starting from $\varphi^{**}$ to find $\varphi^{***}$. During this step, differently from SIMPLE routine, the term that contains the contribution of the neighbour cells is not neglected like in equation (4.28).

PISO method was initially developed for non-iterative computation of unsteady compressible flows, but it has been proved that it performs very well when it is used for unsteady simulations. In these cases, it provides a quicker convergence with respect to SIMPLE method even if it seems to be longer to perform and more complicated.

### 4.3.3. The PIMPLE Method

As the name suggests, it is the combination of the SIMPLE and PISO methods. It is commonly adopted by OpenFOAM to perform unsteady simulations. Similarly to the PISO algorithm, each variable is decomposed using different correctors. For each time

step they are performed two iteration cycles, one inside the other: the inner one is based on the SIMPLE algorithm with inner correctors, while the outer one, with the corresponding correctors, is performed only once the inner cycle has reached convergence. Once a time step is solved it is possible to move towards to the next one.

PIMPLE method is preferred respect to PISO because it is more stable and it allows to use larger time steps and greater Courant numbers.

# 5. BREAKUP MODELS: VALIDATION AND CALIBRATION

In this chapter, different numerical simulations of spray G are performed for the conditions specified by ECN. The objective for this part of the work is to assess the performances of different breakup models (with a special focus on secondary breakup models) comparing the numerical results with experimental data. A calibration of the parameters is performed when this is required by the model; meanwhile, the effects produced while varying their values is studied.

This assessment of performance wants to extend and possibly improve the results presented during previous ECN workshops. The numerical setup presented during 2018 by Lucchini and Paredi in [3] can be considered the actual state of art for numerical simulations of spray G. It is chosen as starting point from which a series of analysis are performed to test different breakup models. The results obtained are always compared to experimental data looking for the numerical setup that better reproduce them.

All the simulations presented in this thesis work were run using OpenFOAM (version 2.2.x) extended with the library LibICE (version 2.2.x). OpenFOAM, which stands for Open Source Field Operation and Manipulation, is an open source CFD code based on C++ programming language produced by OpenCFD ltd and released under GNU General Public License [24]. The LibICE extension is a library created in Politecnico di Milano by the ICE (internal combustion engine) group [25]. It has been developed to improve the CFD code for the specific case of internal combustion engines simulations.

## 5.1. STATE OF ART OF SPRAY G NUMERICAL SIMULATIONS

Starting from the results presented during the 6$^{th}$ ECN workshop (ECN6), the numerical state of art is defined and it is adopted as reference for the first part of this thesis work where the effects of sub-models are analyzed. The setup proposed by Politecnico di Milano and presented by Lucchini and Paredi during ECN6 [3] is currently the one that ensures the best results on spray G simulations. In the next paragraph, this numerical setup is described together with the results that it provides. Its strengths and weaknesses are then analysed to understand the critical issues in spray G simulations.

### 5.1.1. Input Documentation

The reference setup is described according to the standard suggested for the documentation of CFD simulations that is proposed by [14].

- Code used for simulation: OpenFOAM-2.2.x with the library LibICE-2.2.x
- Description of the geometry: the system is composed by a constant-volume vessel with the shape of a box (0.1 x 0.1 x 0.07 m). The injector is located in the centre of the bottom face. The spray is injected towards the positive direction of the z-axis.

- Computational mesh: the initial grid is a 3D structured and cartesian (the grid lines are parallel to the axes of the reference system) mesh composed all by cubical elements with a side length of 2.0 mm. The *adaptive local mesh refinement* (AMR) tool provided by OpenFOAM is used. At each time step, this function automatically refines the mesh in the cells where a certain quantity assumes a value that belongs to a user-defined range. The geometric field used as a refinement criterion is the total fuel mass fraction (liquid and gas) defined as:

$$Y_{l+g} = \frac{m_{f,l} + \rho Y_{tf} V_{cell}}{\rho\, V_{cell}} \tag{5.1}$$

where $m_{f,l}$ is the mass of all the liquid parcels present inside the cell, $Y_{tf}$ is the fuel mass fraction in the continuous phase, $\rho$ is the gas phase density and $V_{cell}$ is the volume of the cell. The refinement is performed where this quantity belongs to the range $[10^{-2}; 1]$. A refinement level needs to be specified: for each level every side of the original cell is divided in two equal parts creating the sides of the new cells. This concept is clearly represented in Figure 5.1. For spray G simulation a level of refinement equals to 2 is recommended. This choice is suggested by [23] where the optimal cell size is studied for this kind of problems. Starting from the initial mesh, with such refinement level, the new cells are characterized by a side length of 0.5 mm. The use of AMR allows to save computational time with respect to a fixed grid adopting the same cell refinement to describe the system.

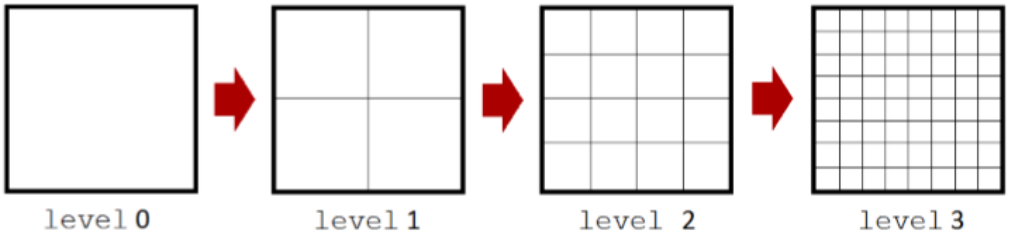


***Figure 5.1 - Representation of the mesh refinement process with different refinement levels***

- Time discretization: the start time is set to 0 s, while the end time corresponds to 2.0 ms. The chosen time-step is 0.001 ms.
- Boundary conditions: the sides of the constant-volume vessel are all modelled as walls and the Lagrangian parcels of fluid that hit them are removed from the simulation. So, the parcels are not bounced back and there is no wall impingement of fuel.
- Initial conditions: they are implemented according to the specifications described in chapter 1. A constant temperature field of 573 K is imposed, while for pressure a constant field of 6 bar is imposed. The Eulerian phase velocity is equal to 0 over all the system, while no Lagrangian parcels are initially present. Initially, the vessel is full of inert gas composed only by $N_2$.
- Fluid properties: in the system two species are present: N2, that represents the inert gas, and iso-octane, that is the fuel. The gas phase is treated as an ideal multicomponent mixture with the ideal gas law. The Newtonian fluid and the

isotropic fluid assumptions are applied. The liquid is a Newtonian and isotropic fluid with temperature dependant properties.

- Turbulence modelling: the standard k-ε model is adopted with the default coefficients (already defined in (3.27)) with the only exception of $C_{1\varepsilon} = 1.5$ as suggested for jets and sprays simulations.
- Spray properties: the atomization (or primary breakup) model used is the Huh-Gosman with the KHRT model for secondary breakup. The collision of particles is neglected since collision models bring to possible convergence issue (according to [16]). The drag model used is the spherical drag model and the Adachi flash boiling evaporation model is implemented for evaporation.
- Injector model: the spray angle is imposed equal to 16.5°; this value is obtained from experimental observations on spray G. The area contraction coefficient $C_d$ is imposed equal to 0.72. This value is obtained from some experimental measurements and it is adjusted to fit experimental data. According to the theoretical description of primary breakup models, as the area contraction coefficient is reduced, the velocity of the injected liquid is increased to maintain the same mass flow rate, since the effective flow area is reduced. So, by changing $C_d$, penetration and velocity values can be adjusted.
- Solution algorithms: the solver *PimpleColdSpeciesFoam* implemented in the LibICE library is used. It is based on the PIMPLE algorithm and it is optimized for simulations where there is a multicomponent mixture without combustion.
- Discretization schemes: the time is discretized using a Euler scheme, while divergences and gradients are discretized with the Gauss scheme (second order accurate)
- Convergence criteria: at each time step, the convergence is reached when the residuals become smaller than a certain limit. In particular, the threshold values are imposed equal to $10^{-10}$ for velocity, $10^{-9}$ for density and $10^{-8}$ for pressure and total fuel mass fraction.
- Relaxation factors: they are all set equal to 1.

### 5.1.2. Results reporting and interpretation

The results are postprocessed following the guidelines proposed in the previous ECN workshops. First, the data for liquid penetration as function of time are compared to the experimental data shared by Sandia (Figure 5.2), according to the standard and the two threshold values described in chapter 3. The lines corresponding to experimental measurements are drawn with the corresponding error bars, since the Sandia data are provided together with the standard deviation.

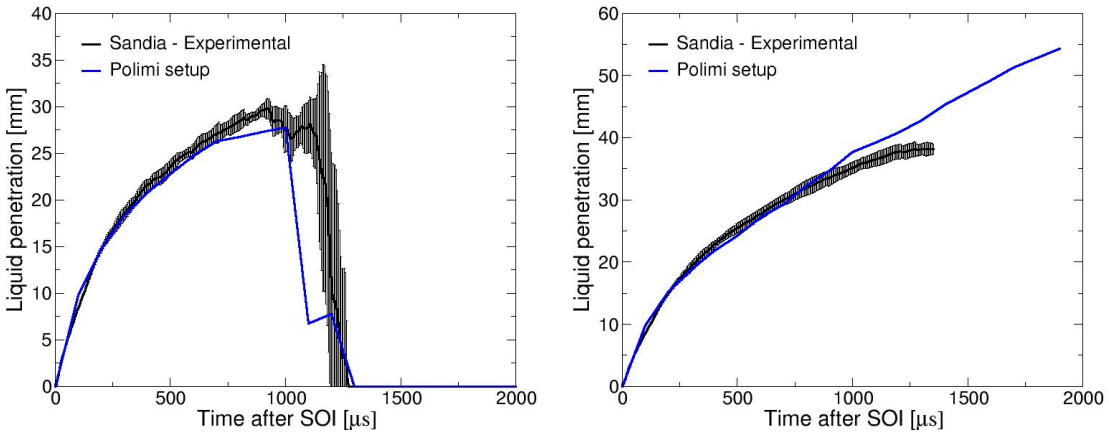


***Figure 5.2 - Liquid penetration for the reference setup according to the two LVF thresholds suggested: 2mm³/mm² (a) and 0.2 mm³/mm² (b)***

Also the vapor penetration data as function of time are compared with experimental measurements from Sandia, the results are plotted in Figure 5.3. It is possible to notice that the numerical results provide good predictions for liquid penetration especially during the injection process (corresponding to time values smaller than 0.8ms after SOI) while after the end of injection there are some discrepancies among them and experimental data. Instead, the vapor penetration resulting from the numerical simulation slightly underpredicts the experimental results.

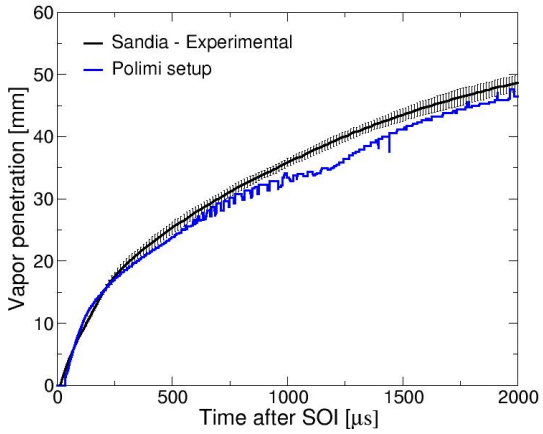


***Figure 5.3 - Vapor penetration as function of time***

After the penetration values, the profiles of SMD, liquid velocity and vapor velocity as function of the radial position (distance from the axis of the injector) are evaluated using a cutting plane perpendicular to the z-axis and located 15 mm above the injection position, as represented in Figure 5.4. These profiles are evaluated for three different time values: 0.3 ms, 0.6 ms and 1.2 ms after the start of injection. They are respectively a time step approximately in the middle of the injection process, a time step close to the end of injection and a time step sufficiently far from it.

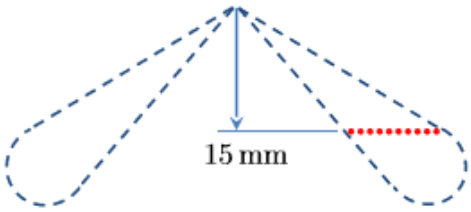


***Figure 5.4 - Representation of the cutting plane used for the sampling of the quantities of interest***

The SMD obtained by numerical simulations are compared with experimental values from General Motors (GM). In this case the standard deviation for experimental data is not provided. In Figure 5.5, it is possible to notice that the numerical simulation underestimates the SMD in all the time steps considered: the real measured diameters are almost twice.

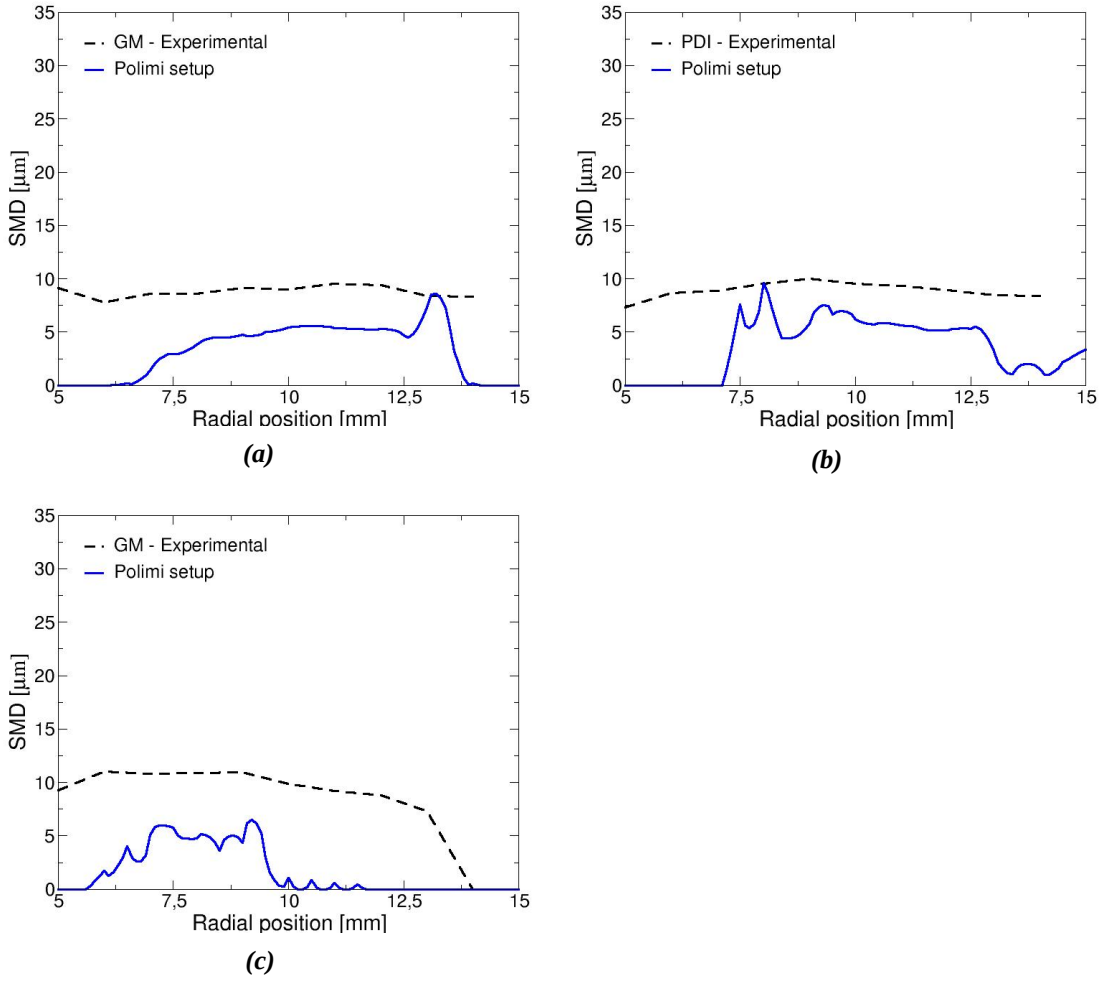


***Figure 5.5 - Radial distribution of SMD for 0.3 ms (a), 0.6 ms (b) and 1.2 ms (c) after SOI***

About velocities, the experimental data provided by General Motors refer to the axial component (directed as the z-axis) of the liquid droplet velocity. Also for these data,

there are no information about the distribution of the measurements. The numerical results report information about both the axial liquid velocity (dashed line) and the axial velocity of the gas phase (solid line). As illustrated by Figure 5.6, during injection (a and b) the predicted liquid velocity curve exhibits a central peak that is greater than the one provided by experimental measurements, while at the borders of the plume (corresponding to low and high values of radial position) the real observed velocities are greater than the ones predicted by CFD calculations. Instead for Figure 5.6 (c), that is representative of a time step after the end of injection, the numerical calculations underestimate the liquid velocity profile.

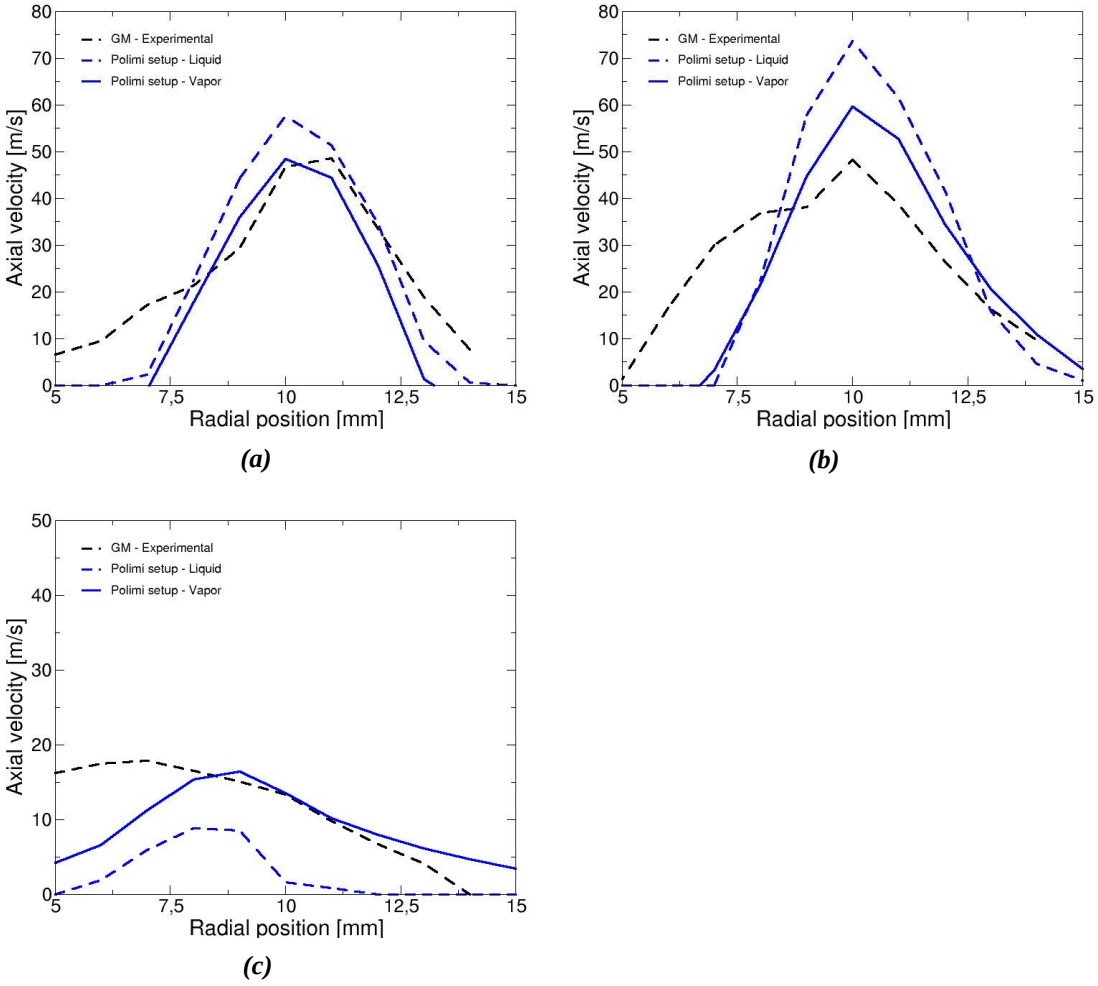


***Figure 5.6 - Liquid and Gas phase axial velocity for three time steps: 0.3 ms (a), 0.6 ms (b), 1.2 ms (c)***

Another useful indicator to assess the performances of the numerical simulation is the graph reported in Figure 5.7. It represents the axial velocity of the gas phase as function of time. The sampling point for this plot belongs to the z-axis and it is located 15 mm above the injection position. This location is interesting to be studied since it is in the middle of the crown created by the spray plumes corresponding to the so-called entrainment region (this region corresponds to the borders of the spray plumes where fuel

and gas come in contact creating the fresh charge). It allows to evaluate the gas motion induced by the fuel injection. The motion conditions here are very important since they are the responsible of the air entrainment that plays a crucial role in the evaporation of liquid fuel. The more the air entrainment is intense, the quicker is the evaporation, since a greater quantity of air penetrates deeply inside the plumes coming in contact with liquid fuel. This velocity profile is the result of the complex interaction between the gas vortexes generated by the spray. In this case the experimental data are provided by Sandia and their standard deviation is available. As it is possible to notice in Figure 5.7, the gas velocity results slightly overestimated in the numerical simulation for time values greater than 1.0 ms when the injection process ends. This graph, together with penetration data, represents one of the crucial quantities for the assessment of the numerical setup used.

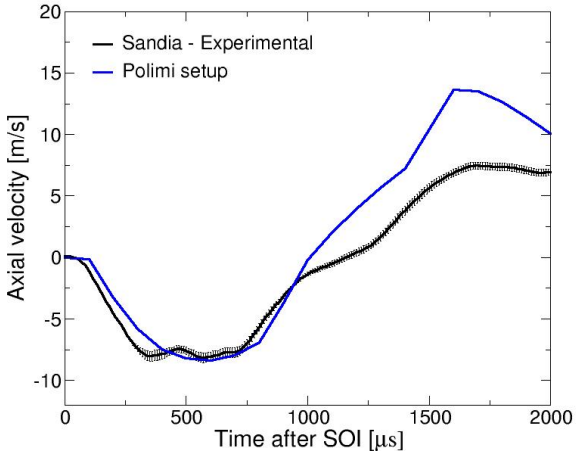


***Figure 5.7 - Axial velocity of the gas phase as function of time on the injector axis***

The last comparison is performed considering the radial density sampled at 0.6 ms after SOI (start of injection) measured on the z-axis 2 mm above the injection position. The sampling point is very close to the injector and it is located very close to the expected end of the liquid core. This plot allows to evaluate the performances of the KHRT model inside the liquid core length where only the KH breakup mechanism is present. The experimental data presented in Figure 5.8 are provided by Argonne National Laboratories without any information about their distribution. In this case, the numerical results provide a peak of density that is smaller than the one provided by experimental data. Moreover, the peak produced by CFD simulations is shifted to the left, corresponding to points located closer to the injector axis.

To summarize the results achieved by this numerical setup, it is possible to state that the penetration values are predicted with a good accuracy, while there is an underestimation of the $SMD$. At the same time the liquid velocity obtained by the simulation is greater than what is expected from experimental data during the injection process, but it is lower after that fuel injection is ended. This behaviour can be explained looking at the area contraction coefficient used for this simulation ($C_d$=0.72). When a small $C_d$ is adopted, the liquid velocity is increased and the aerodynamic interactions with surrounding air becomes stronger. This leads to an excessive breakup of the parcels that exhibit a lower $SMD$ than expected. At the same time, the overestimation of these

velocities allows to compensate the numerical error resulting from the use of a non-oriented spray grid, which tends to reduce the parcel velocity. According to what Stiesch asserts in [16], when a Lagrangian parcel crosses a grid line with a velocity that is not perpendicular to it, a numerical effects by which the parcel behaves like it is slowed down is observed. The compensating effect here described allows to have good predictions for penetration values, but it introduces errors in the velocity and $SMD$ predictions. In chapter 7 numerical effects are further investigated.

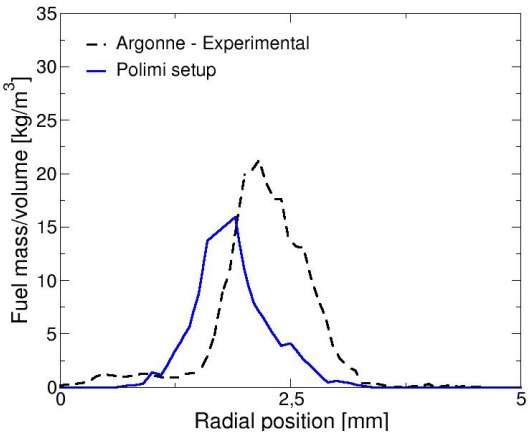


***Figure 5.8 - Radial distribution of density sampled at 0.6ms after SOI***

Another possible issue is found by looking at the spray morphology and the axial LVF graph (Figure 5.9). It is possible to notice how the numerical predicted spray has a plume core composed by liquid fuel that evaporates much later than what is observed in the experiments performed by the University of Melbourne. In particular, in the proximity of the tips of the plumes, the fuel evaporates hardly and the corresponding LVF is bigger than experimental data. Considering that the $SMD$ predicted are small, providing a favourable situation for evaporation, the poor evaporation can be provided by a non-accurate prediction of the air entrainment.

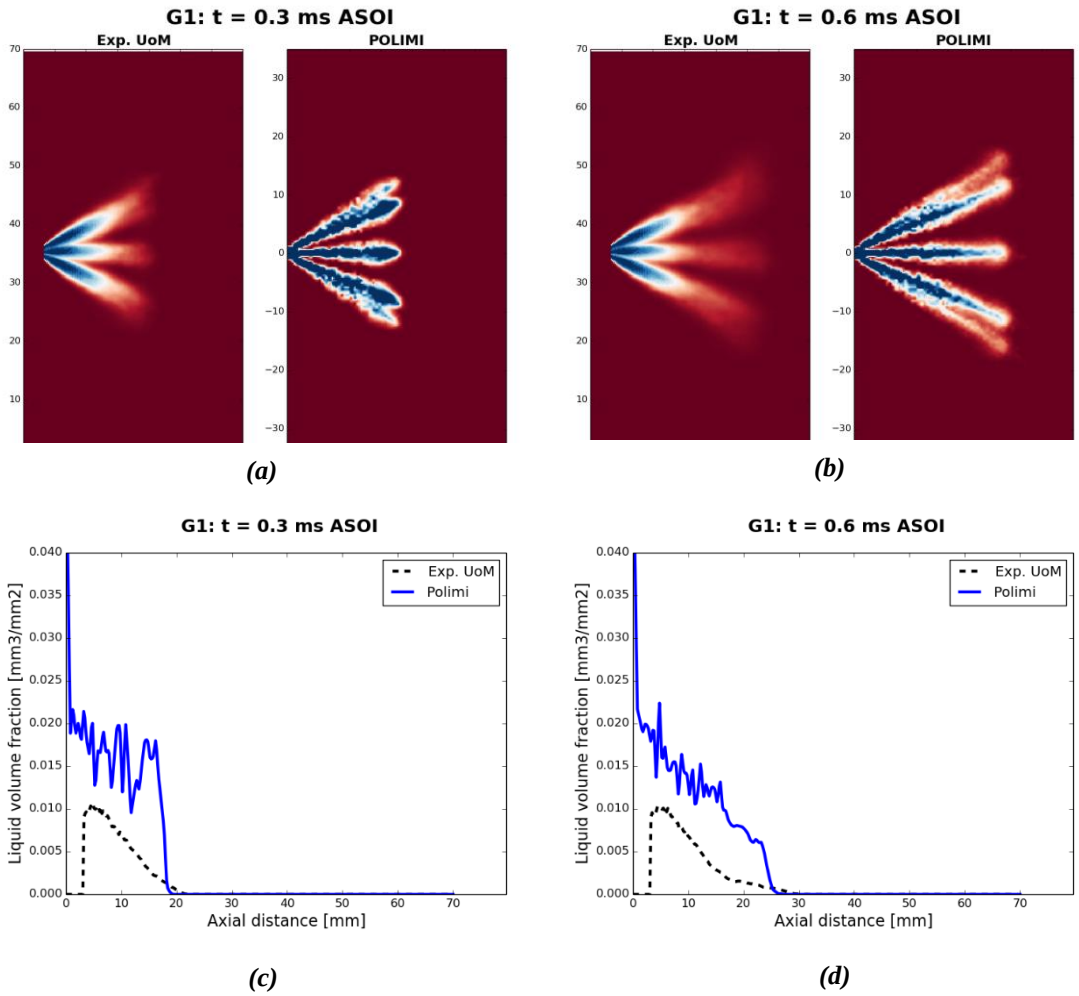


***Figure 5.9 - Spray morphology (a and b) and axial LVF graph (c and d) for two different time steps***

## 5.2. SECONDARY BREAKUP MODELS: ASSESSMENT OF PERFORMANCE

In this section of the work alternative secondary breakup models are tested to assess their performances. The objective is to understand how they affect the results and to evaluate if any of them can improve the results of the base setup.

The breakup models considered are the TAB (Taylor Analogy Breakup), ETAB (enhanced-TAB) and Pilch-Erdman models. TAB and ETAB models (presented in [4] and [5] respectively) were commonly used in the past since they were the first ones that guaranteed acceptable predictions of spray breakup; but, after that KHRT model was introduced, their usage progressively decreased because of the better performances provided by KHRT. More detailed information about these two models are presented in [16]. Anyway, for the sake of completeness their performances are evaluated and compared to experimental data.

The Pilch-Erdman model is not widely used and there are poor studies about it on the literature. This is because KHRT model, that is commonly used for this kind of problems in the CFD simulations, offers good performances in many applications and it is more historically rooted.

### 5.2.1. Results Reporting and Interpretation

The CFD simulations are run with the same setup described for the KHRT model changing only the secondary breakup model. They have been used the TAB, ETAB and Pilch-Erdman (PE) models with the constants set as default.

For all the three cases studied here, the liquid penetrations with the two threshold values are plotted on the same graph in Figure 5.10. TAB and ETAB models provide very similar results and, according to them, penetrations are strongly overestimated. The corresponding curves are quite overlapped and they become flat as they reach the penetration value of 70 mm. This means that the spray plumes hit the wall on the opposite side of the vessel with respect to the injector position before that the liquid evaporates. This is completely inconsistent with experimental data. Instead considering the curves for the Pilch-Erdman model, the results are closer to the trend provided by experimental data.

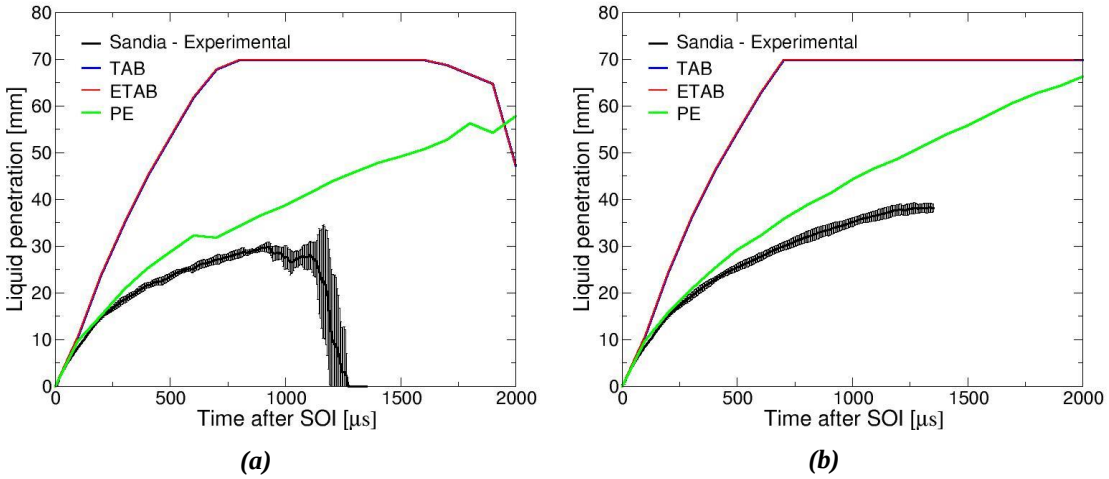


***Figure 5.10 - Liquid penetration for the TAB, ETAB and Pilch-Erdman models according to the two thresholds of LVF 2 $mm^3/mm^2$ (a) and 0.2 $mm^3/mm^2$ (b)***

Similar considerations can be done also for vapor penetration data (Figure 5.11). TAB and ETAB models provide overestimated vapor penetrations; in these cases, the plumes of liquid move towards the vessel wall dragging with them the vapour that is formed by evaporation. Instead, Pilch-Erdman model gives results in better agreement with experimental data

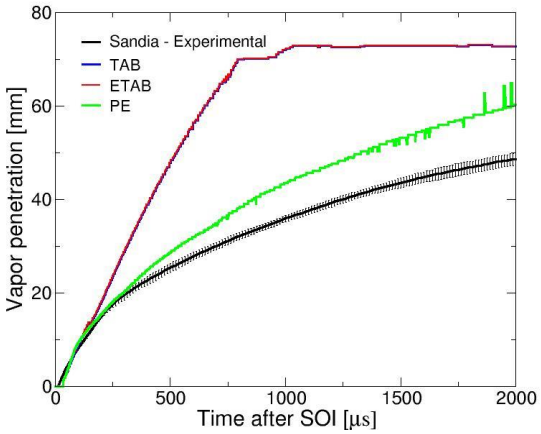


***Figure 5.11 - Vapor penetration for TAB, ETAB and Pilch-Erdman models***

Analysing the SMD, TAB and ETAB models provide results very different form experimental data; considering for example a time step in the middle of the injection process (0.3ms) and a time step close to the end of injection (0.6ms) the SMD predictions are significantly higher than experimental measurements of the diameters (Figure 5.12). Also in this case, the Pilch-Erdman model is not so accurate to predict experimental data but it provides results that are coherent to what happens physically.

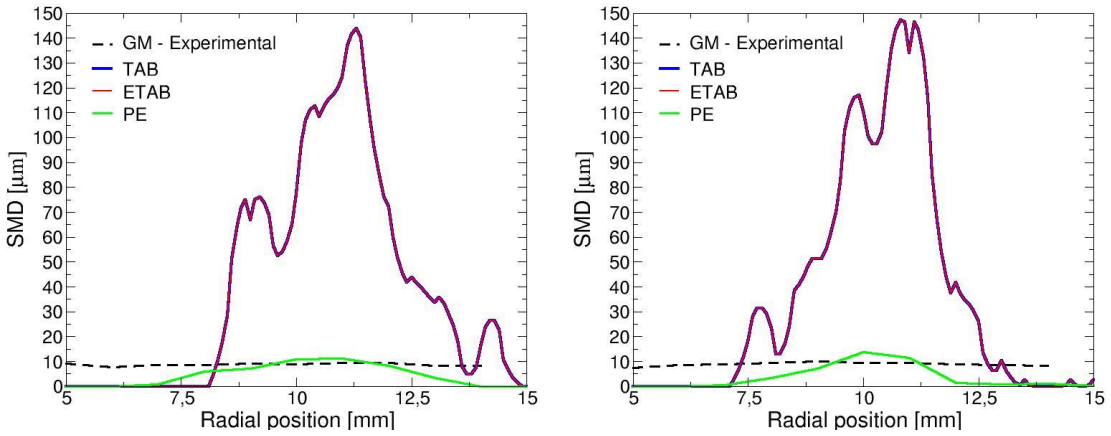


***(a)*** ***(b)***

***Figure 5.12 - Radial SMD distribution for the different breakup models at 0.3 ms (a) and 0.6 ms (b) after SOI***

By simply analysing these outputs, it is possible to draw some conclusions: TAB and ETAB models provides very similar results, but the droplet breakup predicted by them is very poor. This results in a spray with very big drops that cannot be broken into smaller ones; so, a high volume to surface ratio is maintained with a consequent slow evaporation. The plumes composed by big liquid drops penetrates deeply into the inert gas reaching the walls of the vessel. The morphology of the spray for the TAB model after 0.5 ms ASOI clearly confirm this (Figure 5.13). The numerical result is very different from what it is observed during experiments.

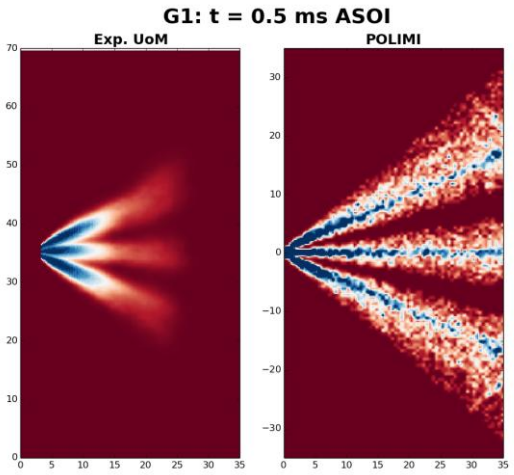


***Figure 5.13 - Morphology of the spray obtained with TAB model (right) versus the experimental results (left)***

Instead Pilch-Erdman model provides results that are consistent with experimental data, even using values for the constants that are not calibrated for this case. That is why further investigations to deeply investigate the performances of this model are performed.

## 5.3. PILCH-ERDMAN MODEL: CALIBRATION AND VALIDATION

The results obtained with the Pilch-Erdman model seem to be promising even using the default coefficients. More detailed analysis about it are necessary to really understand its performances. As first, this model is calibrated changing the constant $B_2$ trying to obtain predictions for the spray that are as close as possible to experimental data.

After that a sensitivity analysis on the number of parcels injected into the system is performed and the effect of the Huh-Gosman primary breakup effect is evaluated. Finally, the so-called counterbore effect is assessed.

Once all these studies are performed, strengths and weaknesses of this breakup model can be identified.

### 5.3.1. Calibration of the Constant $B_2$

Pilch-Erdman model contains two adjustable constants that needs to be calibrated to fit experimental data. According to previous experiences performed by the ICE group with this model in diesel engines simulations, the most significant effects are shown when the $B_2$ parameter is changed. $B_2$ is the constant that multiplies the squared term in equation (3.68). As this value decreases, the maximum stable diameter decreases too. The droplet diameter is reduced more quickly and the penetration values are decreased since smaller droplets are present in the spray.

To perform this calibration, some simulations are run using the same setup described in previous paragraphs and adopting the Pilch-Erdman model for secondary

breakup with different values for the constant $B_2$. The first simulation uses the default value for $B_2$ = 0.165, then two simulations are performed where $B_2$ has been doubled and halved respectively. After that, other attempts are run trying to fit experimental data exploiting the results obtained with the previous attempts. In the following description, they are shown the results corresponding to five values of $B_2$: 0.330, 0.165, 0.0825, 0.040 and 0.020.

Looking at the liquid penetration graphs (Figure 5.14), it is possible to notice that as the value of $B_2$ decreases, the penetration decreases too and the corresponding curves get closer to the experimental results provided by Sandia.

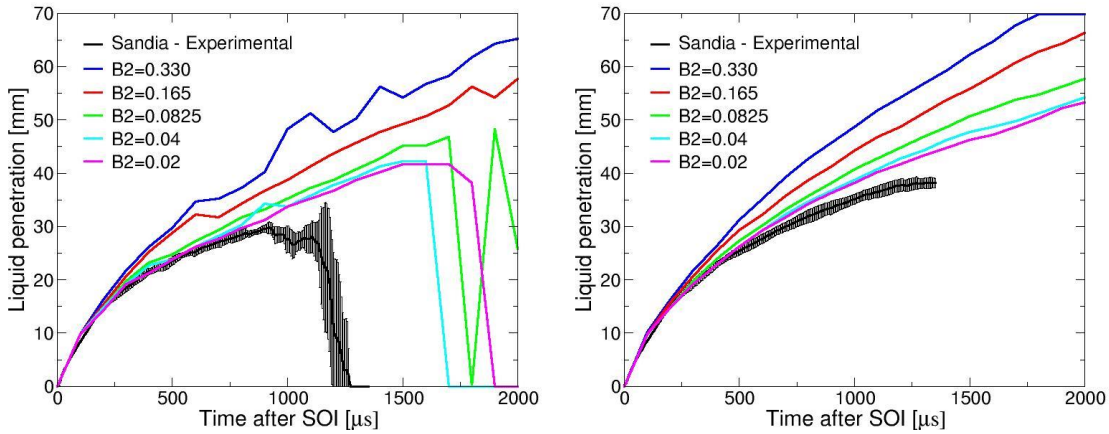


***Figure 5.14 - Liquid penetration for the Pilch-Erdman model adopting different $B_2$ according to the two thresholds of LVF 2 mm³/mm² (a) and 0.2 mm³/mm² (b)***

The same trend can be observed by looking at the vapor penetration plot, reported in Figure 5.15. Especially for low time values, the penetrations obtained adopting $B_2$ = 0.02 well fit the experimental data.

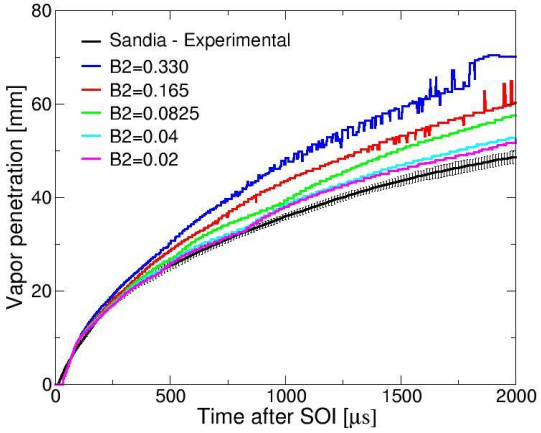


***Figure 5.15 - Vapor penetration data for the Pilch-Erdman model with different $B_2$ values***

When $B_2$ is reduced also the other postprocessed quantities approach the experimental data. The calibration of this model is very simple since it requires to study only the effects

of $B_2$ on the results. By simple adjusting this parameter very good results can be achieved. This is a consequence of the fact that this model is developed on the basis of experimental measurements.

### 5.3.2. Sensitivity Analysis on the Atomization model

Once the effects obtained when $B_2$ changes are studied, the sensitivity of the results to the primary breakup model is performed. All the cases described up to now adopt the Huh-Gosman atomization model. This model accounts for the turbulent effects inside the nozzle by providing a stripping of the newly injected parcels similar to the one described by the KH secondary breakup model. Instead the blob injection model does not account any effect due to the fuel motion inside the nozzle and it does not provide any breakup of the injected parcels. The purpose of this analysis is to understand how the use of different primary breakup models influences the simulation results if the Pilch-Erdman model is used for secondary breakup. According to previous studies presented during ECN workshops, the Huh-Gosman model is needed when KHRT model is adopted because if the turbulence effects generated inside the nozzle are neglected the experimental results cannot be predicted accurately. Two simulations are performed adopting the Pilch-Erdman model for secondary breakup with $B_2$ = 0.02. The first one uses the Huh-Gosman primary breakup model, while the second one uses the blob injection model.

The liquid penetration is very similar for both the simulations (Figure 5.16). Moreover, the numerical results well predict the experimental data, especially before the end of injection, when time is lower than 0.8 ms after the start of injection.

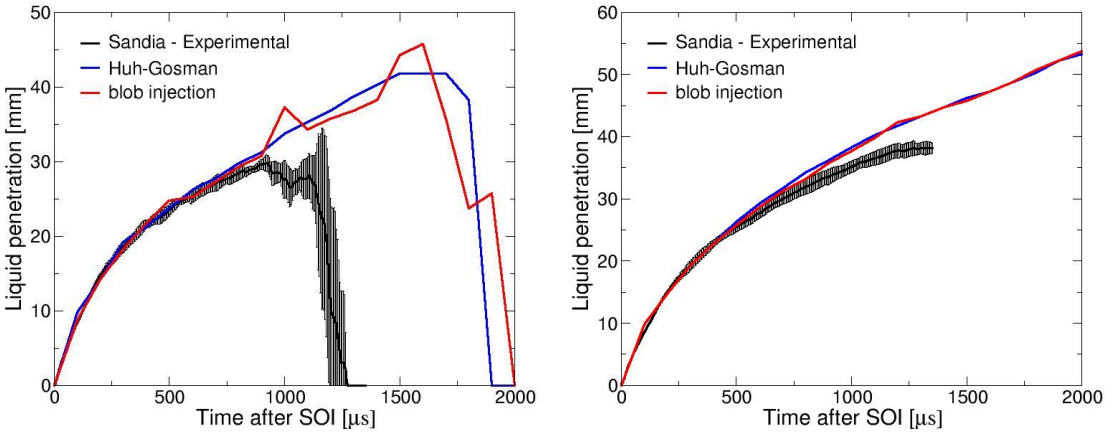


***Figure 5.16 - Liquid penetration for the Pilch-Erdman model adopting different primary breakup models according to the two thresholds of LVF 2 mm³/mm² (a) and 0.2 mm³/mm² (b)***

For vapor penetration, similar comments can be made. The simulations considered in this analysis provide very similar results (Figure 5.17). Comparing them with experimental data by Sandia, a good matching is found especially during injection. Some differences are observed only after the injection process is ended.

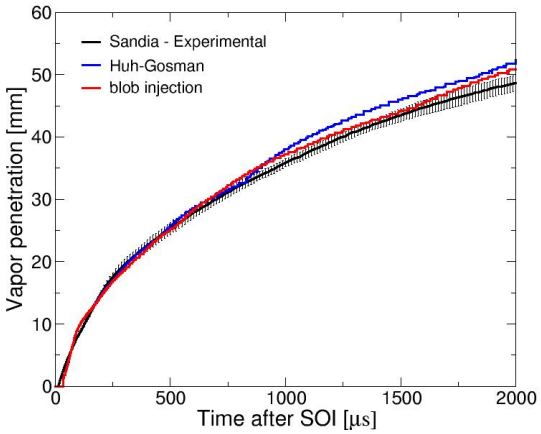


***Figure 5.17 - Vapor penetration data for the Pilch-Erdman model adopting different primary breakup models***

Also for liquid and vapor velocities the results are very similar. A slight decrease of the gas phase velocity peak for the blob injection case can be observed. Instead, the liquid velocity peak is smaller for the case with the Huh-Gosman model. This opposite trend is explained by momentum exchange between the two phases. Where the liquid is slower, the gas is faster because more momentum has been exchanged between the two phases. The SMD observed at the same time step shows how the blob injection model produces slightly bigger parcels. These differences are shown in Figure 5.18 where SMD and velocities are evaluated at 0.6 ms after SOI. Analysing also the other time steps, similar consideration can be made and very small differences can be observed.

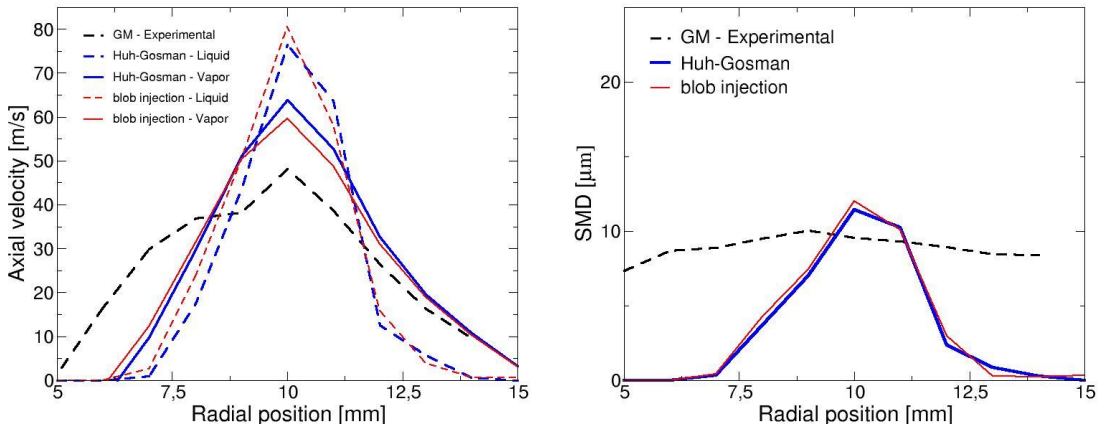


***(a)*** ***(b)***

***Figure 5.18 - Axial velocity (a) and SMD (b) as function of the radial position evaluated at 0.6 ms after SOI comparing Huh-Gosman and blob injection primary breakup model***

Summing up the considerations, the different primary breakup models perform very similarly if the Pilch-Erdman model is adopted for secondary breakup. As described in chapter 3, Huh-Gosman model extends the blob injection model accounting also for the turbulent motion at the nozzle outlet. The difference in the results is not such evident to

justify the adoption of the more complex Huh-Gosman model instead of the simpler blob injection that is easier to be implemented and faster to run. According to these results, the breakup mechanism described by Pilch and Erdman does not exhibit strong variations if the turbulence effects on the nozzle outlet are accounted or not.

### 5.3.3. Sensitivity Analysis on the Number of Particles Injected

As described during chapter 2, the Lagrangian field of the simulation is represented by a certain number of parcels that statistically represent all the liquid drops present in the system. This approach allows to describe the behaviour of all the droplets (order of $10^6$) by simulating only a certain number of parcels that can be decided by the operator before performing the simulation. As this number increases, the spray description improves in exchange of an increase of computational time. Instead, by adopting few parcels the simulation is faster, but the results are not representative of the real spray behaviour. In this sensitivity analysis the attention is focused on studying how the results change if the number of injected particles is changed.

In all the simulations, blob injection model for primary breakup and Pilch-Erdman model ($B_2$ = 0.020) for secondary breakup are adopted. The three cases compared there differs only for the number of parcels injected. 65000, 100000 and 300000 parcels are used respectively. The resulting liquid penetration with the LVF threshold of 2 $mm^3/mm^2$ for the cases with 100000 and 300000 parcels are very similar and they are closer to experimental data with respect to the case with 65000 parcels. Instead considering the other threshold value for LVF, no significant differences are observed among the three cases.

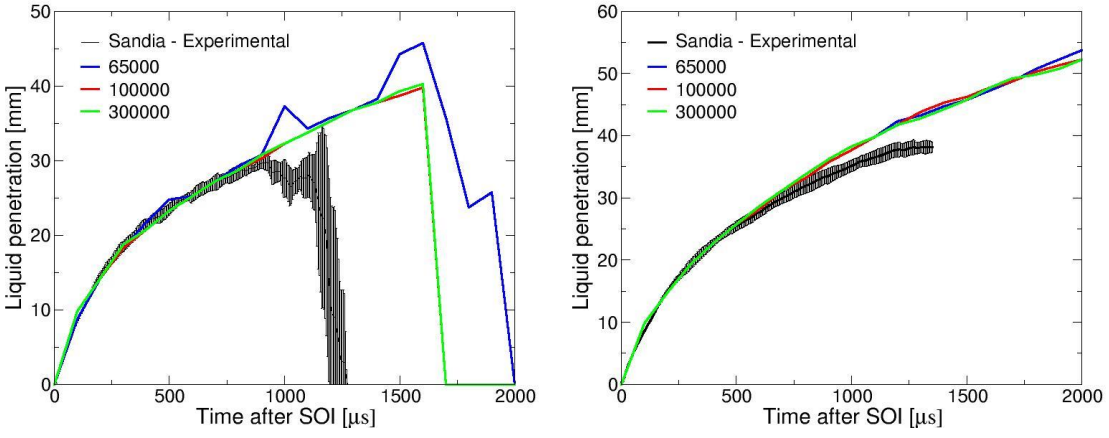


*(a)* *(b)*

***Figure 5.19 - Liquid penetration for the Pilch-Erdman model changing the number of particles injected into the system according to the two thresholds of LVF 2 $mm^3/mm^2$ (a) and 0.2 $mm^3/mm^2$ (b)***

The results for vapor penetration are very good in all the three simulations. Only for the time steps after the end of injection it is possible to notice some differences between the three simulations. In particular, the curve corresponding to the case with

300000 parcels well predicts the trend provided by experimental data for all the time steps.

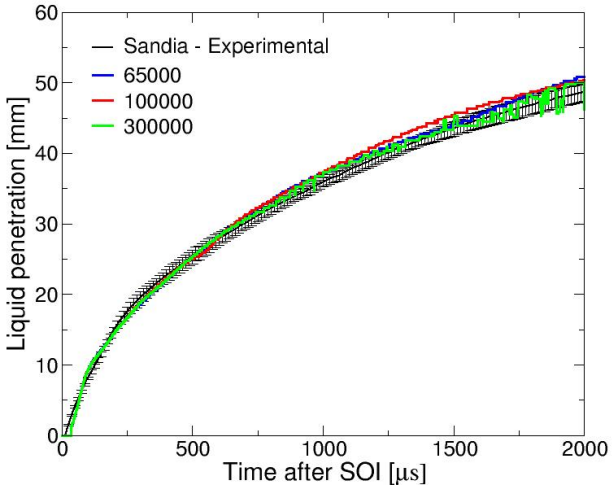


***Figure 5.20 - Vapor penetration for the Pilch-Erdman model with different numbers of parceles injected***

For all the other quantities of interest in spray G simulations there is not a significant difference among the three cases considered.

The importance of an accurate prediction of liquid and vapor penetration in spray simulations justifies the increase of the number of parcels injected from 65000 to 100000 while, at the same time, the small differences obtained when using 300000 instead of 100000 parcels suggest that a number of 100000 parcels for this setup is a good compromise between accuracy and simulation costs. The results obtained in this analysis agree with the DDM theory by which the results should converge as the number of parcels is increased. Considering that the number of parcels used is severely high, the results are very similar because the convergence is close.

### 5.3.4. The Counterbore Effect

In spray G experiments, the liquid fuel is injected in the system by a multi-hole injector. The injection point corresponds to an orifice located at the bottom of a counterbore. The resulting spray crosses the counterbore before entering inside the constant-volume vessel. Usually in CFD simulations of spray G, the Delphi injector is modelled using eight unit injectors and the counterbore geometry is neglected when the mesh is created. During previous ECN workshops, the possible effects of the counterbore on the spray characteristics has been discussed. According to the hypothesis advanced there, when a spray is injected inside a channel, the air motion generated between the spray and the channel walls has an influence on the spray characteristics that is not negligible.

Three simulations are run using the same models and constants (blob injection model, Pilch-Erdman with $B_2$ = 0.02 and 100000 parcels injected), changing only the mesh. The first simulation adopts the grid with 2 mm side cubes and the adaptive local

mesh refinement (AMR), like all the previous simulations. The third simulation (named "snappy with counterbore" for simplicity) uses a grid obtained with the meshing tool *snappyHexMesh* provided by OpenFOAM. In this case the mesh is obtained starting again from a base grid composed only by cubical elements with 2 mm sides. Then, the STL (stereolithography) file representing the detailed geometry of the injector, including also the counterbore, is introduced in the system. After that, the mesh is refined with a level of two in those regions where the presence of the spray is expected during the simulation. The purpose is to maintain as much as possible the coherence with the mesh used for the first case. Moreover, the mesh is further refined in the proximity of the counterbore with a level of six, creating cells with a characteristic length of 0.03125 mm. A surface layer with a single-cell thickness is created above the injector walls. By doing so, the counterbore (diameter of 0.388 mm) results well described by the resulting grid (Figure 5.21). While the mesh created with the AMR is modified during each time step, the one created with *snappyHexMesh* is fixed. The second simulation (named "snappy") represents an intermediate case among the two described above. It adopts a mesh created using *snappyHexMesh* with the same specifications just described for the third case, but without including the STL file in the geometry. For this case, the idea is to replicate the mesh adopted in the last case but, at the same time, the counterbore geometry results neglected like it is done in the first case. What is obtained is very similar to what it is shown in Figure 5.21 (a), with three zones having different refinement levels. The only difference is the injection zone where the geometry of the counterbore is not included into the mesh.

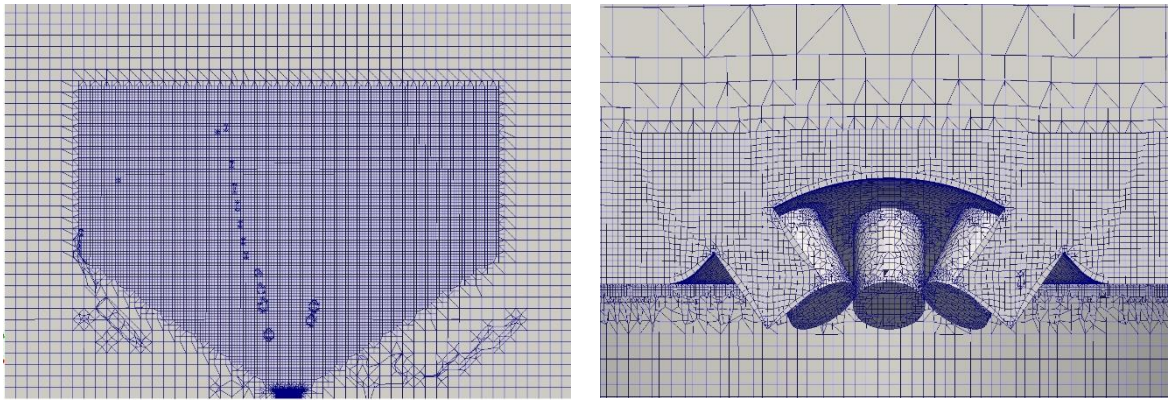

***(a)*** ***(b)***

***Figure 5.21 - Section (a) and detail of the injection zone (b) for the mesh used during the simulation with the complete description of the counterbore***

This comparison allows to highlight possible effects due to the presence of the counterbore and, at the same time, to distinguish them from the possible differences introduced while changing the mesh. The quality of the mesh is different from case to case and it can be summarized as:

- AMR: dynamic mesh; 102060 cells at the beginning and 849254 cells at the end; maximum aspect ratio: 2.073; maximum non-orthogonality: 34.26; average non-orthogonality: 5.06; max skewness: 0.38;

- snappy: fixed mesh; 1919904 cells; maximum aspect ratio: 1; maximum non-orthogonality: 25.23; average non-orthogonality: 4.64; max skewness: 0.35;
- snappy with counterbore: fixed mesh with the presence of the STL file; 1786731 cells; maximum aspect ratio: 11.43; maximum non-orthogonality: 62.77; average non-orthogonality: 5.77; max skewness: 3.05;

When the fixed mesh is adopted, the number of cells is strongly increased with a consequent increase of simulation time. The detailed description of the counterbore with the STL file reduces the mesh quality, since the geometry becomes more complex.

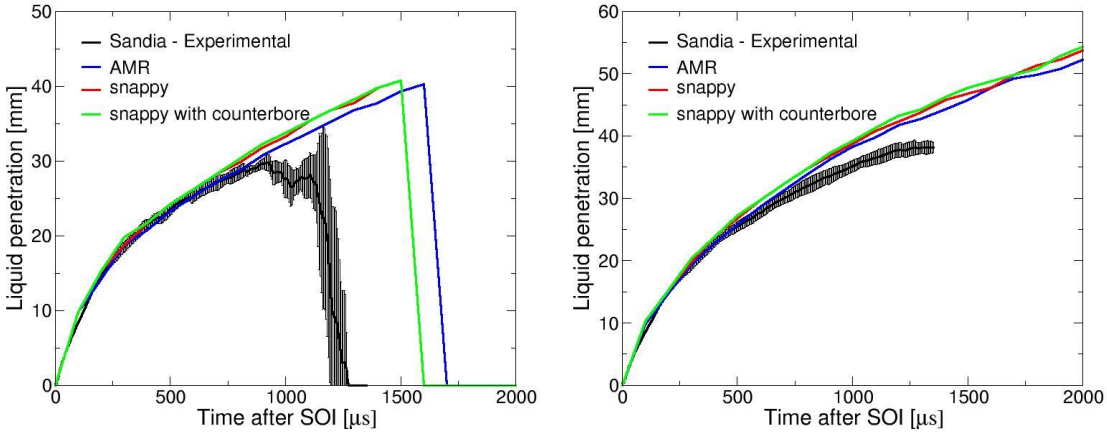


***Figure 5.22 - Liquid penetration for the Pilch-Erdman model adopting different mesh design for the investigation of the counterbore effect, according to the two thresholds values of LVF 2 $mm^3/mm^2$ (a) and 0.2 $mm^3/mm^2$ (b)***

Looking at the results obtained, the two cases built with a fixed mesh provide very similar results for all the quantities of interest. The simulation with AMR, instead, provides slightly different results for liquid penetration (Figure 5.22). Analysing the axial velocity graph (Figure 5.23), a remarkable difference is highlighted after 1.0 ms ASOI when a different mesh configuration is adopted.

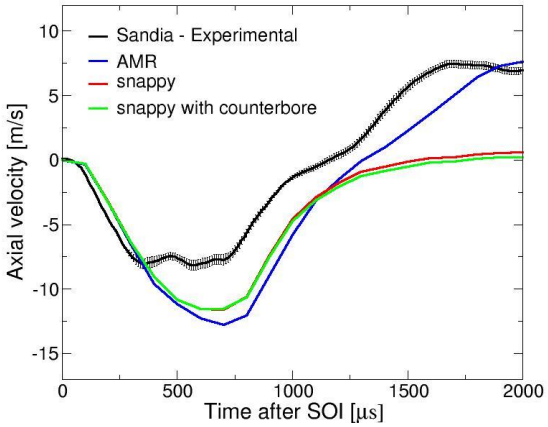


***Figure 5.23 - Axial velocity as function of time for the PE model for the counterbore effect analysis***

Since no significant differences are found between the simulations with the fixed mesh, it is possible to state that a detailed description of the counterbore geometry is not necessary. The results produced do not justify a remarkable increase of complexity in the mesh generation. Instead, the differences among the fixed mesh cases and the AMR case suggest that different mesh design provide different results. This aspect deserves more detailed analysis.

To confirm the considerations about the counterbore effect, another simulation is performed. In this case, always the same setup for models and constants is maintained. The mesh adopted is analogous to the one created using *snappyHexMesh* and the STL file. The only difference introduced with respect to that case is the modification of the counterbore length that is three times higher compared to original specifications (Figure 5.24). The purpose is to create an artificial situation where the counterbore geometry is modified to exasperate the possible effects on the spray characteristics.

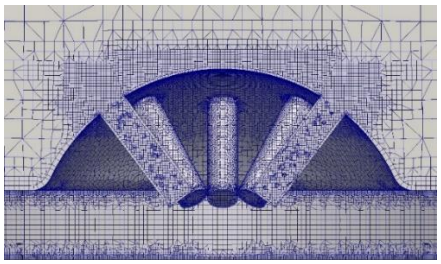

***Figure 5.24 - Detail of the mesh used for the "triple counterbore" simulation***

During the simulation some liquid parcels has been removed since they hit the counterbore walls. This does not affect the motion of the other parcels, but the results cannot be considered reliable. However, after the postprocessing, no remarkable differences are observed between this case and the other two cases adopting the fixed mesh.

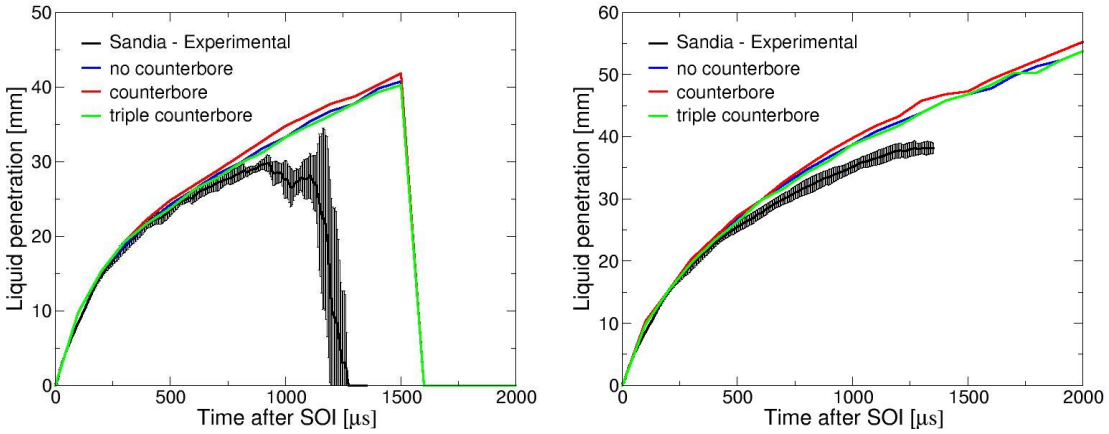


***(a)*** ***(b)***

***Figure 5.25 - Liquid penetrations for Pilch-Erdman model adopting the same grid design with different counterbore geometries***

### 5.3.5. Mesh Effect

From the previous analysis on the counterbore effect some conclusions are drawn: a detailed description of the motion inside the counterbore does not produce significant changes in the results, but the mesh structure can have significant effects. Comparing the fixed mesh, obtained with *snappyHexMesh*, with the dynamic mesh, obtained with AMR, significant differences are found in the axial velocity plot as function of time. To better understand them, the velocity field is studied. In Figure 5.26 the expected velocity field of the gas phase is represented. As it is possible to notice, during injection, gas vortexes are generated both in the region in the middle of the plumes and in the region that lies between them and the vessel walls. Once the injection is finished, these vortexes come in contact close to the sampling point considered during postprocessing, providing the complex curve represented in the axial velocity plot. The main differences between the two cases considered are highlighted once the injection is ended (after 0.8ms after SOI). The correct prediction of the behaviour of these vortexes is crucial because they determine the air entrainment that plays a very important role in the spray evolution.

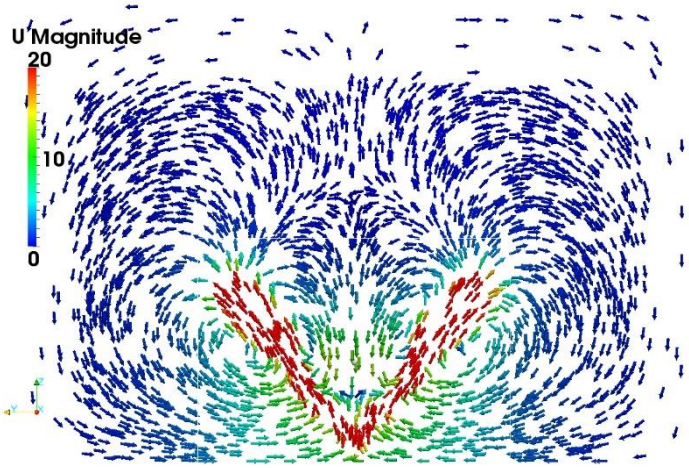


***Figure 5.26 - Expected gas velocity field. This image is obtained from the simulation adopting the "snappy cube" mesh at 0.8 ms after SOI***

The gas vortexes included between external walls and spray plumes are predicted similarly by the different meshes. Instead, a significant difference is shown for the vortexes generated in the region in-between the plumes. In both the meshes, the region where the predicted vortexes are similar, the refinement is the same: they both have cells with characteristic length of 2 mm. Instead the inner region, where the simulations differ, is refined with 0.5 mm cells for the fixed mesh and with 2 mm cells for the automatically refined mesh. This suggests that a different refinement of the mesh produces different velocity field predictions.

Another simulation is performed to prove the sensitivity of the velocity predictions to the mesh refinement. This case adopts the same setup for models and constants used in the previous paragraph. The mesh used for this case (Figure 5.27) is fixed and it is generated with *sanppyHexMesh*. The whole vessel is meshed with cubic cells with 2 mm sides and the region where it is expected the presence of the spray is refined with a level

of refinement equals to two (creating cells with a characteristic length of 0.5 mm). In this case the refined region includes also the zones of the system in the middle of the plumes and the zones that lies between the plume and the walls. The resulting mesh present a refinement region with a cubic shape: for this reason, this case is named “snappy cube” to distinguish it from the previous mesh created with the same meshing tool which has a refined region with the shape of a cone (“snappy cone”).

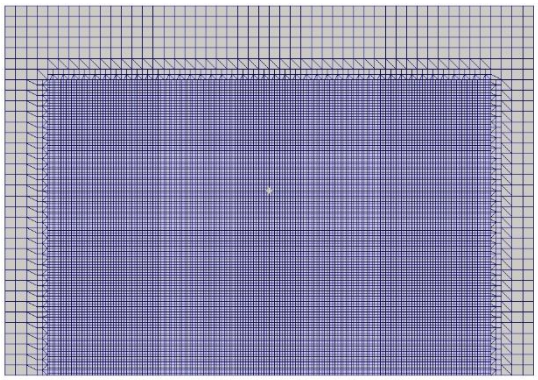

***Figure 5.27 - Section of the mesh used for the "snappy cube" simulation***

Comparing these last two cases with fixed mesh (“snappy cone” and “snappy cube”) and the case with the AMR, the main differences are obtained in the axial velocity graph (Figure 5.28), especially after the end of injection (8 ms after SOI). By analysing the velocity field for the “snappy cube” case, like it has been done for the other case, the hypothesis by which the prediction of velocity depends on the local grid refinement seems to be confirmed. The vortexes in-between the plumes are very similar to the ones predicted by the “snappy cone” simulation, while the vortexes between plumes and walls are more intense than the ones predicted in the other two cases. From this comparison, the following tendency can be noted: the velocity of the vortexes generated by the gas phase are underestimated where the grid is less refined. This is because a finer grid allows to better estimates the velocity and pressure gradients in the momentum and continuity equations according to the theory of the finite volume method.

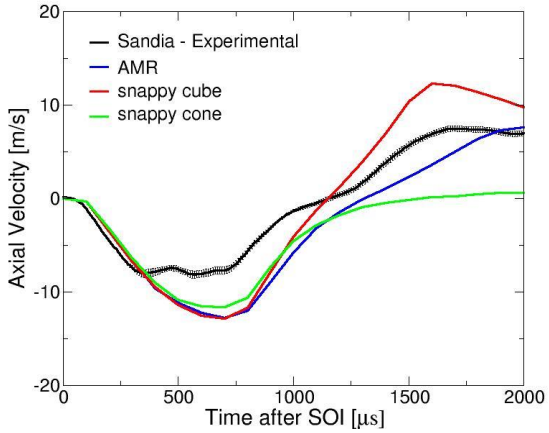


***Figure 5.28 - Mesh effects on the axial velocity plot for the PE model***

These differences affect also the liquid penetration (Figure 5.29). More evident effects are highlighted for the first LVF threshold (a). The other postprocessed quantities, including also the vapor penetration, do not highlight such significant differences.

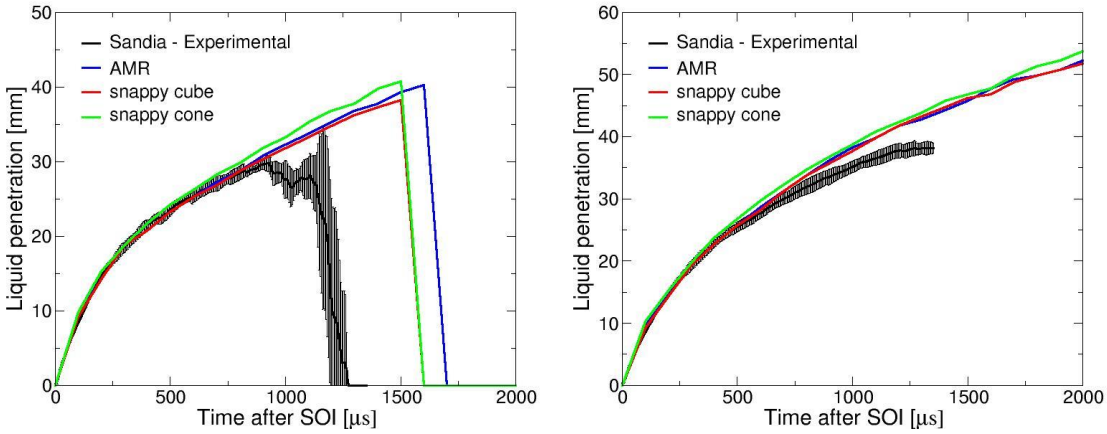


***Figure 5.29 - Mesh effects on the liquid penetration values for the PE model according to the two thresholds of LVF 2 mm³/mm² (a) and 0. 2 mm³/mm² (b)***

This analysis show how the mesh refinement strongly affects the result obtained form the spray simualtion.

According to the finite volume method the "snappy cube" mesh is the best among the cases compared in this analysis since it is most refined one. The results observed here suggest using this mesh structure. As drawback, this involves an important increase of the number of cells in the mesh and consequently an increase of computational costs.

### 5.3.6. Final Considerations on the Pilch-Erdman Model

Whatever the mesh adopted is, the Pilch-Erdman model with this set of constants provides some results that are not satisfactory. First, looking at the morphology (Figure 5.30), the spray plumes generated by this model exhibits a tip composed by liquid drops that penetrate in the vessel without evaporating. This is very similar to what has been observed with KHRT model, but in this situation the problem seems to be worse.

To confirm what is observed in the spray morphology, liquid and vapor penetrations are plotted on the same graph both for Sandia experimental data and for the Pilch-Erdman model (Figure 5.31). In the plot obtained with experimental data (a), vapor and liquid penetration curves tend to detach the one from the others as the time passes with the vapor curve that always lies above the liquid ones. Instead, in the plot obtained from the Pilch-Erdman model this tendency is not clearly shown; in particular, the liquid penetration curve with the LVF threshold of 0.2 $mm^3/mm^2$ lies above the vapor penetration one after the end of injection.

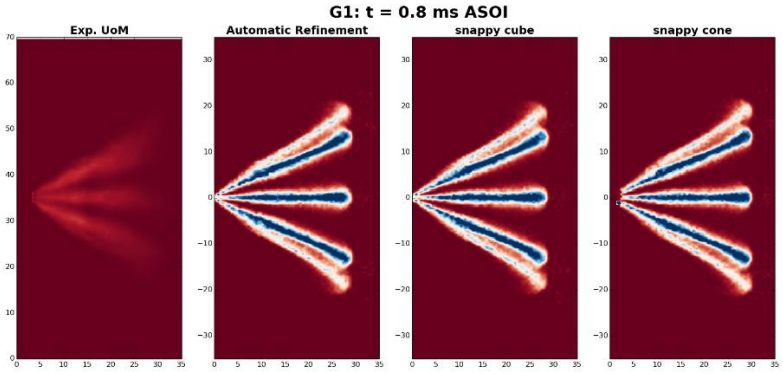


***Figure 5.30 - Spray morphology for Pilch-Erdman model with different mesh design***

The graph of experimental data suggests that initially the vapor is dragged by the liquid that is injected at high velocity into the system providing curves that are quite overlapped close the start of injection. Here the vapor penetration is the result of the fuel that evaporates from the tip of the spray plumes. While, as time passes, the curves of liquid and vapor penetration are slowly detaching. In these time steps, the vapor penetration is provided not only by the evaporation of the plumes tips but there is also a contribution given by fuel vapor diffusion and gas motion inside the system. According to the data provided by Pilch-Erdman model, after the end of injection, the liquid penetration becomes greater than the vapor penetration meaning that some liquid drops penetrate deeper than the fuel vapor carried by the air motion.

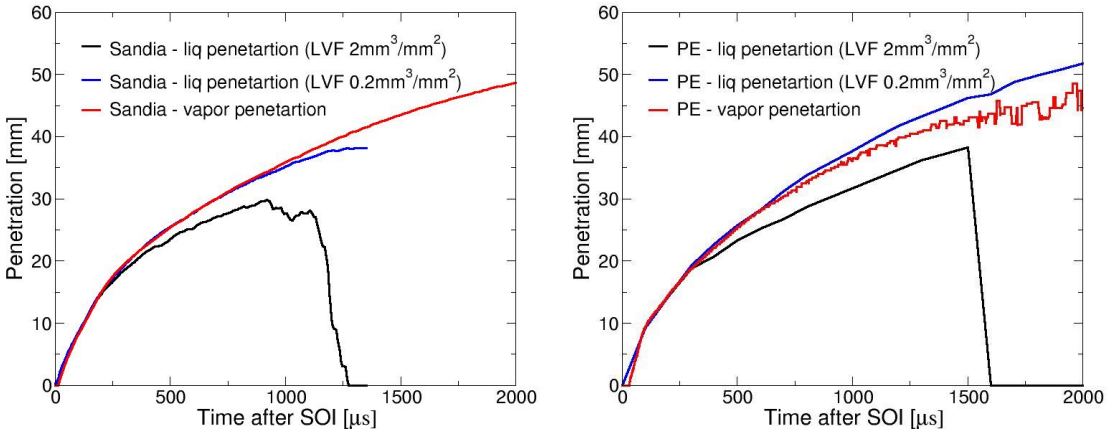


***(a)*** ***(b)***

***Figure 5.31 - Liquid and vapor penetration values for experimental data by Sandia (a) and for the PE model (b)***

Finally, by plotting on the same graph the mass of fuel in the vapor phase as function of time for KHRT and PE models, it is clear that Pilch-Erdman model predicts a spray which evaporates slowly. In Figure 5.32 the black line represents the total mass of

fuel present in the system, both in liquid and in gas phase. No experimental data are available for these values.

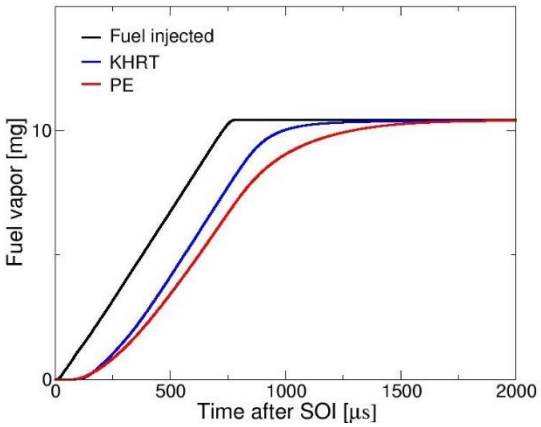


***Figure 5.32 - Mass of fuel in vapor phase as function of time for PE and KHRTPE model***

The Pilch-Erdman model proposes a breakup mechanism by which the child drops are sheared off the surface of the parent drop. Similarly to KH mechanism, the resulting spray is composed by some large droplets remaining from the original parent droplets. They have a large volume to surface ratio and they hardly evaporate. The plume tip that is observed in the spray morphology is composed by these large droplets.

Since this model is based on experimental observations, it provides good penetration values with a suitable calibration (only two adjustable constants are proposed by this model), but it does not describe completely the physics of the breakup observed in experiments. For this reason, it is not suitable for a detailed investigation on spray problems.

## 5.4. KHRTPE MODEL: CALIBRATION AND VALIDATION

Among the weaknesses highlighted before, the Pilch-Erdman model presents some strengths and advantages. That is why the ICE group in Politecnico has decided to develop and implement the KHRTPE hybrid model in the LibICE library. The KHRTPE model tries to combine the Pilch-Erdman with the KHRT to create a new secondary breakup model able to better describe all the possible breakup mechanisms observed in a spray.

This model has not been studied in detail yet, since it has been developed only recently, after the studies performed on the Pilch-Erdman model. For this reason, no information about it are present in the literature. The objective for this part of the work is to assess the performances provided by this model and to identify its strengths and weaknesses.

As first, a quick calibration of this model is performed to find a set of constants that provides results as close as possible to experimental data. The constants of KHRTPE model are the same proposed by the KHRT model plus the ones proposed by the Pilch-Erdman model. To avoid misunderstandings, the constants proposed by the Pilch-Erdman model are renamed $B_{1,PE}$ and $B_{2,PE}$ (in the original model they are named respectively $B_1$

and $B_2$). Instead the same nomenclature is maintained for the constants coming from the KHRT model.

Once the set of constants has been calibrated, the results provided by this model are compared to the ones provided by KHRT and Pilch-Erdman to assess its performances. When strengths and weaknesses of each model are identified, the better performing one can be determined.

### 5.4.1. Calibration of the Constant $B_1$

The constant $B_1$ proposed by the KHRTPE model is the same that appears in the KH model inside equation (3.59). It must be calibrated for each case to fit experimental data. According to [20] its value usually ranges from 1.73 and 60. As $B_1$is increased, the characteristic breakup time $\tau_{BU}$ increases too. As consequence, the breakup rate according to KH mechanism is reduced. The droplets SMD are greater and the penetration values are increased.

The simulations performed in this analysis adopt the same dynamic mesh proposed by Politecnico and described while discussing about the numerical state of art. This choice is justified by the fact that the objective of this analysis is a quick calibration of the constants and not a detailed assessment of the model performances. The adoption of a mesh with AMR allows to save computational time with respect to a fixed mesh. This is fundamental since a lot of attempts with different $B_1$ values are forecast. The accuracy of the solution results lower as previously observed, but the differences that are shown while adopting a fixed mesh rather than a dynamic mesh are smaller than the ones expected while changing $B_1$ during this calibration.

The initial set of constants is built up by adopting the values assumed by the corresponding constants after the calibration of the KHRT and Pilch-Erdman models. Since there are no references regarding the values assumed by the constants in the specific case of KHRTPE model, this could be a good starting point. The first value used in this analysis for $B_1$ is 25 (close to the value of 28 suggested during the last ECN workshop for KHRT model). Then other two attempts are done using a doubled (50) and a halved (12) value for this constant. Finally, exploiting the result obtained from these simulations, a value of 40 is tried to better fit experimental data.

This is a rough calibration and the difference among the results can be easily identified. The choice of the best value for $B_1$ can be done simply by looking at the penetration plots. Figure 5.33 shows how the liquid penetration increases as $B_1$ becomes greater according to what is expected from the literature. The curves obtained imposing $B_1$ = 40 are the ones that approximate better the experimental behaviour.

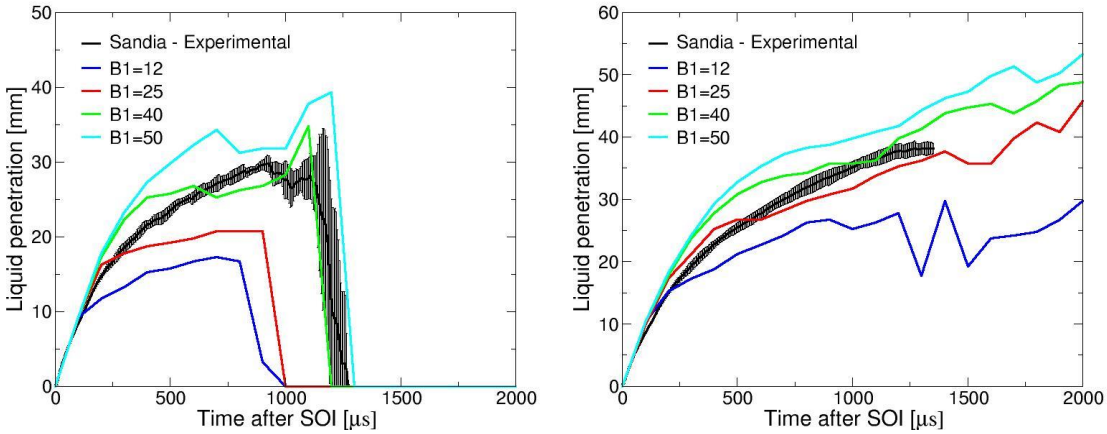


***Figure 5.33 - Liquid penetration for the KHRTPE model with different values of $B_1$ according to the two thresholds of LVF 2 mm³/mm² (a) and 0. 2 mm³/mm² (b)***

Also the vapor penetration graph (Figure 5.34) shows the same trend observed for liquid penetration and the curve obtained with $B_1 = 40$ is again the closest to experimental data among the ones studied here.

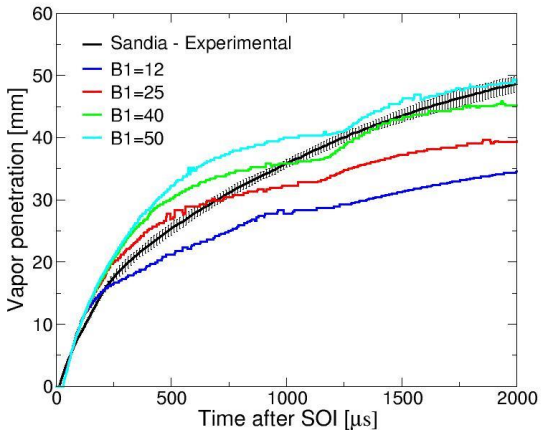


***Figure 5.34 - Vapor penetration for the KHRTPE model with different values of B1***

The other postprocessed quantities confirm what has already been deduced from the penetration plots. As already declared, since this is a first attempt to calibrate the constants of KHRTPE model, the results are not analysed in detail and the attention is focused only on finding a value for $B_1$ that provide meaningful results. After this analysis, the best value that can be attributed to $B_1$ among the ones tested is 40 and it will be used from now on for KHRTPE model.

### 5.4.2. Calibration of the Constant $C_{BU}$

The constant $C_{BU}$ is introduced in the KHRT model by equation (3.64) and it allows to compute the liquid core length. In the KHRTPE model, this constant has the same

function. The liquid core length delimits the region where the different breakup mechanisms are applied. If the distance of a parcel from the injection point is smaller than the core length, only KH and Pilch-Erdman mechanisms are possible; while for greater distance values only KH and RT mechanisms can be applied.

Not much is known about the liquid core and its characteristics, since it is difficult to find an experimental setup able to observe and measure it. However, its existence is assumed as a well-established fact. The work proposed by Faeth [17] provides a comprehensive description of spray and its properties. According to what is proposed in this publication, the liquid core length can be described through an expression that can be easily rewritten to obtain the same formulation of (3.64):

$$\frac{L_c}{d_f} = C_{BU}\sqrt{\frac{\rho_l}{\rho_g}} \approx 200 - 500 \tag{5.2}$$

The range proposed by Faeth is valid for typical sprays at atmospheric pressure, but the literature does not guarantee that these values are reasonable also for spray G conditions. Anyway, they are considered overestimated, since with such great liquid core lengths, the observations and measurements should not be so difficult. To confirm this fact, if a $C_{BU}$ that satisfy this relation is adopted, the resulting liquid core length will be approximately equal to the spray penetration in spray G. This is not consistent with what is observed in experiments, since an intact liquid core is not visible inside the spray plumes along their whole length.

The firsts evaluations performed by the ICE group on KHRTPE, while developing this model, suggest the use of $C_{BU} = 0.75$ corresponding to a calculated liquid core length of 1.6581 mm. In this analysis they are compared three different cases in which $C_{BU}$ assumes different values (respectively 0.375, 0.75 and 2) while all the other parameters are kept constant. The dynamic mesh with AMR is used for the same reasons that are explained for the calibration of $B_1$. The liquid core lengths obtained from the values of $C_{BU}$ adopted here are respectively 0.82905 mm, 1.6581 mm and 4.4216 mm.

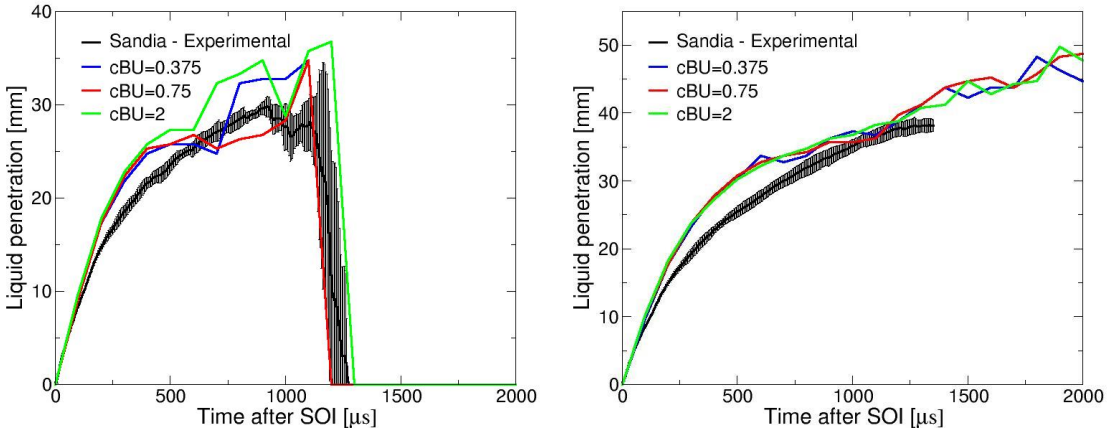


***Figure 5.35 - Liquid penetration for the KHRTPE model with different values of $C_{BU}$ according to the two thresholds of LVF 2 mm³/mm² (a) and 0. 2 mm³/mm² (b)***

Studying the liquid penetration (Figure 5.35), the three cases provide very similar performances and it not possible to clearly identify a precise trend when $C_{BU}$ is changed.

The vapor penetration (Figure 5.36) is again very similar in all the cases considered and no evident trends can be observed from the plot. The curve corresponding to $C_{BU}$ equal to 2 does not exhibit a discontinuity after 1.0 ms like the other ones. This is more in agreement with experimental data that do not have a discontinuity.

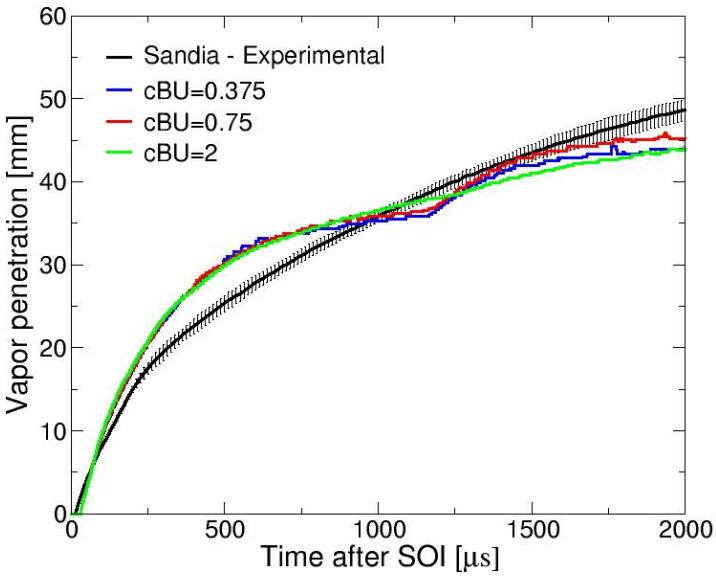


***Figure 5.36 - Vapor penetration for the KHRTPE model with different values of $C_{BU}$***

The plot that reports the liquid mass density as function of the radial position (Figure 5.37) could give more precise information, since the sampling point is located very close to the expected liquid core (2 mm above the injection point). Also this graph does not provide significant indications. At the end, a $C_{BU}$ equal to 2 is chosen since it better reproduces the vapor penetration data.

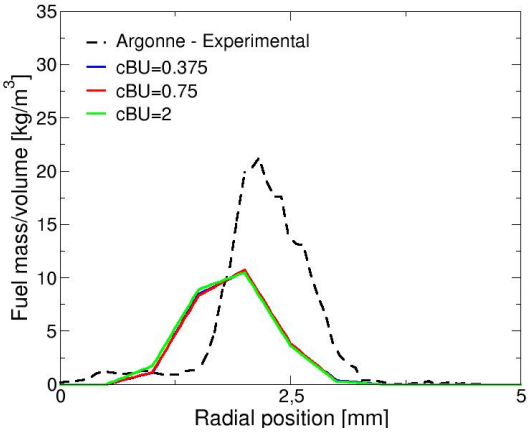


***Figure 5.37 - Radial distribution of density for KHRTPE model adopting different $C_{BU}$ sampled at 0.6ms after SOI***

### 5.4.3. Final Considerations on KHRTPE Model

The calibration of the constants of the KHRTPE model provides a setup that is useful for a first assessment of performance of this model. In this analysis the results that it provides are compared to experimental data and to the results provided by the Pilch-Erdman and the KHRT models. The objective is to discover if the performances of KHRTPE are good enough to justify a deeper investigation. On the contrary, if its results are significantly worse than the ones provided by other models, further analysis on this model are not worth to be performed.

This comparison includes three numerical simulations for spray G adopting three different secondary breakup models. The first case reported adopts the configuration proposed by Politecnico that is considered the numerical state of art for spray G with KHRT model. The second case adopts the PE model with the configuration called "snappy cube" defined while studying the mesh effects on Pilch-Erdman model, since it has been shown to be the better performer among all the configurations that use this model. The last case adopts the KHRTPE model with the set of constants obtained from the previous analysis. To be more accurate the mesh chosen for the third simulation is the same fixed mesh adopted for the second case.

The liquid penetration values plotted in Figure 5.38 are very close to experimental measurements for KHRT and KHRTPE models. The curves produced by the KHRTPE models are the only ones that does not provide a precise penetration prediction for time values close to the start of injection.

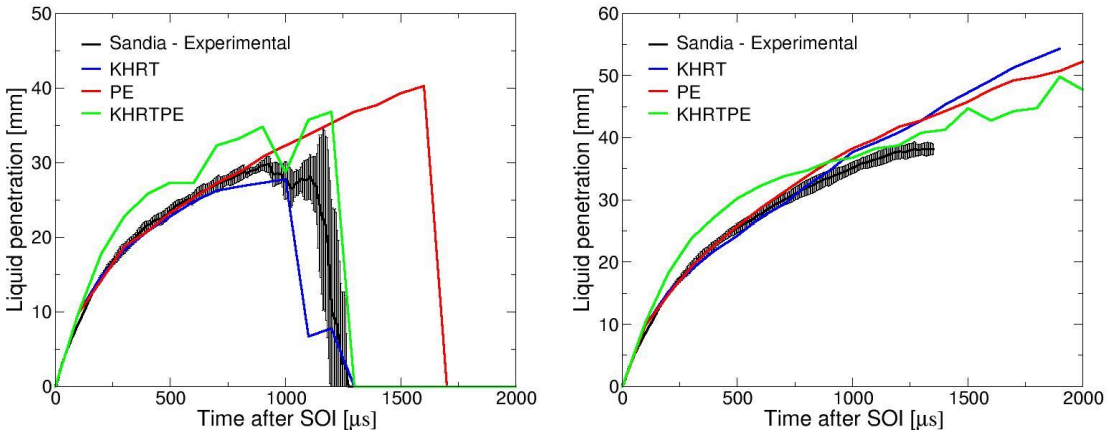


*(a)* *(b)*

***Figure 5.38 - Liquid penetration for the KHRT, PE and KHRTPE models according to the two thresholds of LVF 2 $mm^3/mm^2$ (a) and 0. 2 $mm^3/mm^2$ (b)***

Very similar considerations can be obtained by analysing the vapor penetration (Figure 5.39). The curve corresponding to KHRTPE model tends to overestimate the penetration even for low time values while the KHRT curve departs from experimental data only after the injection process is ended.

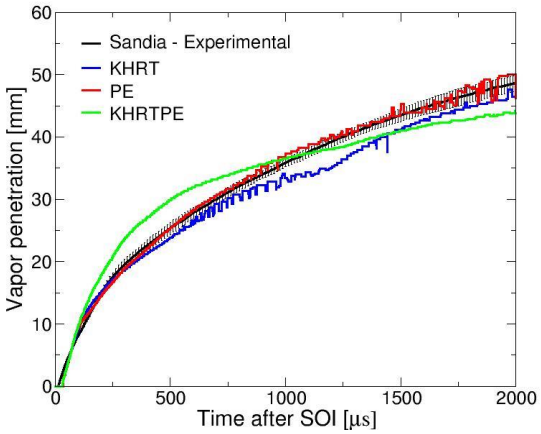


***Figure 5.39 - Vapor penetration for the KHRT, PE and KHRTPE*** models

The graph that represent the mass of fuel in vapor phase as function of time (Figure 5.40) shows how the Pilch-Erdman model predicts a very poor fuel evaporation compared to the other models. Instead, the KHRTPE and KHRT models predicts similar fuel evaporation.

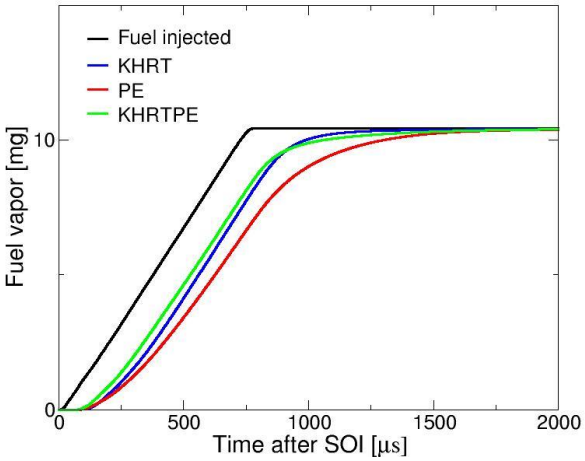


***Figure 5.40 - Mass of fuel in vapor phase as function of time for the KHRT, PE and KHRTPE models***

By plotting on the same graph liquid and vapor penetrations values (Figure 5.41), some useful observations can be done. The plot corresponding to the KHRTPE model (b) has a very similar behaviour compared to the analogous graph obtained while discussing the Pilch-Erdman model. Also in this case, the breakup model predicts a spray with a tip composed by liquid drops that penetrate in the vessel with poor evaporation.

The behaviour of KHRTPE data observed in Figure 5.41 is not consistent with experimental measurements and with the physics of the problem. KHRTPE and PE models, from this point of view, do not provide an improvement with respect to KHRT model. Finally, considering the observations about the overpredictions of penetrations provided by KHRTPE and remembering the importance of these values, there is no reason to further analyse this model since KHRT provides better performances.

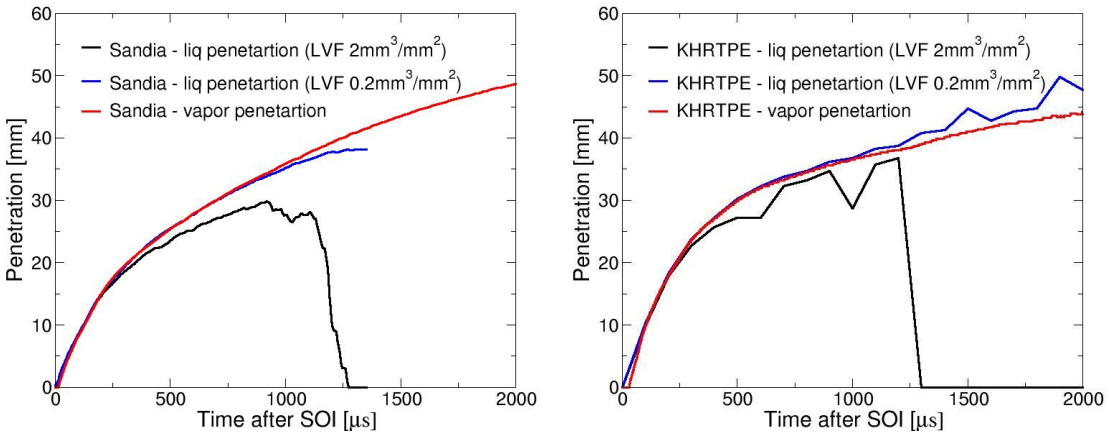


***(a)*** ***(b)***

***Figure 5.41 - Liquid and vapor penetration values for experimental data by Sandia (a) and for the KHRTPE model (b)***

To summarize, the KHRTPE model has the same weakness provided by the PE model. Also in this case the plume tips are composed by liquid drops that evaporate very slowly. The parameters that must be calibrated are numerous and the calibration process is not so simple like in the case of PE model. Moreover, the penetration values provided by the KHRTPE model are not so accurate such as the ones provided by the PE model. This model results not suitable for spray simulations.

# 6. KHRT MODEL: EFFECTS OF SUB-MODELS AND MESH DEPENDENCY OF THE RESULTS

In chapter 5, the performances of different secondary breakup models have been evaluated comparing them with the setup proposed by Politecnico di Milano during the last ECN workshop. After this analysis, the KHRT model still results the most reliable and the better performing one. For this reason, it is adopted as secondary breakup model during all this analysis.

The objective for this analysis is to evaluate the effects of sub-models and mesh structure on the results of spray G simulations, once the secondary breakup model is fixed. At the same time, possible improvements of the reference setup proposed by Politecnico are evaluated.

## 6.1. MESH EFFECTS ON KHRT BREAKUP MODEL

While studying the Pilch-Erdman and the KHRTPE models, it has been proved how the results are influenced by the mesh. In particular, some differences in the simulations while adopting a fixed mesh instead of a dynamic mesh with AMR have been highlighted. A similar analysis can be applied also to the KHRT model, trying to understand the influence that the grid structure plays on the results provided by this model. Considering that the differences among the meshes adopted are observed mainly in the gas motion, conclusions similar to the ones obtained from the previous analysis are expected.

In this investigation, all the cases adopt the same numerical setup that was described as the reference one. Huh-Gosman model is used to describe the spray atomization and the KHRT model is used for secondary breakup. Two different simulations are performed with different meshes and then their results are compared. The first case adopts the dynamic mesh created with AMR (this case is identical to the one described in the numerical state of art), the second one adopts the “snappy cube” mesh created with *snappyHexMesh* and already used in the analogous analysis on PE model.

Since this model has been calibrated before, to be more rigorous, in the penetration graphs, also the experimental values obtained by the University of Melbourne (UM) are plotted with their corresponding error bars. According to the observations and experiences made during previous ECN workshops, they are considered not so reliable such as the ones provided by Sandia, that remain the reference for this work.

The liquid penetration plots are very close to experimental measurements in both the cases (Figure 6.1). The fixed mesh tends to provide slightly smaller values than the AMR mesh as time passes. While during the injection process, the corresponding curves are quite overlapped. Similar considerations can be made also for the vapor penetration.

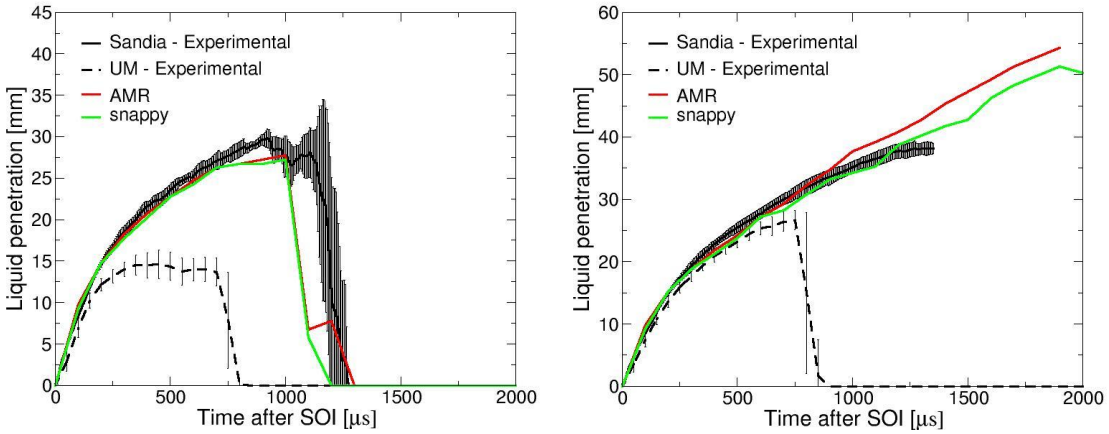


***Figure 6.1 - Liquid penetration for the KHRT model according to the two thresholds of LVF 2 $mm^3/mm^2$ (a) and 0. 2 $mm^3/mm^2$ (b) obtained from different meshes***

The most significant differences are shown in the axial velocity graph (Figure 6.2), as it is expected. Also with the KHRT model, after the end of injection, the curves corresponding to different meshes provides very different results. This can be explained by looking at the gas vortexes generated by the spray injection. The fixed mesh predicts vortexes with higher intensity and magnitude, since it is more refined in those regions where they develop. The interaction among these vortexes is the responsible of the trend shown in Figure 6.2. The curve provided by the fixed mesh produces a positive peak of velocity which is even worse than the one produced by then AMR mesh. In this situation, the weakness already underlined for the KHRT model in the state of art are further emphasized.

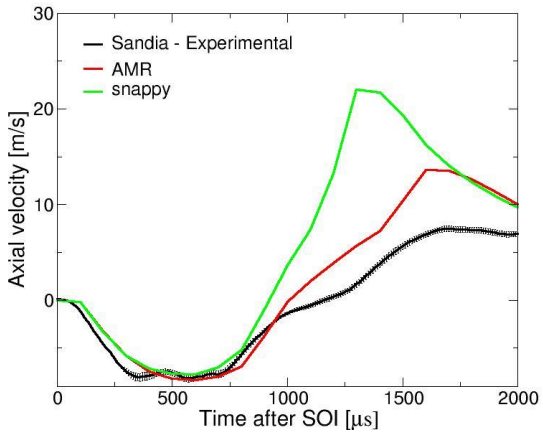


***Figure 6.2 - Axial velocity as function of time provided by the KHRT model on different meshes***

From this analysis some conclusions can be drawn: first, the mesh sensitivity of KHRT model results is similar to the one of PE model; moreover, a refinement of the mesh worsens the results.

## 6.2. MODEL CALIBRATION

The results obtained with the KHRT applied on the fixed mesh deserve a deeper analysis. Since the constants present in this model have been calibrated adopting the dynamic mesh, they need to be adjusted to improve the results obtained with a fixed grid. This further calibration of the breakup model is useful to understand the sensitivity of the results to the KHRT model constants.

### 6.2.1. $B_1$ Calibration

The first constant analysed is $B_1$, already considered in the calibration of the KHRTPE model. It appears in the KH model description inside equation (3.59). As previously mentioned, its value usually ranges from 1.73 and 60. When $B_1$is increased, the characteristic breakup time $\tau_{BU}$ increases, reducing also the breakup rate according to KH mechanism. As result, the droplets are broken into smaller ones slowly and the spray penetrates deeper in the inert gas.

Two simulations are compared adopting two different values for $B_1$: the first uses the value suggested by the reference conditions that is 28, while the second uses a value of 34. No other values are tried since, as it is possible to notice, the results obtained with these two simulations can be considered satisfactory.

The liquid penetration plots (Figure 6.3) provide results coherent to what is expected: as $B_1$ increases, the liquid penetration values become greater. The curve obtained when $B_1$ is equal to 34 predicts very well the Sandia experimental measurements for both the threshold values of LVF.

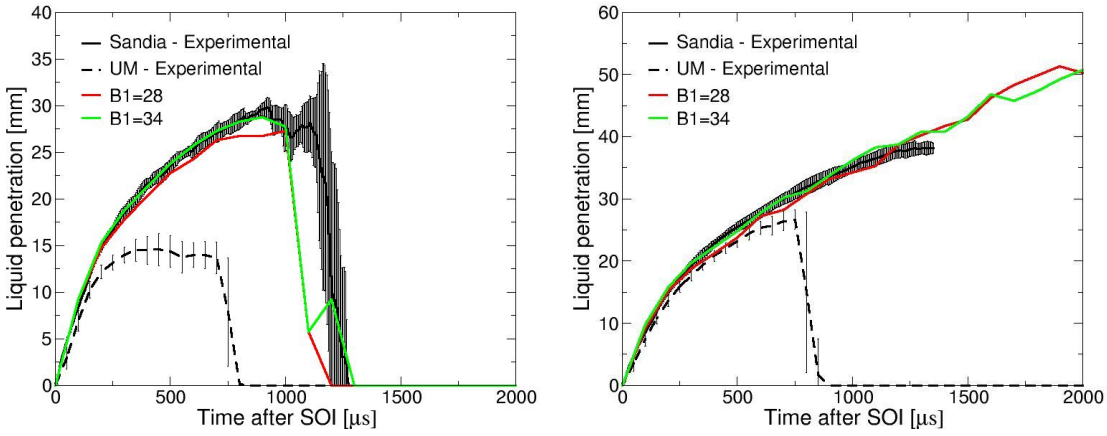


***Figure 6.3 - Liquid penetration for the KHRT model according to the two thresholds of LVF 2 mm³/mm² (a) and 0. 2 mm³/mm² (b) obtained with different $B_1$ values***

For the vapor penetration plot similar considerations be done. The radial distribution graph for the SMD gives another confirmation regarding what it is deduced from the theoretical description of the KHRT model. The droplets observed are bigger if the $B_1$ value increases. Figure 6.4 reports an example of the radial distribution of SMD;

when $B_1$ = 34 the diameters provided by the simulations are greater and the corresponding plot profile is closer to the curve that describes the experimental data with respect the case where $B_1$ = 28. The prediction of SMD significantly smaller than experimental measurements is one of the weak points of the KHRT model. By adopting greater $B_1$ values, this situation is improved.

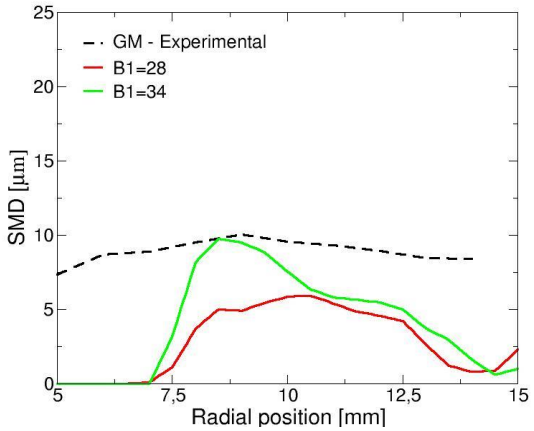


***Figure 6.4 - Radial distribution of SMD for different $B_1$ values evaluated at 0.6 ms ASOI***

The other postprocessed quantities do not show significant variations among the two cases considered. In the axial velocity graph, there are not remarkable differences and the velocity peak remains quite the same for both the simulations compared here.

The penetrations values that it provides and the improvements regarding the SMD predictions, that are one of the KHRT weaknesses, suggest the use of a $B_1$ value equals to 34.

### 6.2.2. $C_{RT}$ Calibration

The second constant considered is $C_{RT}$ (it is common to find it implemented as $cRT$ in CFD codes). It appears inside equation (3.62) for the RT model and it is an adjustable constant that is used to calculate $\Lambda$, the characteristic length of the surface waves with the highest grow rate. According to the breakup mechanism proposed by the RT model, $\Lambda$ is also equal to the diameter of the new child parcels. If the value of $C_{RT}$ is increased, this characteristic length increases too and bigger child drops are generated.

To evaluate its effects, three simulations are compared adopting different values of $C_{RT}$. The first value of 0.08 is the one suggested by the ECN6, while the other two tested values are 0.04 and 0.16. The liquid penetration graphs (Figure 6.5) show how the penetration values tend to grow as $C_{RT}$ is increased. The same can be observed for vapor penetration. This can be explained as follow: if $C_{RT}$ assumes a greater value, the child droplets resulting from RT breakup are bigger. These bigger droplets are hardly slowed down by the gas phase and they can penetrate deeper in the vessel.

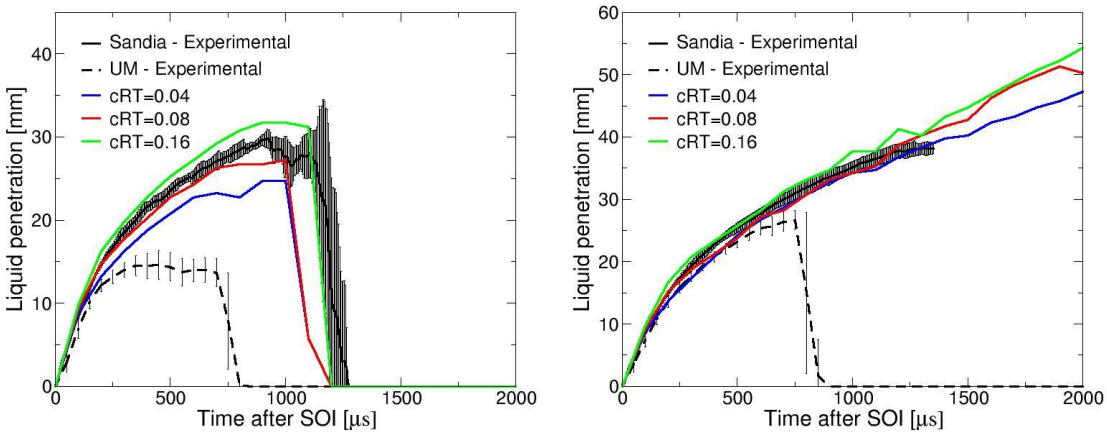


***Figure 6.5 - Liquid penetration for the KHRT model according to the two thresholds of LVF 2 $mm^3/mm^2$ (a) and 0. 2 $mm^3/mm^2$ (b) obtained with different $C_{RT}$ values***

The $SMD$ radial profile confirms that greater droplets are found in the spray if the $C_{RT}$ value is increased. Analysing the simulation performed in this comparison, the case which adopts $C_{RT}$ = 0.16 provides $SMD$ profiles that exhibits an irregular profile with very high peaks (Figure 6.6). This is not coherent with experimental data that provides a more regular profile. This fact suggests that adopting too great values of $C_{RT}$, the KHRT model provides a spray where the drops are not broken down homogeneously and some big liquid drops survive.

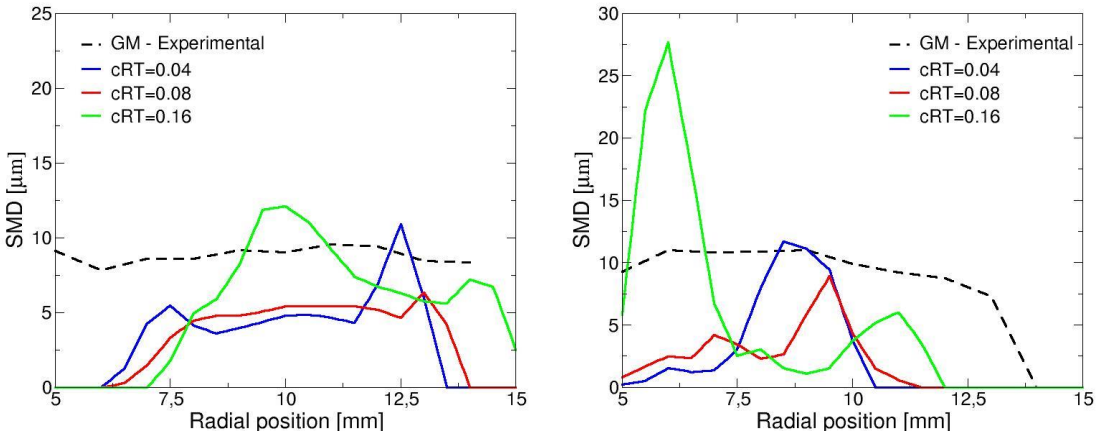


***Figure 6.6 - Radial distribution of SMD for different $C_{RT}$ values evaluated at 0.3 ms (a) and 1.2 ms (b) after SOI***

The presence of some droplets bigger than the ones experimentally observed could provide the same situation that has been noticed while using Pilch-Erdman and KHRTPE models. In such extreme conditions, also for KHRT model, it is possible to have a vapor phase that penetrates slower than the liquid phase.

Between the values of $C_{RT}$ compared, the best performing one is 0.08, since it provides good penetrations curve and regular $SMD$ profiles (even if the $SMD$ values remains underestimated).

### 6.2.3. Spray Angle Calibration

In the numerical setup proposed by Politecnico di Milano during ECN workshops, the spray opening angle $\varphi$ is imposed to be equal to a constant value of 16.5°. The Huh-Gosman atomization model is able to provide a prediction for $\varphi$, but, since reliable experimental measurements are available, a constant opening angle can be adopted exploiting these results. This choice allows to save computational efforts and at the same time to obtain a simulated spray that is consistent with experimental observations.

In the results presentation of ECN6 [3], the setups of the different contributors to spray G simulations are presented. All of them adopt a constant $\varphi$ with very similar values, since the experimental results from which they are obtained are the same.

In this analysis, different simulations are compared, changing only the spray opening angle. The values chosen for $\varphi$ are 15°, 16.5° and 18°. Greater or smaller values are not considered since they would not be consistent with experimental observations. The expectations are to obtain thinner plumes and higher penetration values for smaller angles; while for greater angles, the plumes are expected to be wider and the penetrations to be lower.

The liquid penetration plots confirm what is expected (Figure 6.7 -Figure 6.7). The simulations effectively provide higher penetrations if the spray angle is reduced.

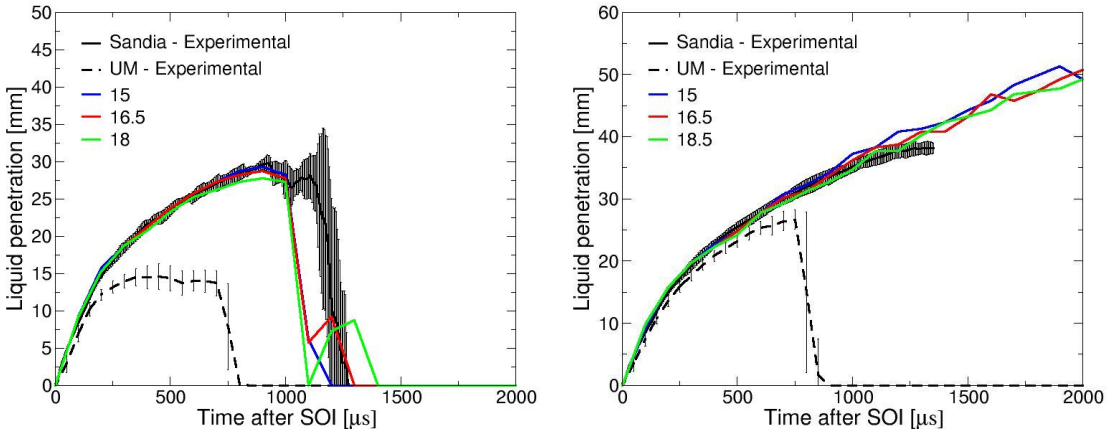


***Figure 6.7 - Liquid penetration for the KHRT model according to the two thresholds of LVF 2 $mm^3/mm^2$ (a) and 0. 2 $mm^3/mm^2$ (b) obtained with different spray opening angles***

Also the vapor penetration and the other postprocessed quantities agree with the expectations. Looking at radial distribution of the liquid velocity (Figure 6.8), it is possible to notice how the peaks of velocity are reduced and the curves are spread over a larger range of radial positions as the opening angle is increased.

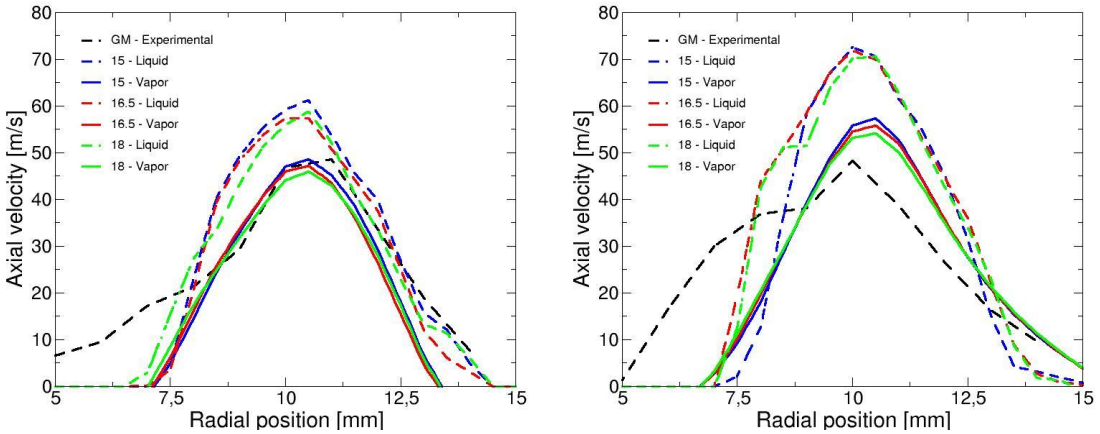


***Figure 6.8 - Radial distribution of liquid velocity for different spray opening angles evaluated at 0.3 ms (a) and 0.6 ms (b) after SOI***

The results obtained while changing the opening angle are very similar since $\varphi$ is varied only by 3° (from the smaller value to the greater one). However, the range of possible values for the spray opening angles is very narrow to achieve a good agreement between experimental and computed data.

## 6.3. TURBULENCE MODEL

The discrepancies among experiments and simulations observed for the axial velocity graph of Figure 6.2 are still present after the constant calibration. The KHRT model provides always a positive peak in this graph, that is not consistent with experimental data, whatever the constants adopted are. From the results presented during the previous ECN workshop, other turbulence models are considered and investigated, trying to understand the possible origins of this problem.

Most of the ECN contributors agree on the adoption of the standard $k$-$\varepsilon$ model with $C_{1\varepsilon}$ = 1.5 as suggested for spray simulations. The KAUST (King Abdullah University of Science and Technology) instead uses the RNG $k$-$\varepsilon$ model. The idea is to verify if this model applied on the numerical configuration with KHRT model and the fixed mesh improves the results.

The RNG $k$-$\varepsilon$ model [26] renormalizes the Navier-Stokes equations using the RNG methods (Re-Normalization Group) to obtain modified transport equations for $k$ and $\varepsilon$, with respect to the ones given by (3.25) and (3.26). Exploiting mathematical techniques, it attempts to account for the effect of different scales of motion while computing $\mu_t$; instead, the standard $k$-$\varepsilon$ model accounts only the effect of a single turbulence length scale. The RNG model provides improved results for modelling rotating flows but no improvements are proved for the predictions of vortex evolution with respect to the standard $k$-$\varepsilon$ model. Moreover, the RNG $k$-$\varepsilon$ model is considered less robust than the standard $k$-$\varepsilon$. In CFD simulations, the standard $k$-$\varepsilon$ is more widely adopted since it

obtains results with a reasonable accuracy for a wide range of turbulent flows and it provides less convergence issues.

The results of three different simulations are compared adopting always the KHRT model and the fixed mesh. They differ for the turbulence model used: the first one adopts the standard $k$-$\varepsilon$ model with $C_{1\varepsilon}$ = 1.5 as suggested by ECN, the second one adopts again the standard $k$-$\varepsilon$ model with $C_{1\varepsilon}$ = 1.44 (default value for standard $k$-$\varepsilon$ model and well validated in CFD simulations), the third one adopts the RNG $k$-$\varepsilon$ model with the coefficients suggested by [26].

The main results of interest are the ones regarding the axial velocity plot as function of time (Figure 6.9), since the effects of the turbulence models on the gas motion should be well represented by this graph. The two cases adopting the standard $k$-$\varepsilon$ model have very similar trends and the one with $C_{1\varepsilon}$ = 1.44 predicts a peak of velocity that is higher. Instead the curve produced by the RNG exhibits very different results. Both the positive and negative peaks of velocity are strongly underestimated in terms of magnitude. Looking at the vortex motion simulated by this model, it is possible to notice how they are less intense with respect to the ones provided by the standard $k$-$\varepsilon$ model.

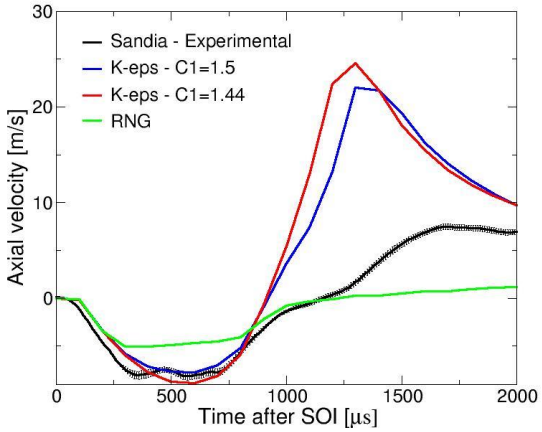


***Figure 6.9 - Axial velocity as function of time provided by the different turbulence models***

The liquid penetration plots (Figure 6.10) show how RNG model provides very high penetration values with respect to the other cases. Comparing the simulations which adopts the standard $k$-$\varepsilon$ model, the penetration values tend to decrease as the $C_{1\varepsilon}$ is reduced.

A rigorous analysis would require a further calibration of the constants for each turbulence model adopted, but some useful considerations can be obtained from this comparison. The RNG $k$-$\varepsilon$ model with this configuration does not improve the results obtained with the standard $k$-$\varepsilon$ model, on the contrary it introduces an evident underestimation of the intensity of the gas vortexes during all the simulated time interval. For the standard $k$-$\varepsilon$ model a significant difference between experimental and computed data is observed in Figure 6.9 only after the end of injection. When adopting for this model a value of $C_{1\varepsilon}$ = 1.44, the velocity peak shown in Figure 6.9 worsen. For these reasons, it is better to maintain the original setup for turbulence model with the standard $k$-$\varepsilon$ model and $C_{1\varepsilon}$ = 1.5 (as suggested by the literature for spray simulations).

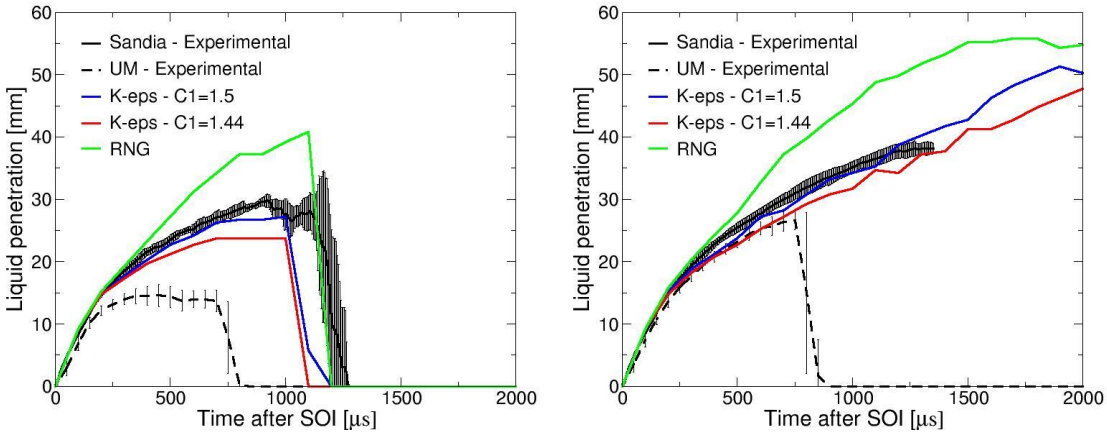


***Figure 6.10 - Liquid penetration for different turbulence models according to the two thresholds of LVF: 2 $mm^3/mm^2$ (a) and 0. 2 $mm^3/mm^2$ (b)***

The difference in the results suggest that all the sub-models are inherently linked. So, the choice of each sub-model and its calibration strongly depends on the other sub-models adopted.

## 6.4. SPRAY ORIENTED MESH

According to Stiesch [16], the Lagrangian-Eulerian simulations provides very different results when performed on different numerical grids. Almost all characteristic spray parameters are strongly influenced by the mesh adopted. The results do not necessarily converge for successively refined grids; thus, the values obtained from a fine grid are not guaranteed to be better than the ones obtained with a coarse grid. Moreover, grid dependant results are not only observed for different cell size but also for varying grid arrangements and design.

Stiesch (recalling the work by Otto et al. [27]) suggests some measures to achieve good results with spray simulations. Among them, there is the adoption of spray-oriented grids. The penetration values and the spray characteristics are better predicted if the spray parcels cross perpendicularly the grid lines.

According to this suggestion, a simulation adopting a spray-oriented grid is performed and then its results are compared to the ones obtained with the two meshes described at the beginning of this chapter (the dynamic mesh with AMR and the fixed mesh obtained with *snappyHexMesh*). The spray-oriented mesh is obtained by adapting a typical grid used for diesel engines simulations to the specific case of spray G. This grid arrangement allows to exploit the radial symmetry of the problem, since the spray G geometry presents eight injector holes that are symmetric with respect to the injector axis. Imposing the proper symmetry boundary conditions, it is possible to consider only the behaviour of a slice corresponding to one eighth of the whole system. This means that only one of the eight plumes are effectively simulated, while the symmetry boundary conditions account for what happens in the remaining part of the system that is not simulated.

The resulting mesh is represented in Figure 6.11. Its quality mesh can be described as it is done for the other cases:

- fixed mesh with rotating symmetry boundary conditions; 1000000 cells; maximum aspect ratio: 2243 (121 cells with high aspect ratio); maximum non-orthogonality: 55.44; average non-orthogonality: 24.70; max skewness: 1.43.

The mesh quality is not very good because it is hard to adapt a grid arrangement designed for diesel engines to spray G (they have very different injection angles: 34° for spray G and typically 77.5° for diesel with respect to z-axis). With such poor-quality mesh, the results expected could not be so accurate.

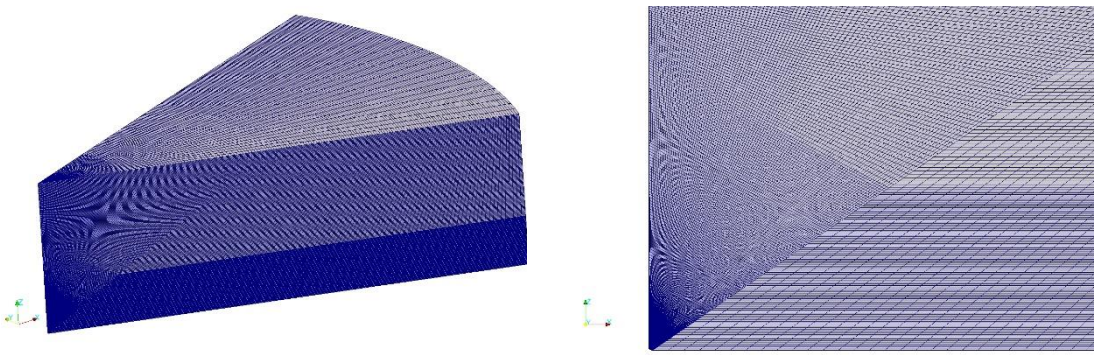

***(a)*** ***(b)***

***Figure 6.11 - Picture of the spray-oriented mesh (a) and a detailed view of the grid close to the injection zone (b)***

Other many attempts adopting this mesh design with different refinements have been tested, but their simulations did not reach convergence. Only for this specific grid the simulation has provided results without error messages.

The liquid penetrations obtained by the spray-oriented mesh (Figure 6.12) are not so different from experimental data and from the results provided by other grids. Moreover, the penetration values provided by this last mesh are slightly higher as expected for spray-oriented grids.

Postprocessing all the other quantities of interest, some differences are highlighted when the spray-oriented mesh is used. An example is the axial velocity plot (Figure 6.13) where the profile provided when using this new grid is quite flat and completely different from experimental data and from the results of the other simulations.

These unexpected results deserve a deeper investigation. Some errors and wrong predictions obtained up to now could be the result of the grid dependency observed in Lagrangian-Eulerian problems. To obtain a comprehensive analysis and a better setup for spray G simulations, also these numerical errors must be considered and studied.

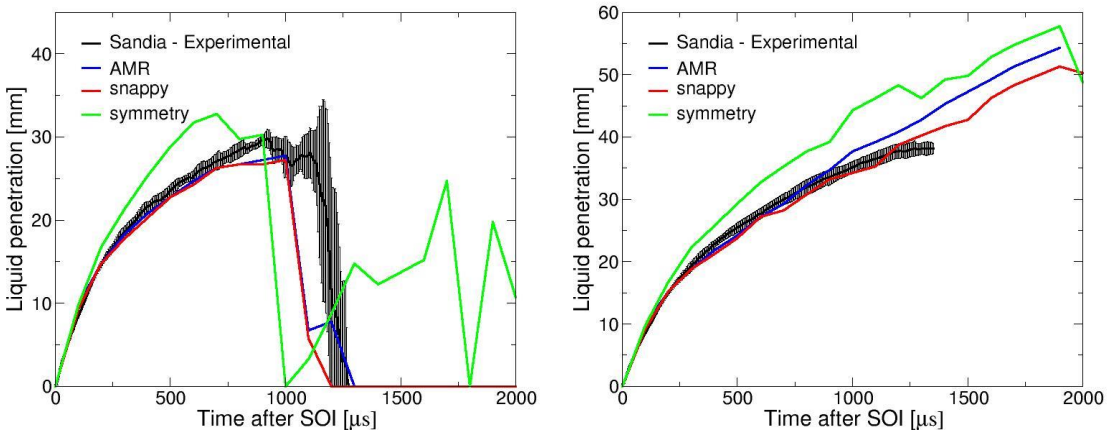


***Figure 6.12 - Liquid penetration for the different grid arrangements according to the two thresholds of LVF 2 mm³/mm² (a) and 0. 2 mm³/mm² (b)***

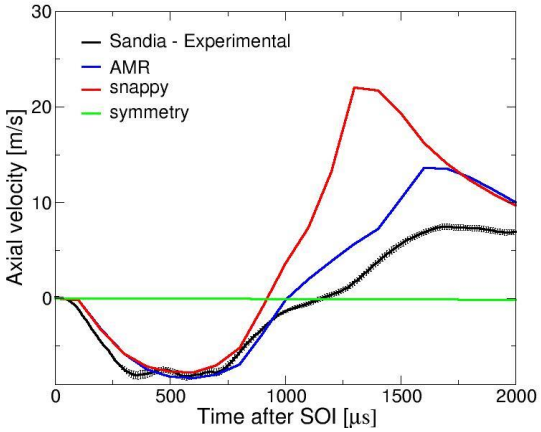


***Figure 6.13 - Axial velocity as function of time for different grid arrangements***

# 7. SPRAY SIMULATIONS: NUMERICAL ANALYSIS

In this chapter, a numerical analysis on the grid dependency of the results is performed to evaluate the effects of the grid structure on the results of spray simulations. Together with the choice of the models, a correct grid design is the key to obtain reliable results in spray simulations by the Lagrangian-Eulerian approach.

In this analysis, the spray G configuration is set aside for a while and a new spray configuration based on typical diesel engines sprays is adopted. This choice is done with the aim to exploit the longer experience and the deeper knowledge gained by the ICE group about spray-oriented grids for diesel engines. This longer experience is explained by historical reasons, in fact, diesel engines CFD simulations have been performed for a longer time with respect to GDI engines. Spray-oriented grids are commonly used in diesel simulations today and they provide reliable results, while for spray G they are not the standard. As drawback, the references provided by experimental data are no more useful since the configuration of the system is changed. A new reference must be set to overcome this problem. Since this analysis is purely numerical, the new reference is represented by a numerical setup adopted as a base case to which all the simulations performed are compared.

This study wants to deeper investigate how the grid arrangement affects the simulation results. In particular, the objective is to verify the numerical effects described in [16] on different grid arrangements: cartesian grids and spray-oriented grids. At the end, summing up all the considerations, the different mesh configurations are compared evaluating their application in spray G simulations.

## 7.1. REFERENCE SETUP DEFINITION

Since the objective of this analysis is to study the dependence of the results on the grid arrangement; models, submodels and their parameters are not changed, since they are not the focus for this part of the work. Their choice is performed by adopting a well established setup used by the ICE group in diesel engines simulations.

The fuel injected is n-dodecane and the injection law is changed by adopting a mass flow rate typical of diesel engines (it is proposed on ECN website for spray A conditions). Temperature and pressure are changed respectively to 1000 K and 160 bar. The number of parcels injected is 150000 per each hole, since the mass of fuel is increased. The time discretization is changed too: the start time corresponds to 0 s, the end of injection is approximately at 1.66 ms, while the simulation end time corresponds to 2.5 ms. The chosen time step is again 0.001 ms. The turbulence model is the standard $k$-$\varepsilon$ model where $C_{1\varepsilon}$ = 1.5, while the spray is modelled with the blob injection model for atomization (constant spray angle equals to 16°, $C_d$ = 0.99) and the KHRT model for secondary breakup ($B_1$ = 25; $C_{RT}$ = 0.20). As already highlighted, the references given by experimental data are no more valid for this configuration. For this reason, a numerical setup is built by applying the measures suggested by Stiesch for a correct grid design in spray simulations.

What results is a system adopting a cartesian grid composed only by identical cubical elements. Its quality results to be the best possible. In the system, only a single injector hole is present and the injection direction is directed parallel to the z-axis. With this geometry, the spray parcels cross the grid lines exactly perpendicular. So, this reference case is composed by a single plume of spray that is simulated by a grid which is simultaneously spray-oriented and cartesian with the highest quality possible (Figure 7.1). The idea is to obtain information regarding only a single spray plume in the best configuration allowed by numerical constrains and then to compare them with the corresponding results obtained by simulating the same plume in different grid arrangements.

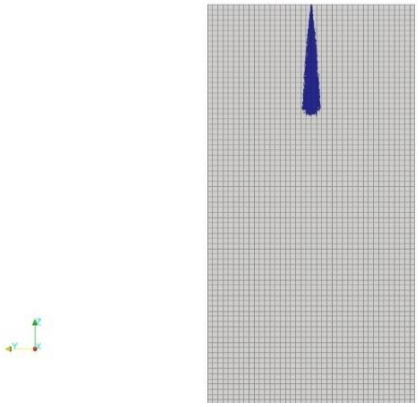

***Figure 7.1 - Mesh representation for the reference case in the numerical analysis***

Once the geometry has been decided, only the cell size must be chosen. According to [28] and [29], in Lagrangian-Eulerian simulations the results converge for successively refined grids, like in Eulerian simulations, only if the void fraction approaches zero. The void fraction is defined as:

$$vF = \frac{V_{liq,cell}}{V_{cell}} \tag{7.1}$$

Where $V_{liq,cell}$ is the volume of all the liquid parcels that are contained in a cell for a specific time step, while $V_{cell}$ is the volume of the cell considered. The void fraction is equal to zero when no liquid is present inside the cell. Its value can assume values ever greater than one: this is possible because the Lagrangian parcels are treated as individual mass points and there is not a limit of parcels that a cell can contain. So, a condition can be found where the volume of liquid drops inside a cell is greater than the volume of the cell itself. This is unphysical but it is allowed by the CFD code. If the void fraction exceeds values in the order of $10^{-2}$, some numerical errors can be observed when the momentum exchange between the two phases is considered. Once the momentum that must be transferred from the liquid phase to the gas phase is determined, the source term in the momentum equation of the gas phase can be evaluated. This source term is uniformly distributed over all the gas present in the cell. The momentum exchanged between the two phases depends on mass and not on volume. So, considering that the ratio between $\rho_l$ and $\rho_g$ is in the order of $10^2$ for this kind of problems, when the void

fraction assumes values close or greater than unity, a large amount of momentum is transferred to a small mass of gas. What results is that the liquid drops are not slowed down by the gas phase that suddenly accelerates reaching the same velocity of the liquid.

To evaluate the most suitable mesh size, three different cases are compared using the same mesh design described above, adopting successively refined grids. The lengths adopted are 2 mm, 1 mm and 0.5 mm. Such values are the same used in spray G simulations and they are commonly adopted in engines simulations.

The void fraction for the three simulations is analyzed to be sure that it assumes values much smaller than unity, avoiding the introduction of numerical errors. In Table 7-1, the maximum values that the void fraction assumes in the simulations are reported for three different time-steps, corresponding respectively to half of injection, end of injection and 0.4 ms after the end of injection. Only for the finer mesh it assumes values in the order of $10^{-2}$; while for the other cases, it is much smaller. For all the simulated conditions, the maximum void fraction does not reach values that can compromise the computed results.

| | **0.8 ms** | **1.6 ms** | **2.0 ms** |
|---|---|---|---|
| **0.5 mm** | 0.04 | 0.03 | 0.002 |
| **1.0 mm** | 0.007 | 0.008 | 0.0004 |
| **2.0 mm** | 0.0019 | 0.0018 | 0.0001 |

***Table 7-1 - Maximum void fraction values for three different mesh refinements evaluated for three different time steps***

The penetration values are computed using a different reference system with respect to the one represented in Figure 7.1. This new system is created by rotating the original one to obtain an angle of 77.5° between the injection direction and the z-axis. By doing so, the penetration values obtained here are computed coherently with the ones that are obtained in the following parts of this analysis. The vapor penetration values (Figure 7.2) obtained for the three cases exhibit a convergence trend, as it is expected when the void fraction is much lower than unity. The same can be stated also for liquid penetrations.

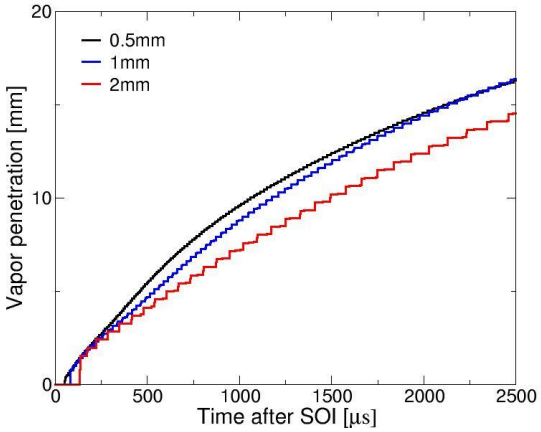


***Figure 7.2 - Vapor penetration value for different grid refinements***

The other quantities of interest in this analysis are the liquid and vapor velocities evaluated along the plume length for the time steps already considered for the void fraction evaluation. In Figure 7.3, the vapor velocities are plotted and the convergence trend can be observed also for this graph.

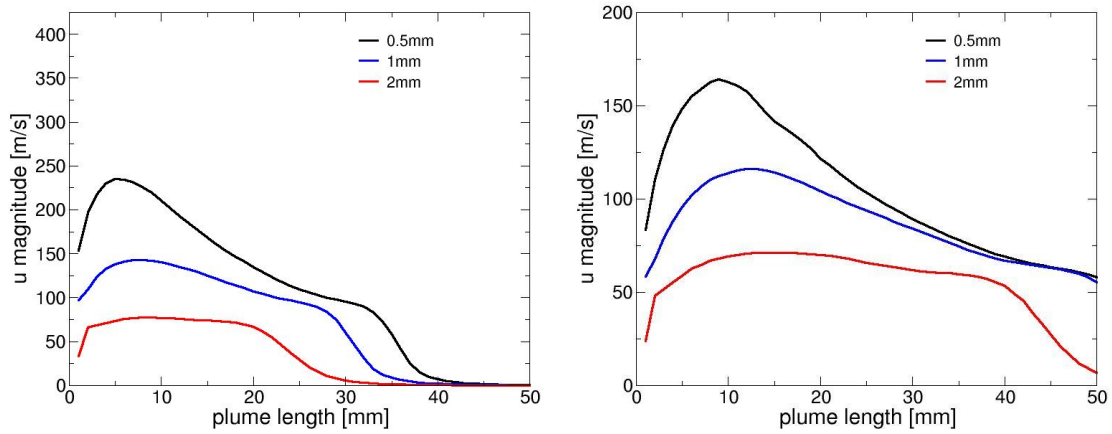


***(a)*** ***(b)***

***Figure 7.3 - Vapor velocities measured along the plume length for different mesh refinements, evaluated at 0.8 ms (a) and 1.6 ms (b) after SOI***

For the liquid velocity graphs (Figure 7.4), very similar comments can be done but there is something that deserves further attention. All the curves exhibit a decreasing trend with a sudden drop corresponding to the end of the plume. The gradient in that position becomes steeper as the cells are refined and the values of liquid velocity corresponding to the plume tip are significantly different. This has a great impact when the wall impingement is evaluated in engines numerical simulations. For this reason, this region must be accurately evaluated by the numerical simulation.

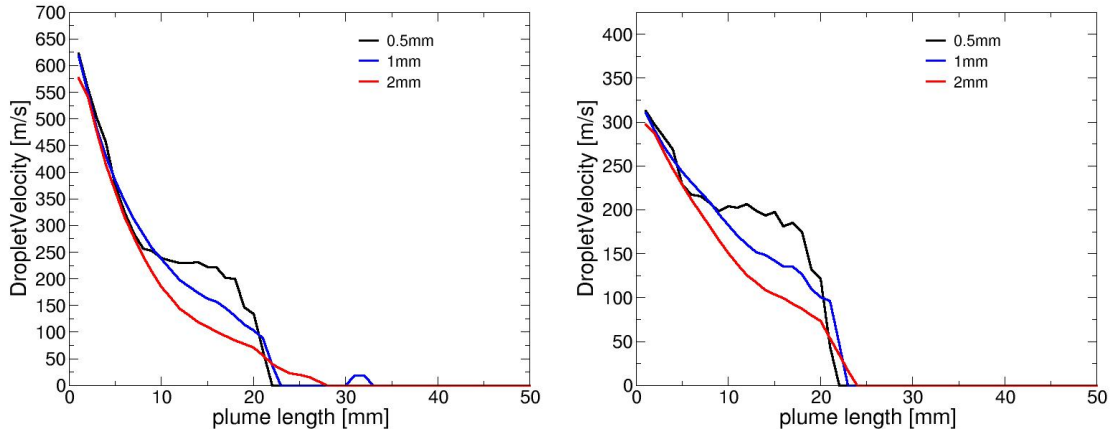


***(a)*** ***(b)***

***Figure 7.4 - Liquid velocities measured along the plume length for different mesh refinements, evaluated at 0.8 ms (a) and 1.6 ms (b) after SOI***

The case which adopts the most refined mesh is chosen as reference for this part of the work. The lack of convergence typical of numerical errors is not shown in this analysis and the values of void fraction are sufficiently smaller than 1. This guarantee that the effects provided by numerical errors are not so significant in these cases.

## 7.2. ANALYSIS ON CARTESIAN GRIDS: AREA CONTRACTION COEFFICIENT EFFECT

Cartesian grids are commonly adopted in spray simulations, as it is possible to notice in the spray G analysis performed in this work. The choice of this grid arrangement allows to obtain a very good quality mesh with a very simple design. As drawback, when the spray direction is not aligned with the grid lines (as in most of the cases with a cartesian mesh) the liquid parcels result slowed down more than they really are in experimental measurements. This brings to an underestimation of the penetration values. This can be explained as follows: changing the reciprocal orientation between spray and grid lines, the number of cells crossed by a liquid parcel change. This changes also the mass of gas involved in the momentum exchange between the two phases with a consequent different evaluation of the momentum transferred from the liquid to the gas.

According to Stiesch [16], it is a common practise to tune model parameters in order to adjust the calculations to the specific numerical grid. In other words, models and sub-models are trimmed to unphysical behaviours to overcome the deficiencies caused by inadequate grid. For the case of spray simulations in cartesian grids, it is common to reduce the area contraction coefficient $C_d$ in order to increase the injection velocity of the liquid compensating the slowdown effect previously described. Usually the $C_d$ is adjusted starting from experimental measurements to fit the penetration values. This requires a proper modification of the sub-models adopted in the simulation. For example, the droplet breakup strongly depends on the relative velocity between liquid and gas. When $C_d$ is modified to fit penetration data, the resulting liquid velocities result overestimated with respect to experimental data. The droplet breakup is strongly influenced by this situation and the parameters of the breakup models must be adjusted to compensate the changes in relative velocities. This is the reason why, during the analysis of KHRT models in spray G problems, the simulations provide always underestimated SMD and overestimated liquid velocities.

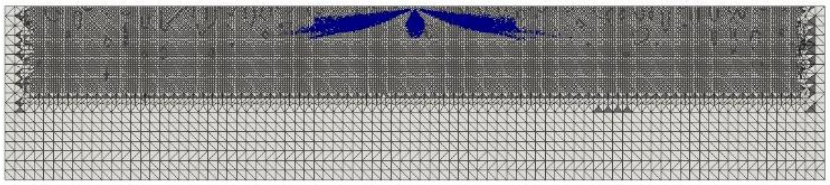

***Figure 7.5 - Section of the cartesian mesh adopted for the simulations***

In this analysis, a cartesian mesh is used to simulate the behaviour of eight plumes with the same model and physical characteristics described during the previous chapter. The eight injector holes are arranged in circle around the z-axis with a radial symmetry. The angle between this axis and the injection direction is 77,5°. Three different $C_d$ values

(0.99, 0.8 and 0.6) have been adopted and their results are compared to the refence case defined in the previous paragraph. The mesh (Figure 7.5) is composed all by cubical elements with 2 mm sides and it presents a refinement box with 0.5 mm side cells in the region where the presence of the spray is expected (the mesh is built up similarly to the "snappy cube" case in spray G analysis).

The vapor penetration plot (Figure 7.6) shows how the penetration values increases as the $C_d$ is decreased. Moreover, being the same the $C_d$ (equals to 0.99), the results provided by the reference case (where the mesh is spray-oriented) are greater than the ones provided by the cartesian mesh (that is not spray-oriented). The curve obtained with $C_d$ = 0.6 is the closest to the reference case

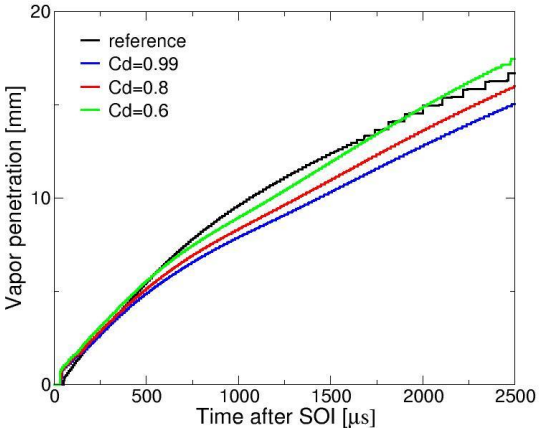


***Figure 7.6 - Vapor penetration values adopting different area contraction coefficients***

The liquid velocity curves (Figure 7.7) show how the velocity is increased as the $C_d$ is reduced. Approaching the injection point, the velocity predicted by the cartesian mesh with $C_d$ = 0.6 is strongly greater than the ones predicted by the reference case, while the case with cartesian mesh and $C_d$ = 0.99 is very similar to the reference, as it is expected. This is because, close to the injection point, the cells crossed by the spray parcels are few and the numerical error cumulated when the parcels do not cross the grid lines perpendicularly is still small. Moreover, all the curves provided by the cartesian mesh do not exhibit the step provided by the reference case corresponding to the tip of the plume with a consequent impact on possible wall impingement.

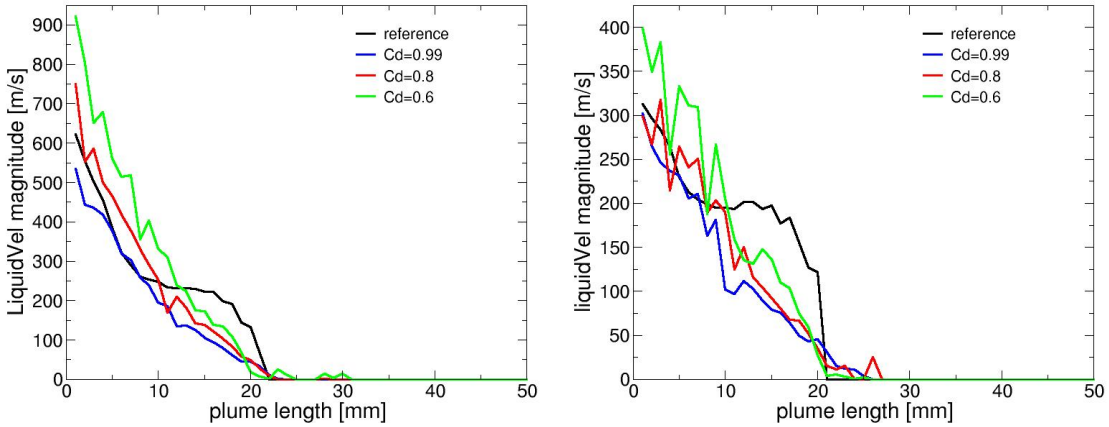


***Figure 7.7 - Liquid velocities measured along the plume length for area restriction coefficients, evaluated at 0.8 ms (a) and 1.6 ms (b) after SOI***

The maximum void fraction evaluated in all the three cases with the cartesian mesh do not exceed the value of 0.09 that can be considered acceptable.

When a cartesian mesh is adopted, the penetration values are underestimated, being the same all the other conditions. The tuning of the area contraction coefficient can be a solution to counterbalance the numerical effects introduced when the spray parcels do not cross the grid lines perpendicularly. As drawback, the resulting velocities are overestimated and this situation should be accounted while the breakup models are implemented. Moreover, all the cases with the cartesian mesh provide velocity profiles different from the reference case close to the tip of the plume.

The adoption of cartesian grids with a proper tuning of the area contraction coefficient allows to obtain reliable results of penetration maintaining a very simple grid design. Some side effects, such as the liquid velocity overprediction, are unavoidably introduced in the simulation. They can be smoothed by properly modifying the submodels parameters, but they cannot be eliminated. To conclude, this grid arrangement can be a good compromise that allows to obtain satisfactory results with a simple design, but it requires to be conscious of what it implies.

## 7.3. ANALYSIS ON SPRAY-ORIENTED GRIDS

According to the literature, the spray characteristics result better predicted if a spray-oriented grid is adopted, but this requires a careful mesh preparation. Compared to cartesian grids, spray-oriented grids have worse mesh quality (mainly in terms of non-orthogonality and aspect ratio) and provide high void fraction values close to the injectors holes where the cells are usually small.

The same spray configuration that has been adopted in the previous paragraph is now simulated with a spray-oriented mesh. The results obtained are compared to the reference case and to the results provided by the cartesian mesh.

### 7.3.1. Comparison between Spray-Oriented and Cartesian Grids

The spray-oriented grids adopted in this analysis are drawn using a typical mesh design adopted by the ICE group for diesel engines simulations as reference. This design is the result of years of experience in this field and it is widely adopted showing up satisfactory results.

In this analysis two simulations are performed adopting the same spray-oriented mesh layout (Figure 7.8) with different grid refinements. The first simulation performed uses a fine mesh that provides high void fraction values. Instead, the second simulation uses a coarse mesh where each side of the geometry is discretized by adopting a number of cells that is the half with respect to the fine mesh. The second simulation was run with the purpose to limit the void fraction issues observed in the first simulation.

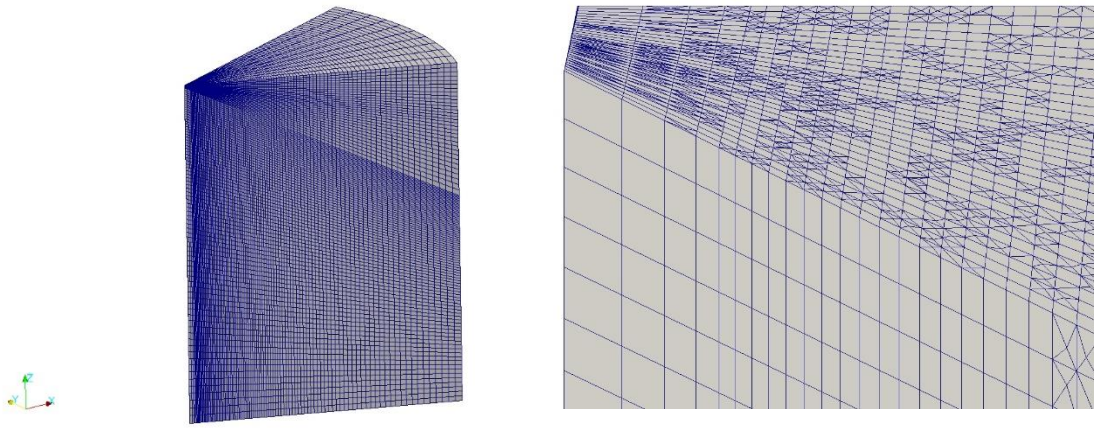

***(a)*** ***(b)***

***Figure 7.8 - Spray-oriented grid adopted for simulations (a) and detailed view of the mesh close to the injection region (b)***

The properties of the two grids can be summarized as:

- Oriented fine: fixed mesh with rotating symmetry boundary conditions; 116480 cells; maximum aspect ratio: 82.09; maximum non-orthogonality: 26.34; average non-orthogonality: 13.77; max skewness: 1.24.
- Oriented coarse: fixed mesh with rotating symmetry boundary conditions; 15120 cells; maximum aspect ratio: 120.87; maximum non-orthogonality: 26.33; average non-orthogonality: 13.78; max skewness: 1.24.

The mesh quality is very similar for the two cases since the grid layout is the same, while the number of cells of the fine mesh is eight times the number of cells of the coarse mesh.

The cases adopting the spray-oriented mesh are compared to the reference case and to the simulation with the cartesian mesh and $C_d$ = 0.6. In Table 7-2 the maximum values that the void fraction assumes are compared for three different time steps. The “Oriented fine” case presents void fraction values higher than one. According to Abraham [29], the numerical error introduced in the momentum exchange between the two phases is not negligible in this case. In the “Oriented coarse” case, the void fraction is smaller, but the numerical error remains not negligible.

| | 0.8 ms | 1.6 ms | 2.0 ms |
|---|---|---|---|
| **Reference case** | 0.04 | 0.03 | 0.002 |
| **Oriented fine** | 1.36 | 1.57 | 0.020 |
| **Oriented coarse** | 0.62 | 0.59 | 0.016 |
| **Cartesian ($C_d$ = 0.6)** | 0.09 | 0.09 | 0.002 |

***Table 7-2 - Maximum void fraction values for different grid arrangements evaluated during three different time steps***

Comparing the vapor penetration (Figure 7.9), the curves provided by the spray-oriented meshes approximate better the trend described by the reference curve, in particular the curve gradients results well predicted.

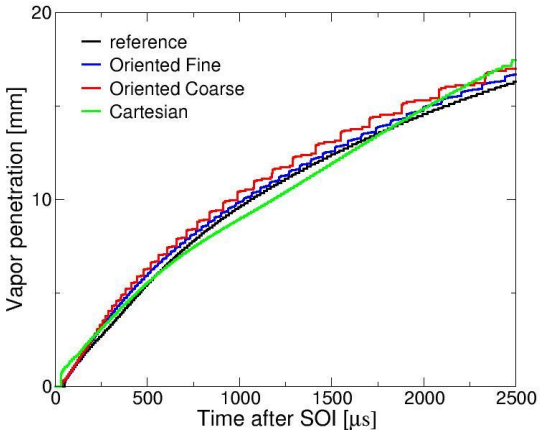


***Figure 7.9 - Vapor penetration values adopting different grid arrangements***

In Figure 7.10, the liquid and gas velocity profiles evaluated along the plume length are reported for the same time step. Close to the injection position, both the spray-oriented meshes provide liquid velocity results closer to the reference case with respect to the cartesian mesh, since they do not adopt a tuned value of $C_d$. For the liquid velocity plot, it can also be noticed that the spray-oriented grids (the fine one in particular) predict a step, that becomes steeper as the grid is refined, corresponding to the plume tip. This agrees with the results of the reference case and it is not predicted by cartesian grid. In the gas velocity profile, the spray-oriented grids provide overestimated values close to the injection position and the trend of their plots, as the injection position is approached, is completely different from what is shown in the reference and the cartesian curves.

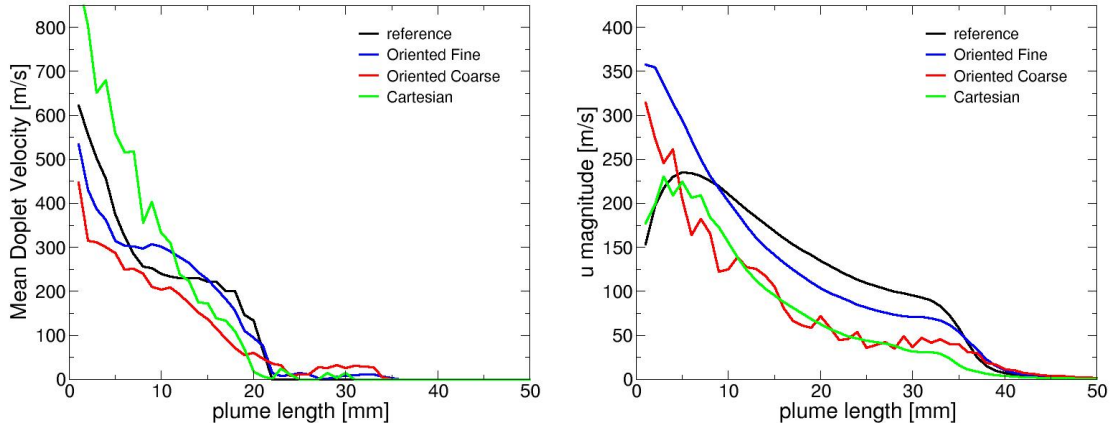


***Figure 7.10 – Liquid (a) and gas (b) velocities measured along the plume length for different mesh arrangements, evaluated at 0.8 ms (a) after SOI***

From the results obtained with spray-oriented mesh, two main issues related to this grid arrangement are highlighted. First, both the simulations adopting spray-oriented grids provides high void fraction values. Second, the mesh quality is poor in term of aspect ratio. A deeper analysis is performed to understand how aspect ratio and void fraction affect the results, before drawing some conclusions on spray-oriented grids.

### 7.3.2. Void Fraction and Grid Refinement of the Injection Region

According to the literature, void fraction values close to or greater than unity are undesired in spray simulations since they introduce numerical errors while the momentum exchange between the phases is evaluated. The “Oriented fine” and “Oriented coarse” meshes adopted before provide high void fraction in those cells that are close to the injection location. They are extremely unfavoured from this point of view because they are very small cells (as result of the mesh design) and they contain a lot of liquid parcels since, close to the injection location, the liquid drops of the spray are very close one to the others. To overcome this problem, a less refined grid can be adopted, but this imply a poorer space discretization of the domain. Comparing the “Oriented coarse” mesh with the “Oriented fine” one, some consequences of the poor discretization can be observed in the vapor penetration of Figure 7.9.

A good solution can be found by manipulating the cells that provide the higher values of void fraction. The idea is to enlarge only those cells that are close to the injection position (they are the ones where the void fraction assumes its maximum value) while the cells that discretize the remaining part of the domain are kept unchanged. The mesh results divided into two regions (Figure 7.11); only the one corresponding to the injection location is modified. The results obtained with simulations adopting different grids refinements for the injection regions are compared. The different refinements are obtained by changing the number of cells used to discretize the system in the radial direction. For example, in Figure 7.11 the cells adopted in the radial direction are 4. The base mesh is

the “Oriented fine” ones and the comparison is performed between three case with respectively 4, 8 (corresponds exactly to the “Oriented fine” case) and 12 cells for the radial discretization of the injection region. The injection region length measured along the plume direction is approximately 3 mm in this analysis.

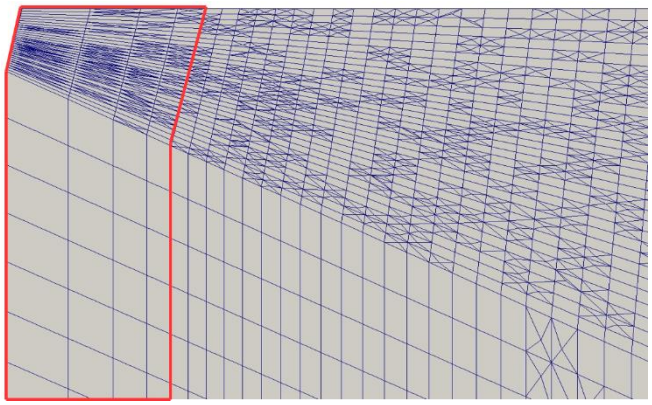

***Figure 7.11 - Grid detail close to the injection position; the region highlighted with red borders contains the cells that have been modified during this analysis***

Table 7-3 shows a strange trend: the void fraction tends to decrease as the grid adopted for the injection region becomes coarser, when it is considered a time step in the middle of the injection process (0.8 ms). While the opposite happens at the end of injection (1.6 ms). The maximum void fraction is always found in those cells that belong to the injection region. This suggest that a simple cell enlargement is not enough to reduce the void fraction. The reduction of the void fraction by manipulating the cell size is a very complex problem that depends both on the geometry of the grid and the shape of the spray.

| | **0.8 ms** | **1.6 ms** | **2.0 ms** |
|---|---|---|---|
| **4 cells** | 1.04 | 1.74 | 0.020 |
| **8 cells** | 1.36 | 1.57 | 0.020 |
| **12 cells** | 1.78 | 0.45 | 0.020 |

***Table 7-3 - Maximum void fraction values for different injection region refinements in spray-oriented grids during three different time steps***

Moreover, when 4 cells are adopted for the discretization of the injection region, the simulation provides some convergence issues, that can be overcome by halving the time step of the simulation. The literature agrees on stating that this introduces another problem. For this kind of simulations, when the time step is changed, the results provided can be significantly different even if the setup adopted is the same.

Since this attempt to reduce the void fraction by manipulating the cells has not produced relevant results, another approach to the void fraction issue has been tried. To avoid the complications introduced by the complex spray-oriented geometry, this part of the analysis adopts the reference case as starting point. The idea is to refine the injection

region of the reference case to increase the void fraction and observe how the results change. The injection region length is chosen to be 12 mm. All the simulations presented in this comparison adopt the same mesh design of the reference case with different level of refinements for the injection region (Figure 7.12). The results obtained from three different cases are compared; they respectively adopt a level of refinement equals to 0 (it is the reference case where the cells have a characteristic length of 0.5 mm), 1 (the cells have a characteristic length of 0.25 mm) and 2 (the cells characteristic length results equal to 0.125 mm).

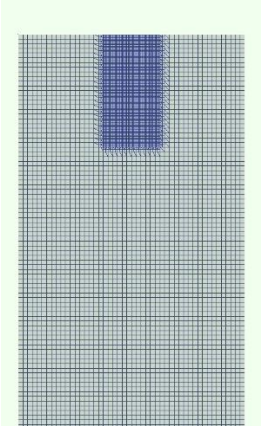

***Figure 7.12 - Section of the reference mesh with a refined injection region***

Table 7-4 shows an increase of void fraction for all the time steps when the cell characteristic length becomes smaller. The cases with a refinement level equals to 1 and 2 provide void fraction values by which the numerical errors are no more negligible.

| | **0.8 ms** | **1.6 ms** | **2.0 ms** |
|---|---|---|---|
| **No refinement** | 0.04 | 0.03 | 0.002 |
| **Refinement level 1** | 0.23 | 0.19 | 0.016 |
| **Refinement level 2** | 0.85 | 0.82 | 0.078 |

***Table 7-4 - Maximum void fraction values for different injection region refinements in the reference setup, during three different time steps***

In the vapor penetration plot (Figure 7.13) some differences between the curves are highlighted when the level of refinement is changed. According to the literature, the results reported in this graph do not exhibit a clear tendency to converge. On the contrary, in Figure 7.2 this trend can be observed because the void fractions obtained are small for all the cases.

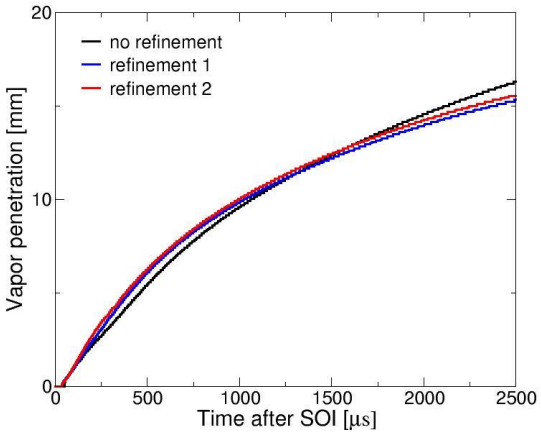


***Figure 7.13 - Vapor penetration values adopting different grid refinements in the injection region***

Other useful information can be obtained by plotting on the same graph the liquid and vapor velocities (Figure 7.14) of the three simulations. Considering the case which provides the highest void fractions, the liquid and gas curves are quite overlapped close to the injection location. This is a typical numerical effect observed when the void fraction is close to unity: the liquid drops are not slowed down by the gas phase that suddenly accelerates reaching the same velocity of the liquid. Inside a cell, the mass of liquid is much greater than the mass of gas, so the CFD code tends to neglect the contribution of the gas phase while the momentum exchange is evaluated.

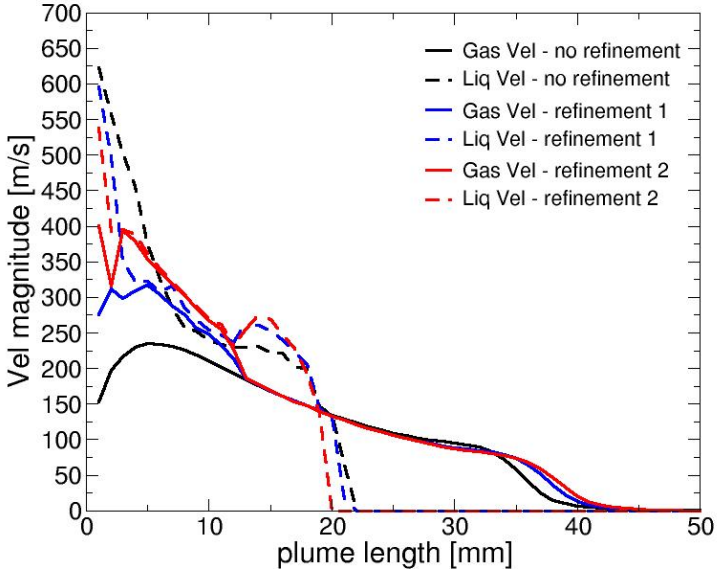


***Figure 7.14 - Liquid and Gas velocities for different injection region refinements evaluated at 0.8 ms after SOI***

Here, the typical numerical effects provided by high void fraction values are observed. According to the literature, void fractions greater than $10^{-2}$ must be avoided because they lead to wrong predictions. The error committed is not negligible and it is clearly represented by the velocity magnitude plot of Figure 7.14. This has a great impact

on the droplet breakup since the relative velocity between gas and liquid changes a lot. For this reason, the cell size must be chosen carefully accounting also for the void fraction. In the case of the reference setup a characteristic length of 0.5 mm for the cells is a compromise that allows to have a fine space discretization and void fraction values still good. This observation can be extended also for cartesian grids studied in this chapter.

### 7.3.3. Aspect ratio effects

The spray-oriented grids adopted during this numerical analysis have high aspect ratio. In the practice, cells that are stretched in the flow direction are commonly accepted if the gradients of the flow properties are not great. Close to the injection location, the liquid velocity gradients can be important. In this region, the spray-oriented grids used in this work adopt cells stretched in the plume direction with an aspect ratio that approximately ranges from 5 to 10.

The effects produced by high aspect ratio cells are evaluated by adopting the simplest geometry possible, that is the reference case used in this analysis. Starting from this geometry, other two simulations are performed only by modifying the mesh. The grids adopted are obtained by stretching the reference mesh on the spray direction. By doing so, a comparison is performed among three meshes with different aspect ratio: 1 (corresponding to the reference case), 5 and 10. These values are chosen since they are the same that can be found in the spray-oriented grid close to the injector.

The void fraction does not represent a problem during this comparison since the maximum values that it assumes in all the simulations are sufficiently smaller than unity.

The plot which reports vapor and liquid velocities (Figure 7.15) shows some interesting results. Approaching the injector hole, the liquid velocity is predicted similarly when the aspect ratio is 1 and 5, but important differences are shown when the aspect ratio is 10. The other postprocessed quantities are not of interest, since the attention is focused on studying how the presence of high aspect ratio cells close to the injection position affect the velocity predictions.

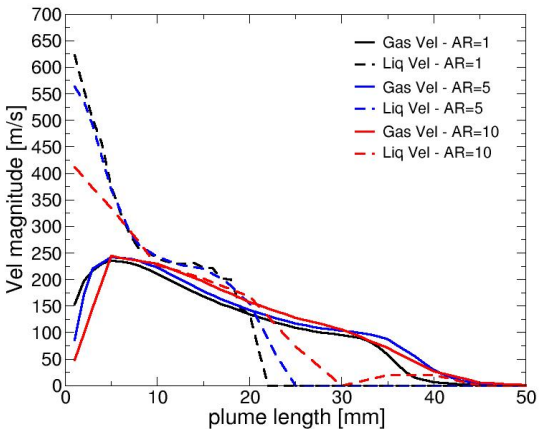


***Figure 7.15 – Liquid and Gas velocities for grids with different aspect ratio evaluated at 0.8 ms after SOI***

The velocity profile inside a cell is obtained by linear interpolation, when this numerical setup is adopted. For this reason, where the gradients are high, the aspect ratio must be limited to better describe the velocity profile. In this configuration an aspect ratio equal to 5 is still acceptable. Changing the configuration, also this threshold value for the aspect ratio changes. In spray-oriented grids, close to the injector location, the aspect ratio of the mesh elements must be carefully checked before performing the simulation. When this is not done, the wrong velocity predictions could affect the droplet breakup. A proper tuning of the breakup model parameters can be useful to overcome this issue.

### 7.3.4. Final considerations on spray-oriented grids

Spray-oriented grids well predicts the liquid velocity profile without a proper tuning of the $C_d$, but they require a very careful design to avoid void fraction and aspect ratio issues. In diesel engines (Figure 7.16), they are commonly used since the combustion chamber geometry well fit this grid design. In spray G simulations, where the geometry is changed, the mesh becomes very complex to design. For example, the adoption of a grid defined by blocks can be adopted. Where the spray presence is expected, a spray-oriented grid can be used, while the remaining part of the geometry can be filled with polyhedral cells. The mesh design process results very complex.

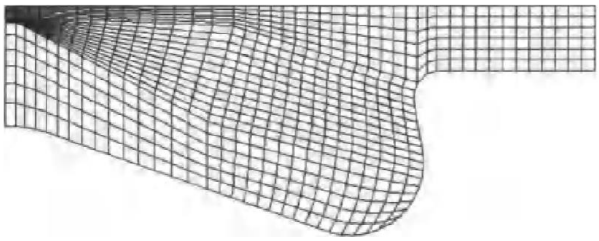

***Figure 7.16 - Spray-oriented grid applied for a typical diesel engine geometry***

In chapter 6, some differences between cartesian and spray-oriented grids have been highlighted in the axial velocity profile as function of time (Figure 6.13). The results have shown how the magnitude of the predicted gas velocity is strongly smaller when a spray-oriented grid is adopted. The same graph is drawn for the cases studied in this numerical analysis. The sampling point is always located on the injector axis, but the distance measured between the sampling point and the injector position is reduced from 15 mm to 5 mm, since the configuration of the problem is changed too. The cases considered for this comparison are the "Oriented fine" one and the case that adopts the cartesian mesh and $C_d$ = 0.99 (the $C_d$ is the same for the two cases compared).

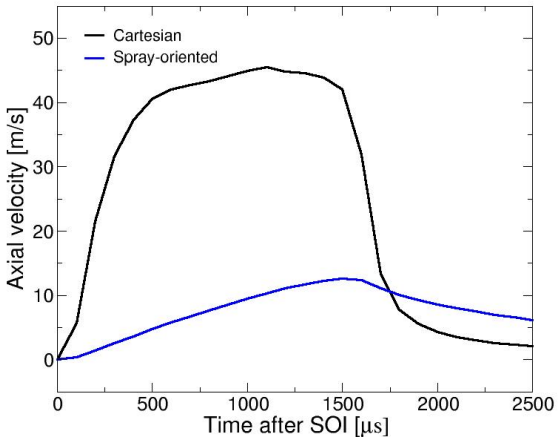


***Figure 7.17 - Axial velocity as function of time for a cartesian grid and a spray-oriented grid***

In Figure 7.17, the curves show how the spray-oriented grid underpredicts the gas velocity also for the configuration studied in this numerical analysis.

The sampling point considered is very close to the axis of symmetry adopted in the spray-oriented grid. To be sure that this problem is not related to the symmetry boundary condition, another simulation is performed. This case simulates all the eight plumes of the spray, like it is done in the cartesian mesh, by adopting a spray-oriented grid with the same section of the others spray-oriented grids used up to now. This case does not adopt symmetry boundary conditions. The results do not provide differences with respect to the cases where the spray-oriented grid and cyclic symmetry boundary condition are adopted. So, the trend observed in the axial velocity plots is not a matter of symmetry boundary condition, but it is related to the different grid arrangements.

To understand the reason why the curves of Figure 7.17 are so different, the pressure field for the cartesian and the spray-oriented grid are compared (Figure 7.18). As already discussed while exposing the governing equation of the fluid dynamics, pressure and velocity are inherently linked. The pressure fields are very different close to the injector location. The issue is related to the numerical evaluation of the gradients of pressure and velocity in the transport equations. These gradients show different behaviour when they are computed on the different grid arrangements. This is a numerical effect that can be related to mesh quality (non-orthogonality and skewness) or to the gradient scheme adopted. These differences affect the resulting air-fuel mixing, as shown in Figure 7.19.

The non-orthogonality and skewness values obtained in spray-oriented grids adopted for this analysis are very small considering the complex mesh design. They can be further reduced with a more accurate grid design, but they cannot be reduced beyond a certain limit.

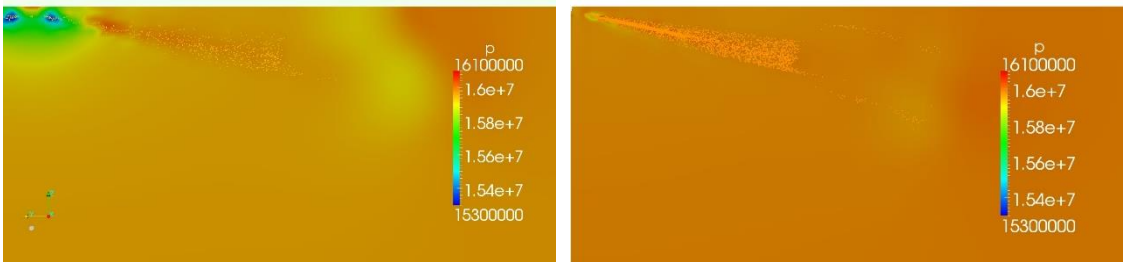


***(a)*** ***(b)***

***Figure 7.18 - Pressure contours for the cartesian grid (a) and the spray-oriented grid (b) obtained at 0.8 ms after SOI. The colour scale is the same in both the images***

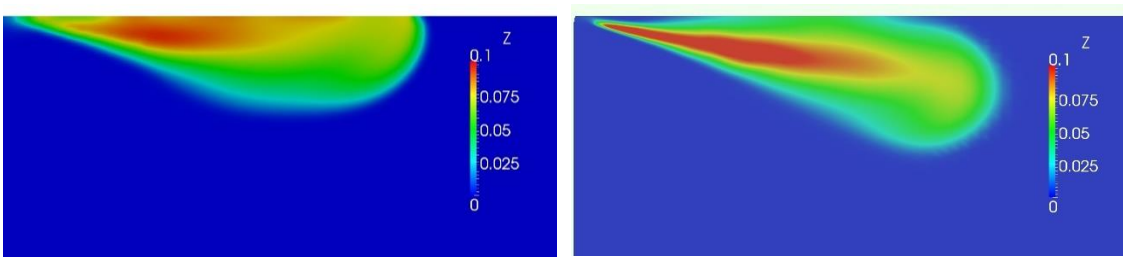


***(a)*** ***(b)***

***Figure 7.19 - Fuel fraction contours for the cartesian grid (a) and the spray-oriented grid (b) obtained at 1.7 ms ASOI***

Syrakos in [30] suggests that the Gauss gradient used in OpenFOAM is inconsistent on unstructured meshes. The use of this gradient scheme results in a zeroth order accuracy (instead of second order as it is reputed) of the finite volume method. The least-squares method is suggested to replace the Gauss gradient. If this is confirmed, important differences in the results can be obtained when the scheme is changed, especially in complex grid.

To conclude, spray-oriented grids present the advantage of a good prediction for liquid velocity and penetration values, but they imply many drawbacks. The grid design results complex and some aspects must be carefully checked to avoid important numerical errors (void fraction and mesh quality). There are many sources of numerical errors that must be controlled in the design phase.

The cartesian grids are very simple to draw. The mesh quality is not a problem and the void fraction results easier to control. The tuning of the parameters allows to compensate the error introduced when the spray does not cross the grid lines perpendicularly. Adopting this kind of mesh, the numerical errors are easier to be managed.

# 8. CONCLUSIONS AND FUTURE WORK

Having presented and analysed the results of many CFD simulations of sprays for IC engine applications, in this chapter the main results will be summarized, considering the initial intent. After that, some guidelines are suggested as starting point for a possible future work.

## 8.1. CONCLUSIONS

### 8.1.1. Sub-Models Effects

The purpose of this thesis was to study the effects of the sub-models and mesh structure on spray simulations for IC engines application. The effects of the sub-models have been evaluated on the spray G configuration suggested by ECN in chapters 5 and 6. The objective was to validate a numerical setup able to describe the spray G configuration comparing the results with experimental data.

Different secondary breakup models have been compared to assess their performances. The results obtained are summarized trying to understand strength and weakness of each model.

TAB and ETAB models provide similar results with a very poor droplet breakup. The simulated spray is composed by large liquid drops (the droplets $SMD$ are strongly overestimated) which hardly evaporate. The penetration values are largely overestimated and the spray morphology is very different from experimental observations. Given these results, TAB and ETAB are not suitable breakup models for sprays simulations.

The Pilch-Erdman breakup model provides good penetration values after a suitable calibration of the constants. It contains only two adjustable parameters, but the most significant effects are shown while changing $B_2$. As its value is deceased, the spray penetration decreases too. The model accounts for the breakup only by reducing the diameter of the parent droplets without creating child drops. This results in a spray morphology where the tips of the spray plumes are composed by large droplets. They hardly evaporate and the penetration values obtained are mainly the consequence of their motion into the inert gas. To summarize, this model is very simple to calibrate and it provides good penetration values, but it not suitable to obtain a complete and detailed characterization of the spray, since the spray morphology that it provides is very different from experimental observations.

Similar conclusions can be drawn for the KHRTPE model. In this case, the model calibration is more complex, since there are more adjustable parameters to consider. Moreover, the penetration values are not so accurate such as the one provided by the Pilch-Erdman model. The morphology shows once again a spray where the plume tips are composed by big droplets, similarly to what is observed for the PE model. Also this model is not suitable to obtain accurate results in spray simulations.

The KHRT model for secondary breakup coupled with the Huh-Gosman model for primary breakup provides the most accurate description of the spray breakup mechanism. The numerical results well predict the experimental data, except for $SMD$ values that are slightly underestimated and liquid velocity values that are overestimated.

The results are proved to be sensitive to the choice of the other sub-models, in particular the turbulence model has a great influence on the simulation. Good predictions of experimental data are obtained when the standard $k$-$\varepsilon$ model with $C_{1\varepsilon}$ = 1.5 is adopted in the numerical setup with KHRT and Huh-Gosman models.

### 8.1.2. Mesh Structure Effects

The effects of the mesh structure on the spray simulations for IC engines application have been investigated using a spray configuration typical of diesel engines. With respect to spray G, this configuration is simpler to describe and the numerical setup adopted is well established.

When a Lagrangian-Eulerian combined approach is adopted, many aspects regarding the grid must be considered to obtain reliable results. In addition to the mesh quality (expressed in terms of non-orthogonality, skewness and aspect ratio), also the presence of the Lagrangian parcels and their interaction with the grid must be accounted when the domain is discretized.

The main mesh structures adopted in IC engines simulation have been compared considering their performances. The results are summarized highlighting strengths and weaknesses.

The adoption of a cartesian mesh (with the grid lines parallel to the axis of the reference system) allows to obtain the highest quality possible in terms of non-orthogonality, skewness and aspect ratio. The main issue highlighted for this grid arrangement is related to the interaction between liquid droplets and mesh elements. In almost all the practical cases, the grid lines do not follow the spray orientation. When this happens, the Lagrangian parcels results to be slowed down more than what happens for a spray-oriented grid. The most important consequences are noticed for penetration values that are underestimated. To overcome this issue, the tuning of model parameters is a solution to adjust the numerical results. In chapter 7, the results show how the penetration values can be adjusted by reducing the area contraction coefficient $C_d$. As side effect, the liquid velocity close to the injection position is strongly overpredicted, with consequences on spray breakup. This implies a further tuning of the parameters present inside all the sub-models adopted for the spray. Moreover, when the grid is not aligned with the spray direction, the liquid velocity close to the tip of the plume is not accurately predicted with possible consequences on the wall impingement.

According to the literature, spray-oriented grids allows to obtain more accurate predictions of the spray characteristics without tuning the model parameters, but, in the practice, they are very complex to design. Many aspects must be considered to avoid numerical errors. The main issue highlighted from the results obtained in chapter 7 is related to the void fraction. When it assumes values close to unity, numerical errors are introduced in the momentum exchange between liquid and vapor phase. The liquid is not slowed down and the surrounding gas suddenly accelerates reaching the same velocity of the liquid drops. This influences the droplet breakup, since it is strongly linked to the

relative velocity among the two phases. High void fraction values are commonly found in spray-oriented grids close to the injection location where the cells are very small. Other issues related to this grid structure are the presence of high aspect-ratio cells (always close to the injector position) and the low quality of the mesh in terms of non-orthogonality and skewness.

Some effects have been observed also comparing the two mesh structures on the spray G configuration where experimental data are available. The most evident effects of the grid dependency of the results are shown when the air entrainment is evaluated through the axial velocity plots as function of time. For cartesian meshes the velocity profile in the spray G configuration are well predicted during the injection process, but, when it finishes, the numerical results do not estimate well the experimental data. Moreover, after the injection process the velocity results provided are very sensitive to the choice of the sub-models adopted, while during injection this is not verified. Spray-oriented grids provide strong underestimations of the gas velocity magnitude in the air entrainment region, with possible consequences on the evaporation. This grid structure provides issues when the pressure and velocity fields are evaluated close to the plume. Possible numerical errors are introduced while the gradients of pressure and velocity are evaluated in the momentum and continuity equations; this is due to poor mesh quality and high void fraction values provided by this grid structure.

Whatever the grid structure adopted is, the results do not converge for successively refined grids. This is a consequence of the Lagrangian-Eulerian coupling; when the grid elements become very small, the void fraction reaches values that can compromise the convergence of the results.

Together with the choice of the sub-models, a correct grid design is the key to obtain reliable results in spray simualtions.

## 8.2. FUTURE WORK

From the numerical perspective it could be interesting to deeply investigate why the spray-oriented grids provide issues in the evaluation of the pressure and velocity gradients. This might permit to obtain useful information to better draw the grid structure.

From the modelling perspective, the development and implementation of new models, such as the KHRTPE, could be a solution to improve the results, since the breakup models adopted in the practice are outdated (the majority of them was developed approximately 30 years ago). This requires also an effort to improve the experimental setup in order to obtain more information about sprays. For example, to better understand the breakup mechanisms, experimental data for both vapor and liquid velocities evaluated in the same location of the spray could be very useful. Moreover, since all the sub-models adopted in the simulation (breakup, turbulence, drag, evaporation) are inherently linked, all of them must be accounted to improve the modelling of the system.

The spray description by Lagrangian-Eulerian approach is proved to be strongly dependent on the grid structure. For this reason, an improvement of the sub-models adopted in the simulation would not be useful if this issue is not overcome. The literature proposes different approaches to reduce the grid-dependency of spray simulations. The so-called ICAS-model (Interactive Cross-sectional Averaged Spray) combined to the Lagrangian-Eulerian approach provides interesting results from this point of view

according to [31]. Another approach proposed to describe sprays is the Eulerian-Eulerian approach; it is more complex, but it provides a lower grid-dependency of the results. It might be useful to investigate them in order to find a better approach to describe the spray.

# Acronyms

| | |
|---|---|
| **IC / ICE** | Internal Combustion / Internal Combustion Engine |
| **GDI** | Gasoline Direct Injection |
| **CFD** | Computational Fluid Dynamics |
| **ECN** | Engine Combustion Network |
| **KHRT** | Kelvin-Helmholtz-Rayleigh-Taylor model |
| **TAB** | Taylor Analogy Breakup model |
| **ETAB** | Enhanced - Taylor Analogy Breakup model |
| **KHRTPE** | Kelvin-Helmholtz-Rayleigh-Taylor-Pilch-Erdman combined model |
| **PE** | Pilch-Erdman model |
| **SMD** | Sauter Mean Diameter |
| **LVF** | Liquid Volume Fraction |
| **SOI / ASOI** | Start of Injection / After Start of Injection |
| **AMR** | Adaptive Local Mesh Refinement |
| **GM** | General Motors |
| **UoM** | University of Melbourne |
| **KAUST** | King Abdullah University of Science and Technology |
| **RANS** | Reynolds Averaged Navier-Stokes Equations |
| **URAN** | Unsteady-RANS |
| **LES** | Large Eddy Simulations |
| **OpenFOAM** | Open Field Operation and Manipulation |
| **LibICE** | Library Internal Combustion Engine |

# Bibliography


[1] Sandia National Laboratories, “Engine Combustion Network,” [Online]. Available: ecn.sandia.gov.

[2] J. Dukowicz, “A Particle-Fluid Numerical Model for Liquid Sprays,” *J Comp Physics,* vol. 35, pp. 229-253, 1980.

[3] T. Lucchini, D. Paredi and J. Lacey, “ECN 6 Proceedings - Evaporative Spray G,” 2018. [Online]. Available: https://ecn.sandia.gov/ecn-workshop/ecn6-workshop.

[4] P. O'Rourke and A. Amsden, “The TAB Method for Numerical Calculations of Sprays Droplet Breakup,” *SAE Paper 872089,* 1987.

[5] F. Tanner, “Liquid Jet Atomization and Droplet Breakup Modeling of Non-Evaporating Diesel Fuel Sprays,” *SAE Papers 970050.*

[6] M. Pilch and C. Erdman, “Use of breakup time data and velocity history data to predict the maximum size of stable fragments for acceleration-induced breakup of a liquid drop,” *Int J Multiphase Flow,* no. 13(6), pp. 741-757, 1987.

[7] S. Hwang, Z. Liu and R. Reitz, “Breakup mechanisms and drag coefficients of high-speed vaporizing liquid drops,” in *Atomization and Sprays, 6(3)*, 1996.

[8] A. Gosman; K.Y. Huh, “A phenomenological model of diesel spray atomization,” *Proceedings of the Int Conf on Multiphase flows,* 1991.

[9] G.Ferrari, Internal Combustion Engines, Esculapio.

[10] Mazda Motor Corporation, [Online]. Available: http://www.mazda.it/mondo-mazda/tecnologia.

[11] Statista, “Worldwide car sales 1990-2019,” [Online]. Available: http://www.statista.com.

[12] International Council on Clean Transportation, in *European Vehicle Market Statistics*, 2018/2019.

[13] C. Osnaghi, Teoria delle Turbomacchine, Bologna: Esculapio, 2006.

[14] W. Malalasekera; H. K. Versteeg, An Introduction to Computational Fluid Dynamics: The Finite Volume Method, Harlow, England: Longman Scientific & Technical, 1995.

[15] F. Bracco, "Modelling of Engines Sprays," *SAE Papers 850394,* 1985.

[16] G. Stiesch, Modeling Engine Spray and Combustion Process, Springer.

[17] G. M. Faeth, L. P. Hsiang and P. K. Wu, "Structure and Breakup Properties of sprays," *Int. J. Multiphase Flow,* vol. 21, pp. 99-127, 1995.

[18] R. Reitz and F. Bracco, "Mechanisms of breakup of round liquid jets," *Encyclopedia of fluid mechanics,* pp. 3:233-249, 1986.

[19] R. Rietz and R. Diwakar, "Structure of high-pressure fuel sprays," *Technical report, SAE Technical Paper,* 1987.

[20] R. D. Reitz, "Modeling atomization process in high-pressure vaporizing sprays," *Atomization and Spray technology,* pp. 3:309-337, 1987.

[21] G. Taylor, "The instabilty of liquid surfaces when accelerated in a direction perpendicular to their planes," in *Proceedings of the Royal Society of London A: Mathematical, Physical and Engineering Sciences*, London , 1950.

[22] "OpenFOAM userguide," OpenFOAM CFD Limited, [Online]. Available: http://www.openfoam.org.

[23] T. Lucchini, G. D'Errico, D. Ettore and G. Ferrari, "Numerical Investigation of Non-Reacting and Reacting Diesel Sprays in Constant-Volume Vessels," *SAE International,* 2009.

[24] "OpenFOAM website," ESI Group , [Online]. Available: http://www.openfoam.com.

[25] "ICE group," [Online]. Available: http://www.engines.polimi.it.

[26] V. Yakhot, S. Orszang, S. Thangam, T. Gatski and C. Speziale, "Development of turbulence models for shear flows by a duoble expansion tecnique," *Physics of Fluids A,* vol. 4, no. 7, pp. 1510-1520.

[27] F. Otto, F. Wirbeleit and J.Willand, "3D-Simualtion innermotorischer Prozesse," *Proc 4th Dresdner Motorenkolloquium,* pp. 279-288, 2001.

[28] A. Lippert, S. Chang, S. Are and D. Schmidt, “Mesh independence and adaptive mesh refinement for advanced engines spray simualtions,” *SAE Technical Paper,* 2005.

[29] J. Abraham, “What is Adequate Resolution in the Numerical Compuations of Transients Jets?,” *SAE Paper 970051,* 1997.

[30] A. Syrakos, S. Varchanis, Y. Dimakopoulos and A. Goulas, “A critical analysis of some popular methods for the discretisation of the gradient operator in finite volume methods,” *Physics of fluids,* 2016.

[31] Y. Wan and N. Peters, “Application of the Cross-Sectional Average Model to Calculations of the dense Spray Region in a Diesel Engine,” *Atomization and Sprays,* vol. 9, no. 2, pp. 111-132, 1999.

[32] G. Z. a. R. J. Z. Scott E. Parrish, “Liquid and Vapor Envelopes of Sprays from a Multi-Hole Fuel Injector Operating under Closely-Spaced Double-Injection Conditions,” *SAE Int. J. Engines 5(2):2012,* doi:10.4271/2012-01-0462.

# List of Figures

# List of Tables